

University of Windsor

## Scholarship at UWindor

---

Electronic Theses and Dissertations

Theses, Dissertations, and Major Papers

---

Winter 2013

### Design and development of a composite automotive anti-roll bar

Michael Doody  
*University of Windsor*

Follow this and additional works at: <https://scholar.uwindsor.ca/etd>

---

#### Recommended Citation

Doody, Michael, "Design and development of a composite automotive anti-roll bar" (2013). *Electronic Theses and Dissertations*. 5040.  
<https://scholar.uwindsor.ca/etd/5040>

This online database contains the full-text of PhD dissertations and Masters' theses of University of Windsor students from 1954 forward. These documents are made available for personal study and research purposes only, in accordance with the Canadian Copyright Act and the Creative Commons license—CC BY-NC-ND (Attribution, Non-Commercial, No Derivative Works). Under this license, works must always be attributed to the copyright holder (original author), cannot be used for any commercial purposes, and may not be altered. Any other use would require the permission of the copyright holder. Students may inquire about withdrawing their dissertation and/or thesis from this database. For additional inquiries, please contact the repository administrator via email ([scholarship@uwindsor.ca](mailto:scholarship@uwindsor.ca)) or by telephone at 519-253-3000ext. 3208.

DESIGN AND DEVELOPMENT OF A COMPOSITE AUTOMOTIVE  
ANTI-ROLL BAR

by  
Michael Doody

A Thesis  
Submitted to the Faculty of Graduate Studies  
through Mechanical Engineering  
in Partial Fulfilment of the Requirements for  
the Degree of Master of Applied Science at the  
University of Windsor

Windsor, Ontario, Canada

©2013 Michael Doody

Design and Development of a Composite Automotive Anti-Roll Bar

by

Michael Doody

APPROVED BY

---

Dr. A. Alpas  
Mechanical, Automotive, & Materials Engineering

---

Dr. W. Altenhof  
Mechanical, Automotive, & Materials Engineering

---

Dr. J. Johrendt, Co-Advisor  
Mechanical, Automotive, & Materials Engineering

---

Dr. B. Minaker, Co-Advisor  
Mechanical, Automotive, & Materials Engineering

October 9, 2013

# Author's Declaration of Originality

I hereby certify that I am the sole author of this thesis and that no part of this thesis has been published or submitted for publication.

I certify that, to the best of my knowledge, my thesis does not infringe upon anyone's copyright nor violate any proprietary rights and that any ideas, techniques, quotations, or any other material from the work of other people included in my thesis, published or otherwise, are fully acknowledged in accordance with the standard referencing practices. Furthermore, to the extent that I have included copyrighted material that surpasses the bounds of fair dealing within the meaning of the Canada Copyright Act, I certify that I have obtained a written permission from the copyright owner(s) to include such material(s) in my thesis and have included copies of such copyright clearances to my appendix.

I declare that this is a true copy of my thesis, including any final revisions, as approved by my thesis committee and the Graduate Studies office, and that this thesis has not been submitted for a higher degree to any other University or Institution.

# Abstract

An analytical elasticity model is developed for laminated cylindrically anisotropic cylinders subjected to extension, bending, pressure, torsion, and transverse shearing. The model predicts the elastic response of thin or thick walled tubes as well as cylinders, and accounts for all elastic coupling present in the aforementioned loading cases. This model is incorporated into analysis software that predicts the linear-elastic response of a composite automotive anti-roll bar. The user may input the bar's two-dimensional geometry, fibre-layup, diameter, and material properties. A filament-wound composite anti-roll bar is designed to act as a lightweight drop-in replacement for the high-performance steel anti-roll bar that is thoroughly benchmarked herein. A mass reduction of 63% is observed when comparing the structural composite bar design to the existing steel bar.

*To my parents,  
for their support of my often exhausting compulsion to know how things work.*

# Acknowledgements

This research has been made possible by the generous financial assistance of the Federal Economic Development Agency of Southern Ontario; for that, I am grateful. Additionally, I would like to thank Andrew Glover, David Glover, and Stephen Ouellette of Thunder Composite Technologies Ltd, for providing me with the opportunity to work closely with them in an industry collaboration on such a promising project.

I would like to thank my supervisors Dr. Bruce Minaker, and Dr. Jennifer Johrendt. The support and guidance they have provided me with has made this experience a positive one. I owe much of my intellectual and professional enrichment to them.

I owe a debt of gratitude to my committee members Dr. Ahmet Alpas, and Dr. William Altenhof.

A special thank you goes out to my colleagues Sean Maloney and Hart Honickman, they have helped me maintain some sanity with my journey through graduate school; I look forward to witnessing their sure success. A special acknowledgement is deserved by Hart, my comrade in anisotropy; the technical advice, friendly guidance, and deeply theoretical conversations he has shared with me have had a marked effect on this work; without him, it would not be what it is.

Finally, I must thank my family and my partner, Sabrina, for their patience and understanding during this endeavour. They have provided me with comfort, solace, and endless love during both challenging and exciting times.

# Contents

<b>Author’s Declaration of Originality</b>	<b>iii</b>
<b>Abstract</b>	<b>iv</b>
<b>Dedication</b>	<b>v</b>
<b>Acknowledgements</b>	<b>vi</b>
<b>List of Tables</b>	<b>x</b>
<b>List of Figures</b>	<b>xi</b>
<b>List of Abbreviations &amp; Definitions</b>	<b>xiii</b>
<b>Notation</b>	<b>xv</b>
<b>1 Introduction</b>	<b>1</b>
1.1 Motivation . . . . .	1
1.2 Research Objectives . . . . .	2
1.3 Thesis Structure . . . . .	2
<b>2 Background Theory</b>	<b>4</b>
2.1 The Automotive Anti-Roll Bar . . . . .	4
2.2 Composites . . . . .	5
2.2.1 Applications . . . . .	5
2.2.2 Fibres . . . . .	6
2.2.3 Polymer Matrices . . . . .	7
2.2.4 Production and Manufacture . . . . .	8
2.2.5 Mechanics of Continuous-Fibre-Reinforced Composites . . . . .	10
2.2.6 Lamination Theory . . . . .	18
2.2.7 Elastic Coupling of Composite Laminates . . . . .	22



---

2.3	Review of Current Literature . . . . .	24
<b>3</b>	<b>Laminated Cylinder Model</b>	<b>27</b>
3.1	Overview . . . . .	27
3.2	Derivation of Stiffness Matrix Terms . . . . .	30
3.2.1	Axial Force . . . . .	30
3.2.2	Moment . . . . .	32
3.2.3	Internal Moment Equilibrium . . . . .	32
3.2.4	Pressure . . . . .	34
3.2.5	Torsion . . . . .	35
3.2.6	Shear . . . . .	36
3.3	Result: Relationship Between Loading and Elastic Response . . . . .	38
3.4	Discussion . . . . .	40
3.4.1	Bending . . . . .	40
3.4.2	Transverse Strain Gradients . . . . .	40
3.4.3	Pressure . . . . .	40
3.4.4	Transverse Shear . . . . .	41
3.4.5	Additional Stress and Strain Distribution Considerations . . . . .	43
3.4.6	Through-Thickness Normal Stress . . . . .	44
<b>4</b>	<b>Validation of The Elasticity Model</b>	<b>45</b>
4.1	Finite Element Analysis . . . . .	45
4.1.1	Elastic Response to Torsion of a Thin-Walled Tube . . . . .	45
4.1.2	The Effect of Tube Wall-Thickness on Axial Response & Coupling . . . . .	47
4.1.3	Final Remarks . . . . .	50
4.2	Experimental Program . . . . .	50
4.2.1	Specimens . . . . .	50
4.2.2	Apparatus . . . . .	51
4.2.3	Three-Point-Bending Tests . . . . .	56
4.2.4	Torsion Tests . . . . .	58
4.2.5	Discussion . . . . .	60
<b>5</b>	<b>Anti-Roll Bar Analysis &amp; Design</b>	<b>63</b>
5.1	Benchmarking of the Steel Anti-Roll Bar . . . . .	64
5.1.1	Classical Analytical Methods . . . . .	64
5.1.2	Finite Element Analysis . . . . .	65
5.1.3	Experimental Testing . . . . .	69

---

5.2 Composite Anti-Roll Bar . . . . .	71
5.2.1 Analysis Software . . . . .	71
5.2.2 Design . . . . .	74
5.2.3 Discussion and Recommendations . . . . .	76
<b>6 Conclusions &amp; Recommendations</b>	<b>78</b>
6.1 Summary . . . . .	78
6.2 Conclusions . . . . .	79
6.3 Recommendations for Future Work . . . . .	79
6.4 Contributions . . . . .	81
<b>References</b>	<b>82</b>
<b>A Specimen Measurements</b>	<b>85</b>
<b>B Laminated Cylinder Model Input</b>	<b>87</b>
<b>C Laminated Cylinder Model Code</b>	<b>89</b>
<b>D Composite Anti-Roll Bar Analysis Code</b>	<b>94</b>
<b>Vita Auctoris</b>	<b>103</b>

# List of Tables

2.1	Fibre-direction strain under various loading directions . . . . .	15
2.2	Elastic coupling in various classes of laminate architecture . . . . .	24
4.1	In-plane properties of unidirectional carbon-fibre/epoxy laminate used in FE studies . . .	46
4.2	Mesh sensitivity study of torsionally loaded FE model . . . . .	47
4.3	Axially loaded model results: axial force response $dl$ & associated extensional-torsional coupling $\phi$ for a number of tubes with varying wall-thickness . . . . .	49
4.4	Cylindrical FRP test specimen dimensions . . . . .	51
4.5	Three point flexure test: experimental results and laminated cylinder model predictions for each specimen . . . . .	58
4.6	Torsion test: experimental results and laminated cylinder model predictions . . . . .	60
4.7	Sensitivity of the model's elastic response prediction to input variables and properties . . .	62
5.1	Stiffness contributions in steel anti-roll bar . . . . .	65
5.2	Steel ARB finite element mesh-sensitivity study data . . . . .	68
5.3	Steel ARB test (polymer bushings) . . . . .	71
5.4	Steel ARB test (steel bushings) . . . . .	71
5.5	In-plane properties of carbon and E-glass unidirectional laminates . . . . .	74
A.1	Sample 1A measurements . . . . .	85
A.2	Sample 1B measurements . . . . .	85
A.3	Sample 1C measurements . . . . .	86
A.4	Sample 2A measurements . . . . .	86
A.5	Sample 2B measurements . . . . .	86
A.6	Sample 2C measurements . . . . .	86
B.1	Material properties of E-glass fibres and epoxy matrix used in test specimens . . . . .	87
B.2	Specimen fibre volume fraction calculation . . . . .	88
B.3	Local elastic properties of individual laminae in test specimens . . . . .	88

# List of Figures

2.1	Effect of an anti-roll bar vehicle body roll . . . . .	4
2.2	Anti-Roll bar as seen in a vehicle . . . . .	5
2.3	Notation and dimensions for the discussed laminate . . . . .	19
2.4	Moments and forces on an element in lamination theory . . . . .	21
2.5	Undeformed and deformed shape of a unidirectional lamina with off-axis loading . . . . .	23
3.1	Local and global coordinate systems for a layered FRP tube in arbitrary state of deformation	28
3.2	Depiction of area used in axial, moment, torsion, and shear calculations . . . . .	31
3.3	Depiction of area used to equilibrate internal moments . . . . .	33
3.4	Depiction of area used in internal pressure calculations . . . . .	35
3.5	Distribution of shear stress in circular cross-sections with response to transverse shear loading (of an isotropic material) . . . . .	42
4.1	FE torsion model: constraints and loading (0.5 mm mesh shown) . . . . .	46
4.2	FE axial loading model: constraints and loading . . . . .	48
4.3	Percent difference in predictions of FE and laminated cylinder model on axial response and axial-torsional coupling . . . . .	49
4.4	MTS <sup>®</sup> Model 642.25 Bend Fixture . . . . .	52
4.5	Torsion Testing Machine . . . . .	53
4.6	Primary-function components of torsion testing machine . . . . .	55
4.7	Experimental setup: three point flexure test (sample 1C) . . . . .	57
4.8	Experimental setup: torsion test (live-end with specimen 2A mounted) . . . . .	59
4.9	Experimental setup: torsion test (dead-end with specimen 2A mounted) . . . . .	59
5.1	Geometry of existing steel anti-roll bar . . . . .	63
5.2	Simplified anti-roll bar geometry: plan view . . . . .	64
5.3	Solid element mesh (2.5 mm nominal element length) . . . . .	66
5.4	Wireframe model showing constraints and applied loading . . . . .	67

---

5.5	Coarsest and finest mesh used in steel ARB convergence study . . . . .	68
5.6	Steel ARB finite element solution convergence: linear spring-rate vs. element size . . . . .	69
5.7	Physical testing setup: fixed end with polymer bushing . . . . .	70
5.8	Physical testing setup: actuated end with steel bushing . . . . .	70
5.9	Line geometry input to CARBA software (congruent with classical analysis) . . . . .	72
5.10	Vertical displacement profile output from CARBA software for the steel bar . . . . .	73
5.11	Desired line geometry of composite ARB . . . . .	74
5.12	Linear anti-roll bar stiffness vs. fibre angle for composite bars . . . . .	75
5.13	Vertical displacement profile output from CARBA software for the composite bar . . . . .	75

# List of Abbreviations & Definitions

All abbreviations used in this work are described in this section; some esoteric terms used here are also defined for convenience.

## Abbreviations

Abbreviation	Meaning
ASTM	American Society for Testing and Materials
ARB	Anti-Roll Bar
CHEXA	An Eight Noded Hexahedral Brick Element
CPU	Central Processing Unit
CLPT	Classical Laminated Plate Theory
CARBA	Composite Anti-Roll Bar Analysis
CQUAD4	A First Order Four Noded Shell Element
FRP	Fibre-Reinforced Polymer
FE	Finite Element
MATLAB <sup>®</sup>	Matrix Laboratory
PC	Personal Computer
RTM	Resin Transfer Moulding
RBE2	Rigid Body Element (interpolation type)
RBE3	Rigid Body Element (true rigid type)
SMC	Sheet Moulding Compound
SPC	Single Point Constraint

## Definitions

---

<b>Term</b>	<b>Definition</b>
Anisotropic	Having elastic properties that depend on direction or orientation, and being fully described by 21 elastic constants
Axial-symmetrical loading	A loading that tends to induce strains that are symmetrical about an axis, e.g., torsion, axial tension/compression, and uniform pressure loading
Cylindrically anisotropic	A material is cylindrically anisotropic when its elastic properties are constant within a cylindrical coordinate system
Isotropic	Having elastic properties independent of direction or orientation, and being fully described by two elastic constants
Orthotropic	Having three orthogonal planes of material symmetry, within which elastic properties are independent of direction, and being fully described by nine elastic constants
Transversely isotropic	Having elastic properties that are constant within a plane, but different along the direction normal to this plane: a special case of orthotropy requiring only five elastic constants to be fully described

---

# Notation

Mathematical notation throughout this work is listed below, separated by the chapter in which it first appears.

## Background Theory

Label	Description
$A$	Extensional stiffness matrix
$A_{mn}$	The $n^{th}$ entry in the $m^{th}$ row of the $A$ matrix
$B$	Coupling stiffness matrix
$B_{mn}$	The $n^{th}$ entry in the $m^{th}$ row of the $B$ matrix
$C$	Laminate stiffness matrix
$D$	Bending stiffness matrix
$D_{mn}$	The $n^{th}$ entry in the $m^{th}$ row of the $D$ matrix
$E_{11}$	Effective elastic modulus in the fibre-direction
$E_{22}$	Effective elastic modulus in the transverse 2-direction
$E_{33}$	Effective elastic modulus in the transverse 3-direction
$E_f$	Longitudinal elastic modulus of fibre
$E_m$	Elastic modulus of matrix
$G_{12}$	In-plane shear modulus
$G_{13}$	Out-of-plane fibre-direction shear modulus
$G_{23}$	Out-of-plane transverse shear modulus
$h_x$	Elevation $h$ to the outer edge of lamina $x$
$k$	Designated layer number
$M_{xx}$ , and $M_{yy}$	Bending moment per unit width of laminate in the $x$ - $z$ and $y$ - $z$ planes, respectively
$M_{xy}$	Twisting moment per unit width of laminate
$N$	Total number of Laminae within the laminate



$N_{xx}$ , and $N_{yy}$	Normal force per unit width of laminate in the $x$ and $y$ direction, respectively
$N_{xy}$	In plane $x$ - $y$ shear force, per unit width of laminate
$\mathbf{Q}$	The orthotropic lamina stiffness matrix
$\bar{\mathbf{Q}}$	The transformed lamina stiffness matrix
$\bar{Q}_{11}$	The first term of the first row of the transformed lamina stiffness matrix
$Q_{11}$	The first entry in the first row of the $\mathbf{Q}$ matrix
$\bar{Q}_{xy}$	The $y^{th}$ entry in the $x^{th}$ row of the transformed lamina stiffness matrix
$Q_{xy}$	The $y^{th}$ entry in the $x^{th}$ row of the $\mathbf{Q}$ matrix
$\mathbf{S}$	Laminate compliance matrix
$\mathbf{S}_{3D}$	Three-dimensional compliance matrix for an orthotropic lamina
$T_g$	Glass transition temperature
$u$ , $v$ , and $w$	Displacement in the $x$ , $y$ , and $z$ directions, respectively
$V_f$	Ratio of fibre to matrix volume (fibre-volume fraction)
$z_k$	The distance between the mid-plane of lamina $k$ and the mid-plane of the laminate, referred to as lamina elevation
$\epsilon_1$	Strain in the fibre direction
$\epsilon_2$	Strain in the transverse 2-direction
$\epsilon_3$	Strain in the transverse 3-direction
$\epsilon_{xx_k}$ , and $\epsilon_{yy_k}$	Normal strain in the $x$ and $y$ directions, respectively, within lamina $k$
$\epsilon_{xx}^0$ , and $\epsilon_{yy}^0$	Mid-plane normal strain in the $x$ and $y$ directions, respectively, of the laminate
$\gamma_{12}$	Shear strain in the 1-2 plane
$\gamma_{23}$	Shear strain in the 2-3 plane
$\gamma_{31}$	Shear strain in the 3-1 plane
$\gamma_{xy_k}$	In-plane $x$ - $y$ shear strain (engineering strain) within lamina $k$
$\gamma_{xy}^0$	Mid-plane in-plane $x$ - $y$ shear strain (engineering strain) in the laminate
$\kappa_{xx}$ , and $\kappa_{yy}$	Bending curvature of the laminate in the $x$ - $z$ and $y$ - $z$ planes, respectively
$\kappa_{xy}$	Twisting curvature of the laminate
$\nu_{12}$	Poissons ratio in the 2-direction due to 1-direction loading (major Poisson's ratio)

$\nu_{13}$	Poissons ratio in the 3-direction due to 1-direction loading
$\nu_{21}$	Poissons ratio in the 1-direction due to 2-direction loading (minor Poisson's ratio)
$\nu_{23}$	Poissons ratio in the 3-direction due to 2-direction loading
$\nu_{31}$	Poissons ratio in the 1-direction due to 3-direction loading
$\nu_{32}$	Poissons ratio in the 2-direction due to 3-direction loading
$\nu_f$	Poisson's ratio of fibre
$\nu_m$	Poisson's ratio of matrix
$\sigma_1$	Normal stress in the fibre direction
$\sigma_2$	Normal stress in the transverse 2-direction
$\sigma_3$	Normal stress in the transverse 3-direction
$\tau_{12}$	Shear stress in the 1-2 plane
$\tau_{23}$	Shear stress in the 2-3 plane
$\tau_{31}$	Shear stress in the 3-1 plane
$\theta$	The angle of fibres within a lamina, relative to the $x$ axis of the $x$ - $y$ - $z$ coordinate system

---

## Laminated Cylinder Model

Label	Description
$a$ , and $b$	Distance from the tube's center to the outer and inner edges, respectively, of a lamina
$dF_{jj_n}$	Normal force in the $jj$ direction acting on an infinitesimal element in lamina $n$
$F_{xx}$	Applied axial force
$G_{ik}$	Shear modulus in the $i$ - $k$ direction
$M_{int_x}$	total internal moment about the $x$ axis
$\mathbf{M}$	Laminated cylinder model stiffness matrix
$M_y$ , and $M_z$	Applied bending moment about the $y$ and $z$ axes, respectively
$P$	Internal Pressure
$r_i$	Inner radius of the tube
$r_n$	Mid-lamina radius of lamina $n$
$T$	Torque applied axially to the tube
$t_n$	Thickness of lamina $n$

$V_{ij}$ , and $V_{ik}$	Shear loading in the $i$ - $j$ and $i$ - $k$ planes, respectively
$V_{xy}$ , and $V_{xz}$	Applied global shear loading in the $x$ - $y$ and $x$ - $z$ planes, respectively
$\epsilon_{ii}$	Strain in the axial ( $ii$ ) direction
$\epsilon_{jj}$	Strain in the tangential ( $jj$ ) direction
$\epsilon_D$	Uniform diametric expansion strain
$\gamma_{ij\text{shear}}$	Shear strain in the $i$ - $j$ plane caused by transverse shear
$\gamma_{ij}$	Shear strain in the $i$ - $j$ plane
$\gamma_{\text{transverse}}$	Transverse in-plane shear strain that results from an axial load
$\gamma_{xy}$ , and $\gamma_{xz}$	Global transverse shear deformation in the $x$ - $y$ and $x$ - $z$ planes, respectively
$\kappa_y$ , and $\kappa_z$	Angle of curvature about the $y$ and $z$ axes, respectively
$\phi$	Angle of twist
$\psi$	Variable defined for convenience
$\sigma_{ii}$	Normal stress in the axial ( $ii$ ) direction
$\sigma_{jj}$	Normal stress in the tangential ( $jj$ ) direction
$\tau_{ij}$ , and $\tau_{ik}$	Shear stress in the $i$ - $j$ and $i$ - $k$ planes, respectively
$\theta$	Angle between $y$ axis and point or plane of interest

---

## Validation

Label	Description
$EI$	Bending stiffness
$J_{\text{classical}}$	Polar moment of inertia, calculated in the classical and exact manner
$J_{\text{shell}}$	Polar moment of inertia, calculated as modelled with FE shell elements
$JG$	Torsional Rigidity
$L$	Span length
$P$	Applied load
$T$	Applied torsion
$x$	Deflection

---

# Chapter 1

## Introduction

The introduction consists of three sections; the first section discusses the motivation behind the research presented herein. The second section outlines three major research objectives, and the third section provides the reader with an overview of the thesis structure.

### 1.1 Motivation

The automotive industry is increasingly being pushed by government fuel economy and emissions mandates to make cars more efficient, lighter, and 'greener'. This movement has facilitated development of an impressive suite of technology ranging from highly efficient small-displacement forced-induction internal combustion engines, to hybrid or purely electric powertrains among other technologies. While these technologies and many others are helping automotive manufacturers lower emissions and approach mileage targets, they will not suffice without supplement; substantial vehicle lightweighting is necessary. Generally, this means that traditional material choices are reconsidered. To this end, the use of aluminium alloys, high strength steel alloys, and fibre reinforced polymers (FRPs) is gaining popularity.

Fibre reinforced composite parts are used extensively in the aerospace and motorsports industries for structural applications. The automotive industry, however, has not yet seen the same level of composite material integration into structural elements of high-production-volume vehicles. The author believes this is a function of primarily two factors: a lack of low-cost high-volume manufacturability, and a lack of understanding of the behaviour of the composite materials themselves. The work presented herein has been motivated by an industry collaboration that aims to make improvements to both of the aforementioned factors, with research focused on the latter.

A proprietary manufacturing methodology for filament-wound FRP structures that allows varying fibre-angle and cross-section throughout the length of a member has been developed. The conventional design approach of finite element modelling does not lend itself well to optimization schemes for a

structure of this type. This point, compounded by a deficit in literature of a comprehensive analytical elasticity model for thick-walled composite tubes and beams of circular cross-section, demonstrates the need for research.

## 1.2 Research Objectives

The first objective of the research is development an analytical elasticity model for axially symmetric, cylindrically anisotropic tubes and rods subjected to extension, bending, pressure, torsion, and transverse shearing. The model captures all of the elastic coupling phenomena present in the loading of a helically wound continuous-fibre composite laminated cylinder.

The second objective is validation of the derived elasticity model. Computational validation was carried out using commercial finite element software; in addition, a limited amount of physical testing was performed to serve as experimental validation of predicted torsional stiffness and bending compliance.

The third objective is development of a structural design for a filament-wound composite automotive anti-roll bar that will act as a lightweight replacement to an existing steel bar. Care will be given to ensure that the design is both cost effective, and lightweight. The model established in the first objective will be used in a computer design package to tailor the elastic response of the composite anti-roll bar. The desired response is a function of parameters determined through analytical and physical benchmarking of the existing steel bar.

## 1.3 Thesis Structure

The author has made an effort to present the material of this thesis in an order that is both logical and conducive to a firm understanding of the work documented herein. The first chapter provides the reader with some insight into what motivated this research, as well as a clear outline of the research objectives.

The second chapter will serve to introduce the novice reader to the background theory that is necessary to understand the material presented in the chapters that follow; for the reader who is versed in this area of science, it may serve as a reference. An introduction is provided on the automotive anti-roll bar, followed by a definition of composite materials, with a focus on fibre-reinforced polymers. Common applications and manufacturing methods of composites are discussed before outlining the theory associated with their analysis and design. Finally, a review of current and relevant literature is presented.

The third chapter addresses the first research objective, presenting a novel elasticity model for cylindrically anisotropic laminated cylinders and tubes, and outlining the model's derivation. A thorough discussion is given with regard to the assumptions, limitations, and implications of the model.

The fourth chapter details the computational and experimental model validation that was performed. The physical test specimens, apparatus, experimental tests, and results are discussed in detail.

The fifth chapter describes the benchmarking of the steel anti-roll bar, and presents the procedure adopted in utilizing the developed model for design of a composite anti-roll bar, as well as the design that resulted.

Conclusions are drawn and provided in the sixth chapter.

## Chapter 2

# Background Theory

This chapter provides an introduction to the automotive anti-roll bar, followed by some background theory necessary for a solid understanding of fire-reinforced composite materials and their design. Lastly, a review is provided of current literature relevant to the work presented herein.

### 2.1 The Automotive Anti-Roll Bar

An anti-roll bar (ARB), known also as a sway bar, is an automotive suspension component that elastically couples the suspension on one side of a vehicle to the adjacent side. If the suspension on one side of the vehicle is compressed, a reactive force will be generated by the ARB tending to compress the suspension on the adjacent side of the vehicle. This coupling serves to reduce the amount of ‘body roll’ a vehicle will experience during cornering (see Figure 2.1). Body roll is defined as the angle through which the vehicle’s body rotates about its longitudinal axis; this motion is not only uncomfortable for passengers, but detrimental to vehicle traction and handling due to the non-linear response of pneumatic automotive tires.

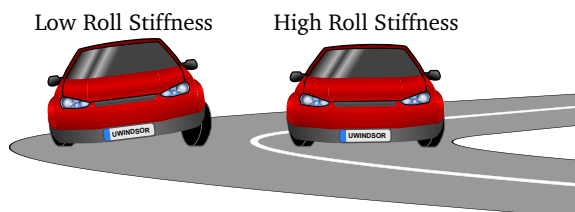


**Figure 2.1:** Effect of an anti-roll bar vehicle body roll

The most conventional style of ARB is a long C-shaped spring-steel member of circular and constant cross section; this style is shown in Figure 2.2. The bar is affixed to the frame of the vehicle with rubber

bushings allowing rotation of the bar while constraining translation. The ends of the bar are pinned to the moving suspension components on each side of the vehicle by 'end links': short links with a spherical joint at each end. If the vehicle's left and right wheels move upward in unison, as would be the case when driving over a speed bump (perpendicularly), both ends of the bar move together causing only rotation within the rubber bushings. However, if one wheel moves independently, the mid-span of the bar is put into a state of torsional deflection as the cantilevered anti-roll bar ends move relative to each other. Therefore, the stiffness of the anti-roll bar (measured in a manner consistent with the deformation observed) directly dictates the degree of coupling between the left and right side vehicle suspension.

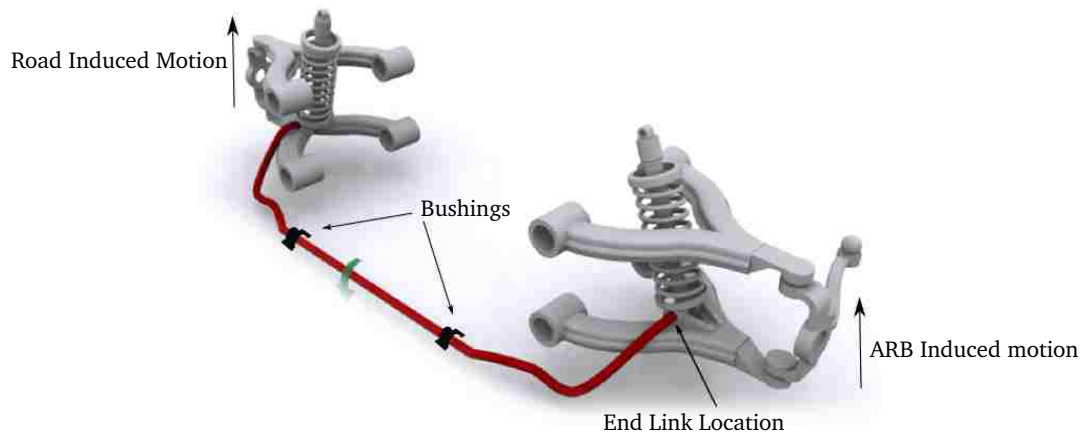


**Figure 2.2:** Anti-Roll bar as seen in a vehicle (reproduced and adapted from [www.carbibles.com](http://www.carbibles.com))

A large amount of research and effort [1][2][3] has been aimed at studying the effects of vehicle roll stiffness as well as the effect ARBs have on vehicle dynamics. Numerous designs including active electronically-controlled ARBs are in existence, but not discussed here. The purpose of this section is to provide a novice reader with a rudimentary understanding of ARB basics; this understanding will be necessary to comprehend the implications of an anti-roll bar's structural and elastic behaviour.

## 2.2 Composites

### 2.2.1 Applications

Fibre reinforced composites have found their way into numerous industries; the number of applications seems limitless and is continually growing. Some significant applications are listed in the following discussion, but by no means is this an exhaustive list.

The aircraft and military industries seem to be at the forefront of FRP development, likely due to their inherent need for lightweight structural materials, as well as the considerable funding and resources



typically available to them. Boron fibre-epoxy composite stabilizer skins were introduced to production F-14 fighter aircraft in the late 1960s, and the use of FRPs in aerospace has only increased; today there are many aircraft having airframes composed mostly of FRP. Many modern helicopters exploit the advantages of FRP rotor blades, allowing reduced weight, greater fatigue and corrosion resistance, and less vibration sensitive designs. The fibre angle can even be altered along the length of the rotor to tune the vibration characteristics of the rotor blade reducing the effect of resonance frequencies.

The automotive industry has been slower to adopt heavy use of FRP components and structure to a production environment, likely because of the cost and production time associated with most manufacturing methods. Lower production, higher budget products in the automotive industry make extensive use of composites; Formula 1 racecars are made primarily of carbon FRPs. A process that will be described later in the text uses sheet moulding compound (SMC) to allow fast and cheap production of hoods, deck lids, doors, and various other automotive panels. Sheet moulding compound panels are typically composed of chopped strand glass-fiber and polyester resin. General Motors began using filament wound, compression moulded composite leaf springs for the Corvette in 1981, providing an 80% weight savings [4]. More recently the Corvette has adopted front and rear composite leaf springs mounted in a manner conducive to an anti-roll effect. Carbon FRP driveshafts have been implemented and proven in both racing and heavy industrial applications; the increased damping and decreased mass allow for use of a longer unsupported drive shaft without the severe resonance encountered in metallic driveshafts.

Other industries include sporting goods (golf clubs, bicycles, skis, etc), marine (boat hulls, masts, etc), and even civil engineering (glass and carbon fibre have been used to reinforce concrete and eliminate corrosion based degradation).

### 2.2.2 Fibres

The fibre component of a fibre-reinforced composite has a much larger effect on strength and stiffness than the matrix. There is more than one reason for this: generally the fibre volume fraction (discussed in detail in Section 2.2.5) is larger than 50% – meaning the composite contains more fibre than matrix; also, more importantly, the tensile strength and modulus of the fibre is generally much higher than that of the matrix. With fibre properties being so dominant, much effort goes into the characterization of different types of fibres. Important properties are tensile and compressive modulus and strength, density, fatigue behaviour, cost of manufacture, and electrical and thermal properties. Fibres are typically arranged into either a cloth with one or more fibre directions, strands (a unidirectional yarn of fibres), or rovings (a continuous bundle of strands). Fibres may be totally raw, or coated in a sizing that promotes matrix adhesion or reduces fibre-fibre friction in rovings. Also available are pre-impregnated or ‘prepreg’ forms of fibres: uncured resin is infused into the roving, strand, or cloth at a specific ratio. The prepreg material is typically stored in a refrigerated environment to prevent any premature or undesired curing. Attributes of the more popular fibres are discussed in the descriptions that follow.

### **Glass Fibres**

Glass fibres remain the most popular fibre for FRPs. This is likely a result of low-cost manufacturability, and moderate strength-to-weight ratio. Glass fibres are highly resistant to chemicals, provide very good insulating properties, and have high tensile strength. Disadvantages include high density, low modulus, and brittle behavior. Two main types of glass are available: E-glass (electrical grade) and S-glass (structural grade). S-glass provides higher tensile strength at a cost premium. Diameters of glass fibres typically range from 8–14 microns [5].

### **Carbon Fibres**

Carbon fibres can offer significant performance advantages over glass: high stiffness-to-weight ratio, low density, and high strength-to-weight ratio at an intermediate cost. The properties of carbon fibres can vary drastically depending on the method of manufacture, allowing the engineer to make a decision based on whether strength or stiffness is of more importance – generally there is a trade off. The tensile modulus of carbon fibres has been reported [6] to range from 207 GPa to 1035 GPa. Tensile strength ranges from 1.9 GPa to as high as 6.9 GPa in recent developments with diameter ranging from 6–8 microns [5]. Aside from the qualities listed, carbon fibres boast a very low coefficient of thermal expansion, a high thermal conductivity, and good fatigue strength characteristics. Disadvantages can include high electrical conductivity, low strain-to-failure, and poor impact resistance.

### **Aramid Fibres**

Known also under the trade name Kevlar 49, aramid fibres exhibit a remarkably low density and high strength-to-weight ratio, and very good impact resistance (even failing in a ductile manner). Aramid fibres show moderate chemical resistivity, and great resistance to high temperatures and combustion. Their tensile strength is approximately 3.6 GPa, tensile modulus: 130 GPa, and fibre diameters are on the order of 12 microns. Disadvantages of aramid fibres include poor compressive strength and difficulty in cutting.

### **Other Less Frequently Used Fibres**

Extended chain polyethylene fibres (known also by their trade name Spectra or Dyneema) have an extremely high strength to weight ratio, good abrasion resistance, but poor matrix adhesion and undesirable properties of creep.

## **2.2.3 Polymer Matrices**

While it has been stated that the properties of the fibre are dominant, the matrix of a fibre-reinforced composite plays a significant role in the overall performance of the material. The presence of a matrix

facilitates fibre-to-fibre stress transfer as well as fibre stability and resistance to buckling under compressive load. Inter-laminar shear strength and elastic shear modulus are governed largely by matrix choice and matrix-fibre adhesion. The toughness or resistance to brittle fracture of a composite can be influenced heavily by matrix properties. The matrix also provides the fibres with abrasion resistance, and isolation from potentially harmful moisture and chemicals.

There are two major categories of polymer matrices: thermosets, and thermoplastics. Thermoset polymers include epoxies, polyesters, vinyl esters, phenolics, polyimides and cyanate esters. Thermoplastic polymers include nylons, polycarbonates, polyethylene terephthalate, and many others.

Thermoset polymers typically begin production as a two part system of low viscosity liquids that are mixed together, allowing a curing reaction to take place. Once cured, the long chain-like molecules form cross-links that strengthen and stiffen the material, but also prevent the reforming that is possible with thermoplastics. Generally, thermosets provide superior resistance to creep and stress relaxation when compared to thermoplastics. There are disadvantages to thermoset polymers: low strain to failure, extended curing or polymerization times, and limited pot life – the length of time a mixed liquid batch of thermoset ingredients can be left at room temperature.

Thermoplastic polymers do not require a chemical curing process to form molecular cross-links and assume a stable solid shape. Because thermoplastics are not cross-linked, they may be heated or melted and formed into a desired shape repeatedly. While thermoplastics do not offer good creep and stress relaxation characteristics, they do exhibit larger values of strain-to-failure and better resistance to crack propagation.

Both thermosets and thermoplastics exhibit a significant behaviour shift at a certain elevated temperature known as the glass transition temperature  $T_g$ . The stiffness of the polymer is significantly reduced at, and even leading up to  $T_g$ , limiting the temperature range within which a particular matrix is useful.

Non-polymer matrices such as metal and ceramic do exist and have been proven as a very useful technology, but the scope of this document will be limited to polymers – or rather, fibre-reinforced polymers (FRPs).

#### 2.2.4 Production and Manufacture

The direction of fibres in an FRP component has a profound effect on its performance; because of this, an understanding of the manufacturing process is important to the analysis of an FRP structure. Certain manufacturing processes lend themselves well to particular shapes, or to high production-rates and low manual labour requirements. The automotive industry is largely responsible for the recent advancements in low-labour high production rate manufacturing processes.

### **Sheet Moulding Compound**

Sheet moulding compound (SMC) refers to both a material and the manufacturing process used to make it. The process involves fibres (typically glass) being strewn atop a sheet of un-cured polyester resin; once the chopped rovings are settled, another resin sheet is laid on top. The resin-fibre-resin stackup is then sandwiched between two layers of thin sheeting known as carrier film. These layers of film are later removed when the sheet is placed into a heated compression mould to be shaped and cured. The process lends itself very well to a mass production environment, which is likely why it has such popularity in the automotive industry for the manufacture of hoods, deck lids, door panels, and other suitable parts.

### **Filament Winding**

Another manufacturing method that can be highly automated is filament winding: a process in which continuous rovings or strands are wound around a mandrel that is later removed. A typical setup has the mandrel rotating while a fibre is laid down at some angle by a carrier moving laterally to the longitudinal axis of the part. The rovings may be wetted out prior to winding, or alternatively, prepreg rovings can be used to eliminate the sometimes messy procedure of wet layup. Examples of parts typically produced using filament winding are automotive drive shafts, large storage tanks, pipelines, and helicopter rotor blades. Numerous variations of the filament winding process have been established to meet needs specific to certain applications; no attempt has been made here to detail each of them.

### **Tube Rolling**

Tube rolling is another process that can produce hollow and axisymmetric<sup>1</sup> tubes. Lengths of tape (usually prepreg) are wrapped onto a mandrel by a specialized set of rollers. Once the fibre layup is complete, the mandrel and uncured material may be placed in a split mould for cure, or encased in a heat shrink wrap and placed in an air-circulating oven. Tube rolling offers higher production rates than filament winding, but does not offer the same flexibility in fibre angle.

### **Pultrusion**

Pultrusion is a continuous process in which unidirectional fibres and possibly woven cloth are pulled through a heated die, emerging cured in the desired cross sectional shape and cut into lengths. Fibres pass through a wet-out bath before being arranged into the mould by a preform. Often, woven cloth is added to the outside of pultruded members such that the outermost layer of fibres is oriented at an angle to add transverse strength. Additionally, the woven cloth protects the load bearing unidirectional core from abrasion – both in the mould and in the member's end use. Much like filament winding, variations

---

<sup>1</sup>When tube rolling is performed on tapered mandrels, the result is not always a perfectly axisymmetric fibre layup.

on the process are plentiful; a noteworthy example is pull-winding, where fibres are wound or even braided around a core as they are pulled through a die.

### **Resin Transfer Moulding**

The resin transfer moulding or RTM process involves dry layers of continuous strand mat, chopped strand mat, or woven cloth set into a two part mould containing channels through which resin may be injected (at pressures reaching 690 KPa [6]). Precautions are taken such that the air, which the resin is displacing, has an escape path and does not become entrapped as a void.

### **Prepreg Layup & Vacuum Bagging**

Prepreg layup is a labour-intensive and low production rate manufacturing process most used in motor-sports, military, and aerospace industries. Sheets of woven cloth or unidirectional ply are removed from their refrigerated storage and cut by hand or with automated cutting machinery using a laser, water jet, or an ultrasonic cutter. The plies are warmed slightly to increase pliability and tackiness and then stacked in a mould by hand, or by an automated machine. Once the desired layup is fitted into the mould, a series of bleeder, breather, and barrier materials are laid atop, before the vacuum bag is sealed around the part and mould. After vacuum is applied to a valve on the vacuum bag, removing most of the air, the whole assemblage is placed in an autoclave, where it can be subjected to a prescribed temperature-pressure schedule. Part quality and performance is remarkable in this process, justifying its use if cost and production rate are of secondary concern.

## **2.2.5 Mechanics of Continuous-Fibre-Reinforced Composites**

The primary factor distinguishing the analysis of conventional engineering materials like steel or aluminium from that of composite materials is a directionality of material properties. Steel and aluminium can typically be treated as isotropic<sup>1</sup> (having material properties equal in all directions), while continuous-fibre-reinforced composites exhibit large variations in strength, moduli, Poisson's ratio, and thermal expansion coefficients depending on the angle at which they are measured. In general a material of this type is known to be anisotropic; when the material can be shown to have certain symmetries it is orthotropic. An orthotropic material has principal axes along which tensile or compressive loading produces no resulting shear stress. Similarly, shear loading in the plane of symmetry induces no normal stress.

In the case of continuous-fibre-reinforced composites, an orthotropic material model is assumed. The properties of the fibre and the matrix are used to give a "smeared" set of net material properties which

---

<sup>1</sup>Most steel and aluminium alloys do exhibit a directionality of material properties; however, this phenomenon does not become pronounced until dealing with the plastic deformation of materials processed in complex manners (multi-stage rolling and stretching).[7]

are treated as homogeneous throughout that particular orientation of material.

Before delving fully into macro-mechanics level stress-strain relations, it is necessary to examine the microstructure of continuous-fibre-reinforced materials – moreover, the interaction between the fibres and the matrix. While the apparent purpose of studying micro-mechanics is to develop material properties that are usable in macro-mechanics, the reality is not generally a reliable correlation. In cases where appropriate test material can be obtained, the majority of reliance will be placed on the results of physical testing. Micro-mechanics theories prove more useful in providing insight towards failure modes and allowing the inference (from physical test data) of material properties within a range of volume fraction [5]. The sections that follow will outline current theory and methodology relating to micro-mechanics, and to macro-mechanics.

### Micro-Mechanics: Fibre-Matrix Interaction

There are three constants required to describe the linear-elastic response of an isotropic material. For an anisotropic material this number is twenty-one, for an orthotropic material it is nine:  $E_{11}$ ,  $E_{22}$ ,  $E_{33}$ ,  $G_{12}$ ,  $G_{13}$ ,  $G_{23}$ ,  $\nu_{12}$ ,  $\nu_{13}$ , and  $\nu_{23}$  [8].

If the arrangement of fibres in the matrix is uniform, the material is assumed to be transversely isotropic (the transverse stiffness properties in a plane perpendicular to the fibre direction are independent of orientation). The result is that  $E_{22} = E_{33}$ ,  $G_{12} = G_{13}$ ,  $\nu_{12} = \nu_{13}$ . Also, it is known [6] that the out-of-plane shear modulus  $G_{23}$  is a function of  $E_{22}$ , and  $\nu_{23}$ :

$$G_{23} = \frac{E_{22}}{2(1 + \nu_{23})} \quad (2.1)$$

Therefore, the number of independent elastic constants required to describe a transversely isotropic material drops to only five:  $E_{11}$ ,  $E_{22}$ ,  $G_{12}$ ,  $\nu_{12}$  and  $\nu_{23}$ .

A number of models exist with the aim of determining the constituent material properties of a transversely isotropic lamina using the individually known properties of the fibre and matrix. These models range from a low-fidelity weighted average calculation, to higher fidelity models involving an exact elastic solution, energy theorems, or a numerical solution to an assumed cross section. It should be noted that all of the micro-mechanics models described here require that all fibres are perfectly bonded to the matrix, and the lamina is free of voids. Strain is assumed to be uniform throughout the cross section of the lamina.

Many of the models do not present a method of determining the last of the five aforementioned elastic constants: the transverse out-of-plane Poisson's ratio  $\nu_{23}$ . Christensen[9] presents a method showing that  $\nu_{23}$  can be calculated as a function of the known in-plane Poisson's Ratios  $\nu_{12}$ , and  $\nu_{21}$  using the following relationship:

$$\nu_{23} = \nu_{12} \frac{1 - \nu_{21}}{1 - \nu_{12}} \quad (2.2)$$

where:

$$\nu_{21} = \frac{E_{22}}{E_{11}} \nu_{12} \quad (2.3)$$

**Rule-of-Mixtures Model** The rule-of-mixtures model states that under the aforementioned assumptions, the effective fibre-direction properties can be calculated using a weighted average. This average is weighted by a factor known as the fibre volume fraction  $V_f$ : the ratio of fibre to matrix volume. In a cross section perpendicular to the fibre direction, the volume fraction is equal to the cross-sectional area-ratio of fibre to matrix.

The effective modulus  $E_{11}$  is calculated as shown in Equation 2.4. As expected, the effective modulus lies between that of the fibre and that of the matrix.

For the case of transverse modulus  $E_{22}$ , the fibre and matrix are in series and so the contribution of their individual moduli becomes additive (as with springs in series); the resulting relationship is shown in Equation 2.5.

$$E_{11} = E_f (V_f) + E_m (1 - V_f) \quad (2.4)$$

$$E_{22} = E_{33} = \frac{E_f E_m}{E_f - V_f (E_f - E_m)} \quad (2.5)$$

where:

$V_f$  = fibre volume fraction: ratio of fibre volume to matrix volume (equal to area fraction  $A_f$ )

$E_{11}$  = Effective elastic modulus of lamina in the fibre direction

$E_f$  = Longitudinal elastic modulus of the fibre

$E_m$  = Elastic modulus of the matrix

A similar derivation applying a shear stress to the fibres and matrix produces the following relation that describes the lamina shear modulus:

$$G_{12} = G_{21} = G_{13} = G_{31} = \frac{G_f G_m}{G_f - V_f (G_f - G_m)} \quad (2.6)$$

Note that because a unidirectional fibre-reinforced composite lamina is treated as transversely isotropic, the shear modulus  $G_{12} = G_{13}$ .

The major Poisson's ratio  $\nu_{12}$  can be found using the ratio of lateral to axial strain, giving a result similar to Equation 2.4. The minor Poissons ratio  $\nu_{21}$  is calculated using the conventional relationship shown in Equation 2.3.

$$\nu_{12} = \nu_{12_f} V_f + \nu_{12_m} (1 - V_f) \quad (2.7)$$

where:

$\nu_{12}$  = Major Poisson's ratio

$\nu_f$  = Poisson's ratio for fibre

$\nu_m$  = Poisson's ratio for matrix

The predictions given by the rule-of-mixtures model for  $E_{11}$  and  $\nu_{12}$  are generally accepted as accurate; the series calculations, however, are not as highly regarded. These transverse stiffness coefficients are under-predicted by the rule-of-mixtures model; this is likely caused by the inaccuracy of using a purely in-series stiffness calculation. It is easy to imagine a fibre geometry with fibres directly in contact with each other, or perhaps interlocked such that the matrix thickness between fibres is very small. A simple volume-fraction based series calculation puts more reliance on the moduli of the matrix than is the reality. In this case it makes sense that as volume fraction increases, predictions lose accuracy.

**Concentric-Cylinder Model** Hashin and Rosen[10] apply a concentric-cylinder model developed by Hill[11] that assumes a geometry consisting of parallel cylinders (fibres) of varying size inside concentric tubes (matrix). The range of radii has no lower bound; infinitesimally small cylinders ensure the cross-sectional area is fully occupied. Geometrically this model is clearly inaccurate – it is known that fibres are relatively uniform in size. Despite this, the predictions are said to be of a reasonable accuracy [5]. The model provides an exact elasticity solution for all but one of the five properties needed to model the stiffness of a transversely isotropic material. A method of modelling the undetermined property – transverse shear modulus – is presented by Christensen and Lo[12] as a quadratic whose terms are a function of fibre-volume fraction and material properties of the fibre and matrix.

**Halpin-Tsai Relationships** A set of curve-fitting relations were developed by Halpin and Tsai predicting stiffness coefficients based on a number of previously published high-fidelity micro-mechanics models. The derivation of the now well known 'Halpin-Tsai' relations is well outlined in [13], along with derivations from works which formed their foundation.

The existing rule-of-mixtures results are used for  $E_{11}$ , and  $\nu_{12}$ , while the previously under-predicted stiffness coefficients in the transverse direction are calculated using a curve fit. The Halpin-Tsai relations have been shown to model the transverse properties of a fibre-reinforced composite lamina with more accuracy. The relevant equations are shown as follows:

$$\frac{G_{12}}{G_m} = \frac{1 + \zeta \eta V_f}{1 - \eta V_f} \quad (2.8)$$



where:

$$\eta = \frac{G_{12_f}/G_{12_m} - 1}{G_{12_f}/G_{12_m} + \zeta} \quad (2.9)$$

and similarly, for the transverse modulus:

$$\frac{E_{22}}{E_m} = \frac{1 + \zeta\eta V_f}{1 - \eta V_f} \quad (2.10)$$

where:

$$\eta = \frac{E_{12_f}/E_m - 1}{E_{12_f}/E_m + \zeta} \quad (2.11)$$

and  $\zeta$  is a curve fitting factor.

### Characterization for a Unidirectional Lamina: Experimental Methods

As mentioned, physical testing is the primary method of establishing reliable material properties for fibre-reinforced composites. Relatively simple test procedures exist to find fibre-direction modulus  $E_{11}$ , Poisson's ratio  $\nu_{12}$ , transverse modulus  $E_{22}$ , and shear modulus  $G_{12}$ . These procedures are described in the following paragraphs.

**Fibre-Direction Tensile Testing:**  $E_{11}$ ,  $E_{22}$ ,  $\nu_{12}$  A tensile test of a unidirectional coupon with fibres oriented along the axis of loading can be used to establish the modulus  $E_{11}$ , and the Poisson's ratio  $\nu_{12}$ . The coupon is a high aspect-ratio rectangular prism with two compliant and strain-compatible tabs adhered to each end, sandwiching the test material. These adhered tabs serve to distribute the stress concentrations caused by wedge-style grippers. Longitudinal and transverse strains are measured using strain-gauges along and perpendicular to the fibre direction, respectively. The modulus  $E_{11}$  is simply the ratio of stress to strain measured in the longitudinal direction. The Poisson's ratio is found as the ratio of longitudinal strain to transverse strain:  $\nu_{12} = -\epsilon_1/\epsilon_2$ . An ASTM procedure is available (ASTM D-3039) which outlines exact coupon dimensions and strain rates.

The transverse modulus  $E_{22}$  is found with a similar test having fibre oriented perpendicular to the tensile loading direction. Although this could be used to obtain  $\nu_{21}$  in a manner analogous to how  $\nu_{12}$  is determined, this is not common practice as the strain being measured is generally an order of magnitude smaller than that associated with  $\nu_{12}$ . Instead the reciprocity relationship shown in Equation 2.3 can be exploited.

**Transverse Shear Testing:**  $G_{12}$  A number of methods exist for determination of the transverse shear modulus  $G_{12}$  [14].

The Iosipescu shear test was developed by Nicolai Iosipescu[15] for use in determining the shear properties of isotropic metals. It was later applied to composites materials by Walrath and Adams[16].

**Table 2.1:** Fibre-direction strain under various loading directions

Loading	Strain in Direction 1
$\sigma_1$	$\epsilon_1 = \sigma_1/E_{11}$
$\sigma_2$	$\epsilon_1 = -\nu_{21}\epsilon_2 = -\nu_{21}[\sigma_2/E_{22}]$
$\sigma_3$	$\epsilon_1 = -\nu_{31}\epsilon_3 = -\nu_{31}[\sigma_2/E_{33}]$

The test uses a specimen with V-notches cut into the top and bottom of the material as viewed from the side. The specimen is subjected to asymmetrical four point bending such that the transverse plane of interest is at a location of zero bending moment and experiences pure shear<sup>1</sup>. Strain gauges are placed at a 45° angle to the longitudinal axis of the specimen (and fibres). Specific information about the Iosipescu test is found in ASTM D-5379[17].

A method involving a more complicated test specimen is known as the torsion tube test. The test utilizes a thin-walled tube with fibres wound in the hoop direction. Advantages of the torsion tube test include the presence of well-defined stress fields and the ease of eliminating end-effects [5]. The method was found to show stiffness properties equivalent to those found with the Iosipescu test. A comparison can be found between the torsion tube test and the Iosipescu shear test in a manuscript by Swanson et al.[18].

Another method of shear modulus determination exists (ASTM 3518), in which a coupon consisting of  $\pm 45^\circ$  laminae is tested in the same manner as the aforementioned tensile coupon testing.

A difficulty exists in all methods of shear stiffness quantification for fibre-reinforced composites: the shear response is typically quite non-linear [18] [19].

### Macro-Mechanics: Stress-Strain Response of a Lamina

The objective of the preceding Section 2.2.5 is the characterization of a single unidirectional lamina by virtue of predicting five elastic constants. The current section discusses methodology regarding use of these elastic constants to model the stress-strain response of a unidirectional lamina, with loading at an angle offset to the fibre direction.

Consider a single ply (lamina) of unidirectional-fibre composite with three orthogonal normal loadings applied. Assume that the material is loaded exactly along and transverse to its fibre direction. The effect of the loading in each direction on the strain in the fibre direction is shown in Table 2.1. Loading  $\sigma_1$  in the fibre direction causes an elastic response; loadings  $\sigma_2$  and  $\sigma_3$  transverse to the fibre direction cause strain through Poisson's ratio effects. It follows that the fibre-direction strain  $\epsilon_1$  under these three loadings can be expressed as the superposition of the effect from each loading. This relationship is shown in Equation 2.12.

<sup>1</sup>Stress concentrations exist near the V-notches of the specimen, but analyses have shown pure shear to exist at the center of the specimen.

$$\epsilon_1 = \sigma_1/E_{11} - \nu_{21}[\sigma_2/E_{22}] - \nu_{31}[\sigma_3/E_{33}] \quad (2.12)$$

Similar relations hold for strains in the other directions and the complete stress-strain relationship can be conveniently shown in a matrix equation:

$$\begin{Bmatrix} \epsilon_1 \\ \epsilon_2 \\ \epsilon_3 \\ \gamma_{23} \\ \gamma_{31} \\ \gamma_{12} \end{Bmatrix} = \begin{bmatrix} 1/E_{11} & -\nu_{21}/E_{22} & -\nu_{31}/E_{33} & 0 & 0 & 0 \\ -\nu_{12}/E_{11} & 1/E_{22} & -\nu_{32}/E_{33} & 0 & 0 & 0 \\ -\nu_{13}/E_{11} & -\nu_{23}/E_{22} & 1/E_{33} & 0 & 0 & 0 \\ 0 & 0 & 0 & 1/G_{23} & 0 & 0 \\ 0 & 0 & 0 & 0 & 1/G_{31} & 0 \\ 0 & 0 & 0 & 0 & 0 & 1/G_{12} \end{bmatrix} \begin{Bmatrix} \sigma_1 \\ \sigma_2 \\ \sigma_3 \\ \tau_{23} \\ \tau_{31} \\ \tau_{12} \end{Bmatrix} \quad (2.13)$$

or

$$\{\epsilon\} = [S_{3D}]\{\sigma\} \quad (2.14)$$

where  $S_{3D}$  is the three-dimensional compliance matrix for an orthotropic lamina.

With fibre-reinforced composites it is quite common that the thickness of a laminate is very small in comparison with length and width. In this case it is generally<sup>1</sup> reasonable to assume that the through-thickness stresses are negligible, or rather that material exhibits a state of plane stress – strain is not restrained in the through-thickness direction, but assumed negligible. This assumption reduces the compliance matrix in Equation 2.13 to the three by three matrix shown in Equation 2.15.

$$\begin{Bmatrix} \epsilon_1 \\ \epsilon_2 \\ \gamma_{12} \end{Bmatrix} = \begin{bmatrix} 1/E_{11} & -\nu_{21}/E_{22} & 0 \\ -\nu_{12}/E_{11} & 1/E_{22} & 0 \\ 0 & 0 & 1/G_{12} \end{bmatrix} \begin{Bmatrix} \sigma_1 \\ \sigma_2 \\ \tau_{12} \end{Bmatrix} \quad (2.15)$$

Inverting the compliance matrix in Equation 2.15 produces the lamina stiffness matrix  $Q$  such that

$$\begin{Bmatrix} \sigma_{11} \\ \sigma_{22} \\ \tau_{12} \end{Bmatrix} = \begin{bmatrix} Q_{11} & Q_{12} & 0 \\ Q_{21} & Q_{22} & 0 \\ 0 & 0 & Q_{66} \end{bmatrix} \begin{Bmatrix} \epsilon_{11} \\ \epsilon_{22} \\ \gamma_{12} \end{Bmatrix} \quad (2.16)$$

or

$$\{\sigma\} = [Q]\{\epsilon\} \quad (2.17)$$

<sup>1</sup>Even with thin laminates cases exist where through-thickness stress facilitates a failure mode. An example is the “free-edge effect” phenomenon in which through-thickness shear develops with the attenuation of in-plane shear at the free edge of a stressed laminate.

where

$$Q_{11} = \frac{E_{11}}{1 - \nu_{12}\nu_{21}} \quad (2.18)$$

$$Q_{22} = \frac{E_{22}}{1 - \nu_{12}\nu_{21}} \quad (2.19)$$

$$Q_{12} = Q_{21} = \frac{\nu_{12}E_{22}}{1 - \nu_{12}\nu_{21}} = \frac{\nu_{21}E_{11}}{1 - \nu_{12}\nu_{21}} \quad (2.20)$$

$$Q_{66} = G_{12} \quad (2.21)$$

The stress-strain relationship of Equation 2.16 is valid only when the coordinate system of loading coincides with the material-fibre coordinate system. It is very rare that a laminate does not have at least some laminae with fibre-directions offset from the loading direction. This is due to the large differential in transverse versus longitudinal stiffness and strength of continuous-fibre composites.

It becomes necessary to define a matrix which allows the stress-strain relation to be extended to a lamina with fibres oriented at any angle. This is achieved by applying standard transformation procedures which can be found in any mechanics of materials text. The resulting relation is shown in Equation 2.22 containing the lamina stiffness matrix  $\bar{\mathbf{Q}}$  that allows stress-strain relation for a transversely isotropic material with its principal material axis arbitrarily oriented in the plane of the lamina.

$$\begin{Bmatrix} \sigma_{xx} \\ \sigma_{yy} \\ \tau_{xy} \end{Bmatrix} = \begin{bmatrix} \bar{Q}_{11} & \bar{Q}_{12} & \bar{Q}_{16} \\ \bar{Q}_{21} & \bar{Q}_{22} & \bar{Q}_{26} \\ \bar{Q}_{61} & \bar{Q}_{62} & \bar{Q}_{66} \end{bmatrix} \begin{Bmatrix} \epsilon_{xx} \\ \epsilon_{yy} \\ \gamma_{xy} \end{Bmatrix} = [\bar{\mathbf{Q}}] \begin{Bmatrix} \epsilon_{xx} \\ \epsilon_{yy} \\ \gamma_{xy} \end{Bmatrix} \quad (2.22)$$

where:

$\sigma_{xx}$  = normal stress in the  $x$  direction

$\sigma_{yy}$  = normal stress in the  $y$  direction

$\tau_{xy}$  = in-plane  $x$ - $y$  shear stress

$\epsilon_{xx}$  = normal strain in the  $x$  direction

$\epsilon_{yy}$  = normal strain in the  $y$  direction

$\gamma_{xy}$  = in-plane  $x$ - $y$  shear strain

The elements in the  $\bar{\mathbf{Q}}$  matrix are calculated as [6]:

$$\begin{aligned}
\bar{Q}_{11} &= Q_{11} \cos^4 \theta + 2(Q_{12} + 2Q_{66}) \sin^2 \theta \cos^2 \theta + Q_{22} \sin^4 \theta \\
\bar{Q}_{12} = \bar{Q}_{21} &= Q_{12} (\sin^4 \theta + \cos^4 \theta) + (Q_{11} + Q_{22} - 4Q_{66}) \sin^2 \theta \cos^2 \theta \\
\bar{Q}_{22} &= Q_{11} \sin^4 \theta + 2(Q_{12} + 2Q_{66}) \sin^2 \theta \cos^2 \theta + Q_{22} \cos^4 \theta \\
\bar{Q}_{16} = \bar{Q}_{61} &= (Q_{11} - Q_{12} - 2Q_{66}) \sin \theta \cos^3 \theta + (Q_{12} - Q_{22} + 2Q_{66}) \sin^3 \theta \cos \theta \\
\bar{Q}_{26} = \bar{Q}_{62} &= (Q_{11} - Q_{12} - 2Q_{66}) \sin^3 \theta \cos \theta + (Q_{12} - Q_{22} + 2Q_{66}) \sin \theta \cos^3 \theta \\
\bar{Q}_{66} &= (Q_{11} + Q_{22} - 2Q_{12} - 2Q_{66}) \sin^2 \theta \cos^2 \theta + Q_{66} (\sin^4 \theta + \cos^4 \theta)
\end{aligned} \tag{2.23}$$

where  $\theta$  is the angle of the fibres within the lamina, relative to the  $x$  axis of the  $x$ - $y$ - $z$  coordinate system.

In Section 2.2.6 that follows, the usefulness of Equation 2.22 will come into focus as one moves from analysis of a single lamina to analysis of a laminate with numerous layers of arbitrary fibre angle. In preparation for a multi-lamina analysis, the  $\bar{\mathbf{Q}}$  matrix is rewritten for a given lamina  $k$  as  $\bar{\mathbf{Q}}_k$  and Equation 2.22 is re-written in a manner that is specific to lamina  $k$ :

$$\begin{Bmatrix} \sigma_{xx_k} \\ \sigma_{yy_k} \\ \tau_{xy_k} \end{Bmatrix} = \begin{bmatrix} \bar{Q}_{11_k} & \bar{Q}_{12_k} & \bar{Q}_{16_k} \\ \bar{Q}_{21_k} & \bar{Q}_{22_k} & \bar{Q}_{26_k} \\ \bar{Q}_{61_k} & \bar{Q}_{62_k} & \bar{Q}_{66_k} \end{bmatrix} \begin{Bmatrix} \epsilon_{xx_k} \\ \epsilon_{yy_k} \\ \gamma_{xy_k} \end{Bmatrix} = [\bar{\mathbf{Q}}_k] \begin{Bmatrix} \epsilon_{xx_k} \\ \epsilon_{yy_k} \\ \gamma_{xy_k} \end{Bmatrix} \tag{2.24}$$

where:

- $\sigma_{xx_k}$  = normal stress in the  $x$  direction within lamina  $k$
- $\sigma_{yy_k}$  = normal stress in the  $y$  direction within lamina  $k$
- $\tau_{xy_k}$  = in-plane  $x$ - $y$  shear stress within lamina  $k$
- $\epsilon_{xx_k}$  = normal strain in the  $x$  direction within lamina  $k$
- $\epsilon_{yy_k}$  = normal strain in the  $y$  direction within lamina  $k$
- $\gamma_{xy_k}$  = in-plane  $x$ - $y$  shear strain within lamina  $k$

## 2.2.6 Lamination Theory

Classical Laminated Plate Theory (CLPT) is probably the most widely used theory in the analysis of fibre-reinforced composites. The theory is useful in the analysis of thin-walled composite structures with distinct layers in which continuous fibres have a uniform direction; these distinct layers – or laminae – make up a laminate. Classical laminated plate theory provides a means of calculating stresses and strains in each lamina of a laminate structure subjected to a set of in-plane loads and bending moments.

A number of assumptions are necessary to maintain the validity of using CLPT for a given structure [6][5]:

- The thickness of the laminate is of a significantly smaller dimension than the width and length.
- All laminae are perfectly bonded to each-other.
- Each lamina is of uniform thickness, is orthotropic and homogeneous in nature, and behaves as a linear elastic material.
- The through thickness distribution of in-plane strain is linear, and the laminate adheres to the Kirchoff-Love assumptions: straight lines normal to the mid-surface remain straight and normal throughout deformation.

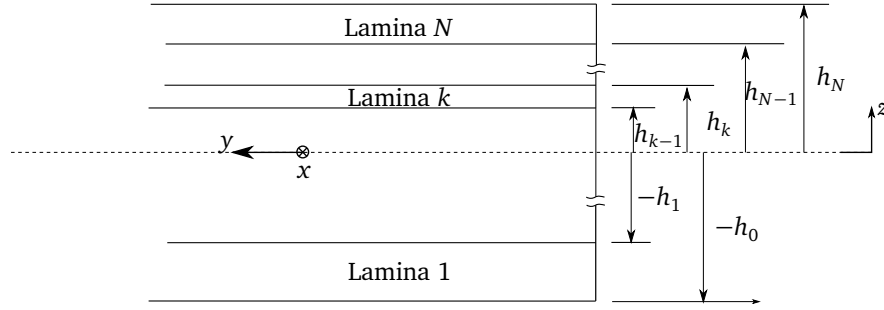


Figure 2.3: Notation and dimensions for the discussed laminate

Consider the flat laminate shown in Figure 2.3 with an  $x, y$  coordinate system located in its mid-plane, containing  $N$  laminae. It has been shown [5] that for an arbitrary set of mid-plane strains and curvatures, the corresponding in-plane strains in each lamina  $k$  are as follows:

$$\begin{aligned}
 \epsilon_{xx_k} &= \frac{\partial u}{\partial x} - z_k \frac{\partial^2 w}{\partial x^2} \\
 \epsilon_{yy_k} &= \frac{\partial v}{\partial y} - z_k \frac{\partial^2 w}{\partial y^2} \\
 \gamma_{xy_k} &= \frac{\partial u}{\partial y} + \frac{\partial v}{\partial x} - 2z_k \frac{\partial^2 w}{\partial x \partial y}
 \end{aligned} \tag{2.25}$$

where:

$u, v,$  and  $w$  represent displacements in the  $x, y,$  and  $z$  directions, respectively.

$\epsilon_{xx_k}$  = normal strain in the  $x$  direction within lamina  $k$

$\epsilon_{yy_k}$  = normal strain in the  $y$  direction within lamina  $k$

$\gamma_{xy_k}$  = in-plane  $x$ - $y$  shear strain (engineering strain) within lamina  $k$

$z_k$  = distance between the mid-plane of lamina  $k$  and the mid-plane of the laminate, referred to as lamina elevation

or, in a more compact and useful format:

$$\begin{pmatrix} \epsilon_{xx_k} \\ \epsilon_{yy_k} \\ \gamma_{xy_k} \end{pmatrix} = \begin{pmatrix} \epsilon_{xx_k}^0 \\ \epsilon_{yy_k}^0 \\ \gamma_{xy_k}^0 \end{pmatrix} + z_k \begin{pmatrix} \kappa_{xx} \\ \kappa_{yy} \\ \kappa_{xy} \end{pmatrix} \quad (2.26)$$

where:

$\epsilon_{xx}^0$  = mid-plane normal strain in the  $x$  direction of the laminate

$\epsilon_{yy}^0$  = mid-plane normal strain in the  $y$  direction of the laminate

$\gamma_{xy}^0$  = mid-plane in-plane  $x$ - $y$  shear strain (engineering strain) in the laminate

$\kappa_{xx}$  = bending curvature of the laminate in the  $x$ - $z$  plane

$\kappa_{yy}$  = bending curvature of the laminate in the  $y$ - $z$  plane

$\kappa_{xy}$  = twisting curvature of the laminate

A set of stress resultants  $\{N\}$  is defined as the integration of stresses over the thickness of the laminate; these terms manifest themselves as applied force per unit width. Similarly, a set of moment resultants  $\{M\}$  is applied moment per unit width. The convention and nomenclature relating to these resultants can be seen in Figure 2.4. The mathematical definitions of  $\{N\}$  and  $\{M\}$  are shown below as an equilibrium summation with force resultants equated to the integral of stress, and moment resultants equated to the integral of stress multiplied by distance from the center line:

$$\begin{pmatrix} N_{xx} \\ N_{yy} \\ N_{xy} \end{pmatrix} = \int_{-h}^h \begin{pmatrix} \sigma_{xx} \\ \sigma_{yy} \\ \tau_{xy} \end{pmatrix} dz \quad (2.27)$$

$$\begin{pmatrix} M_{xx} \\ M_{yy} \\ M_{xy} \end{pmatrix} = \int_{-h}^h \begin{pmatrix} \sigma_{xx} \\ \sigma_{yy} \\ \tau_{xy} \end{pmatrix} z dz \quad (2.28)$$

where  $h$  is half the total thickness of the laminate.

Using the constitutive relationships in 2.22 developed for a single orthotropic lamina at an arbitrary angle, the stress matrices in Equations 2.27, 2.28 can be replaced by  $[\bar{Q}]\{\epsilon\}$ . A summation across all laminae is necessary to relate the force and moment resultants to strains in the laminate – for example:

$$N_{xx} = \sum_{k=1}^N \int_{h_{k-1}}^{h_k} \sigma_{xx_k} dz \quad (\text{See Figure 2.3})$$

The integral in the example shown is easily integrated over the constant material properties of each

lamina. Doing this for each resultant equation yields the following:

$$A_{mn} = \sum_{k=1}^N (\bar{Q}_{mn_k} (h_k - h_{k-1})) \quad ; \quad [\mathbf{A}] = \begin{bmatrix} A_{11} & A_{12} & A_{16} \\ A_{21} & A_{22} & A_{26} \\ A_{61} & A_{62} & A_{66} \end{bmatrix} \quad (2.29)$$

$$B_{mn} = \frac{1}{2} \sum_{k=1}^N (\bar{Q}_{mn_k} (h_k^2 - h_{k-1}^2)); \quad [\mathbf{B}] = \begin{bmatrix} B_{11} & B_{12} & B_{16} \\ B_{21} & B_{22} & B_{26} \\ B_{61} & B_{62} & B_{66} \end{bmatrix} \quad (2.30)$$

$$D_{mn} = \frac{1}{3} \sum_{k=1}^N (\bar{Q}_{mn_k} (h_k^3 - h_{k-1}^3)); \quad [\mathbf{D}] = \begin{bmatrix} D_{11} & D_{12} & D_{16} \\ D_{21} & D_{22} & D_{26} \\ D_{61} & D_{62} & D_{66} \end{bmatrix} \quad (2.31)$$

where:

$N$  = total number of laminae

$\bar{Q}_{mn_k}$  =  $mn$  term of the  $\bar{\mathbf{Q}}_k$  matrix for the  $k^{\text{th}}$  lamina

$A_{mn}$  =  $mn$  term of the  $\mathbf{A}$  matrix for the laminate

$B_{mn}$  =  $mn$  term of the  $\mathbf{B}$  matrix for the laminate

$D_{mn}$  =  $mn$  term of the  $\mathbf{D}$  matrix for the laminate

$h_{k-1}$  = distance from the mid-plane of the laminate to the bottom surface of the  $k^{\text{th}}$  lamina

$h_k$  = distance from the mid-plane of the laminate to the top surface of the  $k^{\text{th}}$  lamina

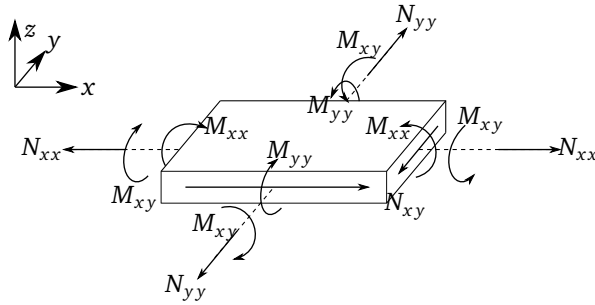


Figure 2.4: Moments and forces on an element in lamination theory

The  $\mathbf{A}$ ,  $\mathbf{B}$ , and  $\mathbf{D}$  matrices are used to form a larger matrix  $\mathbf{C}$ , known as the laminate stiffness matrix.

$$\text{Laminate stiffness matrix} = [\mathbf{C}] = \begin{bmatrix} [\mathbf{A}] & [\mathbf{B}] \\ [\mathbf{B}] & [\mathbf{D}] \end{bmatrix} \quad (2.32)$$



The stiffness matrix relates forces and moments applied to the laminate to mid-plane strains and curvatures:

$$\begin{pmatrix} N_{xx} \\ N_{yy} \\ N_{xy} \\ M_{xx} \\ M_{yy} \\ M_{xy} \end{pmatrix} = \begin{bmatrix} A_{11} & A_{12} & A_{16} & B_{11} & B_{12} & B_{16} \\ A_{21} & A_{22} & A_{26} & B_{21} & B_{22} & B_{26} \\ A_{61} & A_{62} & A_{66} & B_{61} & B_{62} & B_{66} \\ B_{11} & B_{12} & B_{16} & D_{11} & D_{12} & D_{16} \\ B_{21} & B_{22} & B_{26} & D_{21} & D_{22} & D_{26} \\ B_{61} & B_{62} & B_{66} & D_{61} & D_{62} & D_{66} \end{bmatrix} \begin{pmatrix} \epsilon_{xx}^0 \\ \epsilon_{yy}^0 \\ \gamma_{xy}^0 \\ k_{xx} \\ k_{yy} \\ k_{xy} \end{pmatrix} \quad (2.33)$$

where:

$N_{xx}$  = normal force in the  $x$  direction, per unit width of laminate

$N_{yy}$  = normal force in the  $y$  direction, per unit width of laminate

$N_{xy}$  = in-plane  $x$ - $y$  shear force, per unit width of laminate

$M_{xx}$  = bending moment in the  $x$ - $z$  plane, per unit width of laminate

$M_{yy}$  = bending moment in the  $y$ - $z$  plane, per unit width of laminate

$M_{xy}$  = twisting moment per unit width of laminate

Strains and curvatures can be defined as a function of applied resultant forces and moments by inverting the stiffness matrix  $\mathbf{C}$  to obtain the compliance matrix  $\mathbf{S}$ :

$$\text{Laminate compliance matrix} = [\mathbf{S}] = [\mathbf{C}]^{-1} = \begin{bmatrix} [\mathbf{a}] & [\mathbf{b}] \\ [\mathbf{b}]^T & [\mathbf{d}] \end{bmatrix} \quad (2.34)$$

With a compliance matrix defined, Equation 2.33 can be modified to take the form:

$$\begin{pmatrix} \epsilon_{xx}^0 \\ \epsilon_{yy}^0 \\ \gamma_{xy}^0 \\ k_{xx} \\ k_{yy} \\ k_{xy} \end{pmatrix} = \begin{bmatrix} a_{11} & a_{12} & a_{16} & b_{11} & b_{12} & b_{16} \\ a_{21} & a_{22} & a_{26} & b_{21} & b_{22} & b_{26} \\ a_{61} & a_{62} & a_{66} & b_{61} & b_{62} & b_{66} \\ b_{11} & b_{21} & b_{61} & d_{11} & d_{12} & d_{16} \\ b_{12} & b_{22} & b_{62} & d_{21} & d_{22} & d_{26} \\ b_{16} & b_{26} & b_{66} & d_{61} & d_{62} & d_{66} \end{bmatrix} \begin{pmatrix} N_{xx} \\ N_{yy} \\ N_{xy} \\ M_{xx} \\ M_{yy} \\ M_{xy} \end{pmatrix} \quad (2.35)$$

## 2.2.7 Elastic Coupling of Composite Laminates

The anisotropic nature of a unidirectional lamina subjected to loading at an angle to the fibre direction results in a shear coupling effect. This effect is seen in Equation 2.22 when the  $\bar{Q}_{16}$  term is non-zero, as it will be for any off-axis unidirectional lamina. The effect is also depicted in Figure 2.5 for clarity. It is

worth noting that the coupling is independent of which stress is applied: shear stress will result in axial stress by virtue of a non-zero  $\bar{Q}_{61}$  term.

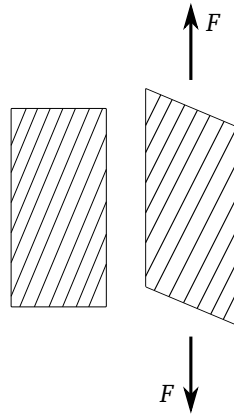


**Figure 2.5:** Undeformed and deformed shape of a unidirectional lamina with off-axis loading

Typical laminates consist of many layers, each having a potentially different fibre-angle or a different fibre entirely. The mismatch of degree to which each layer exhibits extensional-shear coupling results in interesting and sometimes counter-intuitive behaviour of the laminate as a whole. The elastic behaviour depends very much on the architecture of the laminate; three special classes of laminate architecture are defined as follows:

### Balanced Laminates

A balanced laminate exists when each lamina with fibre-angle  $\theta$  is balanced by a lamina of equal thickness at fibre-angle  $-\theta$ . For balanced laminates, the  $A_{16}$  and  $A_{26}$  terms of the **A** matrix in Equation 2.32 are zero; removing any extensional-shear coupling.

### Symmetric Laminates

A symmetric laminate exists when symmetry of fibre angle, and lamina thickness can be found with respect to a plane halfway through the thickness of the laminate. Each lamina above the mid-plane has a matching lamina below and at the same distance from the mid-plane. For symmetric laminates, the entire **B** matrix of Equation 2.32 goes to zero; this eliminates extensional-bending, extensional-twisting, shear-bending, and shear-twisting coupling.

### Anti-Symmetric Laminates

An anti-symmetric laminate exists when for each fibre angle  $\theta$ , there is a fibre-angle  $-\theta$  of equal thickness at an equal distance from the mid-plane.

In the interest of clarity, the coupling to be expected is summarized for the aforementioned special cases of laminate architecture in Table 2.2. Two cases are not shown in the table:

1. A laminate that is both balanced and symmetric. In this case the expected coupling may be resolved by superposition of the corresponding columns, resulting in only bending-twisting coupling.
2. A laminate that is neither balanced nor symmetric, which has the potential to exhibit all forms of coupling.

**Table 2.2:** Elastic coupling in various classes of laminate architecture (reproduced and adapted with permission from [20])

Type of Coupling	Laminate Architecture		
	Balanced	Symmetric	Balanced Anti-symmetric
<b>Extensional-Shear</b>	None	May be present	None
<b>Extensional-Bending</b>	May be present	None	None
<b>Bending-Twisting</b>	May be present	May be present	None
<b>Shear-Bending</b>	May be present	None	May be present
<b>Shear-Twisting</b>	May be present	None	None
<b>Extensional-Twisting</b>	May be present	None	May be present

## 2.3 Review of Current Literature

The first instance found in the open literature of an analytical solution for mechanical loading of a cylindrically anisotropic cylinder belongs to Lekhnitskii[21]; he establishes the governing partial differential equations for analysis of a single cylindrical tube of anisotropic material loaded axisymmetrically. Many of the manuscripts to be discussed build upon Lekhnitskii's formalism, expanding the theory to account for multiple layers in a laminate.

Sherrer[22] presents a theoretical elastic solution for filament-wound cylinders having any number of layers with any fibre-angle in each layer. The presented solution is claimed valid for axial-symmetric (axial, torsional, and pressure) loading of thin or thick-walled tubes. Sherrer takes the stress-strain relations for an orthotropic material used by Cutler[23] and combines them with element equilibrium equations extracted from Timoshenko's text[24] to arrive at matrix expressions for strain and stress. Compatibility is then enforced by equating stresses and displacements at layer interfaces allowing treatment of laminated cylinders.

Important points are made by Pagano, Halpin and Whitney[25] regarding the existence of a uniform stress field as well as the influence of end constraints in the axial-force mechanical testing of cylindrically anisotropic tubes. It is noted that a uniform stress field is possible only as thickness approaches zero for

specimens subjected to uniaxial tension with one end free to rotate. When both ends are rigidly held against rotation and axial tension is applied, an approximately uniform stress field is possible; however, the resulting axial modulus will be significantly different from the unrestrained case. The rigid-constraint configuration results in shear stress (torque) in the material, and can lead to instability (torsional buckling) in thin-walled cylinders. Pagano and Whitney[26] perform a quantitative investigation on the stress fields present in highly anisotropic cylinders subjected to simple loadings. A procedure is presented that serves to quantify the elastic stress gradients present through the thickness as well as along the length of a tube under axial loading, torsional loading, and pressure loading. Parametric studies are provided that shed light on the sensitivity of through-thickness stress uniformity to parameters such as tube thickness ratio and degree of material anisotropy. Normal, shear, and hoop stresses are examined, corresponding to axial, torsional, and pressure loading, respectively. It is shown that stress gradients are significantly reduced in symmetrically laminated cylinders. Further study of stress gradients in a symmetric angle-ply laminate is presented by Pagano[27] as somewhat of an addendum to [26].

Reissner and Tsai[28] present an analysis demonstrating that orthotropic laminated cylindrical shells exhibit a significant reduction in their bending and stretching stiffness factors when a longitudinal slit is present. An analogous and well known phenomenon exists with torsion of homogeneous shells, but no such effect is seen when comparing the axial or bending stiffness of closed versus open cross-section tubes.

The elastic behaviour of a system of coaxial orthotropic cylinders loaded in tension, torsion, and bending is analysed by Jolicoeur and Cardou[29] by expanding upon the work of Lekhnitskii. The treatment of multiple layers is accomplished by stipulation of boundary conditions at the interfaces between individual cylinders; cases of both no-slip and no-friction are investigated. Numerical results show a development of cross-section warping during bending; the effect is pronounced in the no-friction case, but less so in the no-slip case. This result has implications on the validity of using a Euler-Bernoulli hypothesis to model bending of cylindrically anisotropic cylinders. Extension, torsion, outer and inner surface tractions, and pressurizing of a cylindrically anisotropic tube are investigated by Ting[30] and subsequently by Chen et al.[31]. These authors assume that stress distribution is a function of radial distance. Chouchaoui and Ochoa[32] extend the analysis of Jolicoeur and Cardou[29] to include tensile, torsion, bending, and pressure loading of laminated cylindrically anisotropic tubes.

A so-called 'state space approach' is presented by Tarn and Wang[33] as a solution to the problem of a cylindrically anisotropic layered tube under extension, torsion, bending, constant surface traction, and pressurizing. Again, Lekhnitskii's[21] differential equations are used as a starting point. The equations of anisotropic elasticity are formulated in the cylindrical coordinate system and arranged to form a system matrix that is independent of radius; this allows the state equation to be solved with matrix algebra. The result shows an axisymmetric state of stress caused by extension, torsion, pressurizing, and constant surface tractions, and an axially asymmetric state of stress caused by bending. In a subsequent

publication, Tarn[34] updates the approach to handle temperature change and body-force.

In summary, a number of theories that aim to describe the elastic response of cylindrically anisotropic tubes are present in the literature; the majority are based upon Lekhnitskii's stress functions and are limited to axisymmetric loadings. A few authors extend the analysis to include the asymmetric effects of bending, namely Jolicoeur et al.[29], and Chouchaoui et al.[32]. All of the discussed analyses that are based on the Lekhnitskii stress functions involve first finding an elasticity solution for each layer or lamina, and then stipulating the boundary conditions on each layer to enforce compatibility. Ultimately this layer-by-layer approach results in large and unwieldy systems of equations that need to be solved before constants in the stress and displacement equations can be determined. The 'state space' solution presented by Tarn and Wang[33] is probably the most comprehensive model in the literature, accounting for tensile, torsion, bending, traction (outer and inner surface), and pressure loading. Despite the misleading use of the term shearing when referring to surface tractions, the authors make no attempt at handling a transverse shear loading. Moreover, the bending solution that is presented as exact does not account for bending-shear coupling – a phenomenon present in all cases of cylindrically anisotropic materials subjected to bending, excluding the special case of cylindrical orthotropy.

## Chapter 3

# Laminated Cylinder Model

In the case of a thin-walled laminated composite tube, it is appropriate to use CLPT to obtain a smeared set of properties that describe the behaviour of the laminate and use those properties to predict the elastic response of the tube. However, this method loses validity as the ratio of tube thickness to diameter increases. At higher thickness-to-diameter ratios, the outermost layers have a more pronounced effect on the behaviour of the tube than the inner layers; the outer layers are at a larger radius and contribute more to the overall elastic behaviour of the tube. To account for the area differential as well as the difference in elastic contribution between outer and inner layers, a through-thickness integration that accounts for radius is necessary. This chapter presents an analytical model that accounts for these points, and details its derivation. Discussion about the assumptions and implications is included.

### 3.1 Overview

Consider a layered FRP tube with a global  $x$ - $y$ - $z$  coordinate system having its  $x$  axis aligned axially with the tube. Allow a local  $i$ - $j$ - $k$  coordinate system to exist with its  $k$  axis aligned radially at the point of interest. The tube is shown in Figure 3.1 in an arbitrary state of deformation, where the stress state at any point in layer  $n$  can be described with respect to the local  $i$ - $j$ - $k$  coordinate system by six values:  $\sigma_{ii_n}$ ,  $\sigma_{jj_n}$ ,  $\sigma_{kk_n}$ ,  $\tau_{ij_n}$ ,  $\tau_{ik_n}$ , and  $\tau_{jk_n}$ . With the assumption of zero through-thickness stress, the number of values required to describe the stress state at any point reduces to three:  $\sigma_{ii_n}$ ,  $\sigma_{jj_n}$ , and  $\tau_{ij_n}$ . It should be mentioned here that it will later become necessary to include  $\tau_{ik_n}$  in the derivation that follows; the reason will be evident. It was shown in Equation 2.22 that a set of stresses in a given coordinate system can be related to strains in that coordinate system by the  $\bar{Q}$  matrix; applying this approach to the current

consideration gives:

$$\begin{Bmatrix} \sigma_{ii_n} \\ \sigma_{jj_n} \\ \tau_{ij_n} \end{Bmatrix} = \begin{bmatrix} \bar{Q}_{11_n} & \bar{Q}_{12_n} & \bar{Q}_{16_n} \\ \bar{Q}_{21_n} & \bar{Q}_{22_n} & \bar{Q}_{26_n} \\ \bar{Q}_{16_n} & \bar{Q}_{26_n} & \bar{Q}_{66_n} \end{bmatrix} \begin{Bmatrix} \epsilon_{ii_n} \\ \epsilon_{jj_n} \\ \gamma_{ij_n} \end{Bmatrix} \quad (3.1)$$

or, for clarity:

$$\sigma_{ii_n} = \bar{Q}_{11_n} \epsilon_{ii_n} + \bar{Q}_{12_n} \epsilon_{jj_n} + \bar{Q}_{16_n} \gamma_{ij_n} \quad (3.2)$$

$$\sigma_{jj_n} = \bar{Q}_{21_n} \epsilon_{ii_n} + \bar{Q}_{22_n} \epsilon_{jj_n} + \bar{Q}_{26_n} \gamma_{ij_n} \quad (3.3)$$

$$\tau_{ij_n} = \bar{Q}_{16_n} \epsilon_{ii_n} + \bar{Q}_{26_n} \epsilon_{jj_n} + \bar{Q}_{66_n} \gamma_{ij_n} \quad (3.4)$$

where the elements of the  $\bar{Q}_n$  matrix are as described in Equation 2.23, leaving only the strains  $\epsilon_{ii}$ ,  $\epsilon_{jj}$ , and  $\gamma_{ij}$  as unknowns.

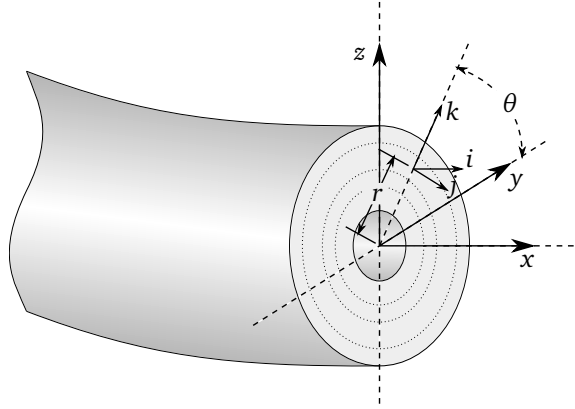


**Figure 3.1:** Local and global coordinate systems for a layered FRP tube in arbitrary state of deformation

Expressions are formed for  $\epsilon_{ii}$ ,  $\epsilon_{jj}$ , and  $\gamma_{ij}$  and substituted into Equations 3.2, 3.3, and 3.4 such that  $\sigma_{ii_n}$ ,  $\sigma_{jj_n}$ , and  $\tau_{ij_n}$  can be expressed as a function of lamina properties ( $\bar{Q}_n$  matrix terms), state of strain, and location ( $\theta$ ) in the cross-sectional plane of interest.

Just as in Kirchoff-Love plate analysis, longitudinal strain  $\epsilon_{ii}$  is calculated as the superposition of midplane strain (or in the current case, axial strain) and strain caused by bending curvature  $\kappa$ . Note that it is necessary to use the relevant elevation from the axis of curvature, seen in Equation 3.5 as  $\cos\theta$  and  $\sin\theta$  terms, multiplied by radius. The  $\kappa_z$  term is negative in accordance with the chosen coordinate systems – a positive curvature  $\kappa_z$  results in negative strain  $\epsilon_{ii}$  at positive values of  $r\cos\theta$ .

$$\epsilon_{ii} = \epsilon_{xx}^0 + \kappa_y r \sin\theta - \kappa_z r \cos\theta \quad (3.5)$$

An expression is required for  $\epsilon_{jj}$  that will allow the superposition of uniform diametric expansion

strain  $\epsilon_D$  and the non-uniform transverse strain caused by bending and Poisson's ratio effects. A transverse strain gradient is defined with respect to the  $y$  and  $z$  axes as  $\frac{d\epsilon_{jj}}{dz}$  and  $\frac{d\epsilon_{jj}}{dy}$ , respectively. These strain gradients do not have direct relevance, but are needed to quantify the relationship between transverse strain and elevation from the axis of curvature. The transverse strain is assumed to vary linearly with elevation from the neutral axis (this assumption is based upon classical Euler beam theory). The transverse strains discussed occur as a result of normal strain (Poisson's ratio effects). Equation 3.6 provides the desired superposition of uniform and non-uniform transverse strains.

$$\epsilon_{jj} = \epsilon_D + \frac{d\epsilon_{jj}}{dz} r \sin\theta + \frac{d\epsilon_{jj}}{dy} r \cos\theta \quad (3.6)$$

The transverse shear  $\gamma_{ij}$  is induced by torsional deformation of the tube, as well as shear deformation. A rate of twist  $\frac{d\phi}{dx}$  that relates torsional deformation and strain in a particular lamina at radius  $r$  is defined. To relate shear deformation of the tube to local shear deformation in a lamina, a conversion must be made between the global  $x$ - $y$ - $z$  coordinate system, and the local  $i$ - $j$ - $k$  coordinate system that follows the lamina. A conventional strain transformation procedure will show that the local shear strain caused by transverse shear can be expressed as  $\gamma_{ij_{shear}} = \gamma_{xy} \sin\theta - \gamma_{xz} \cos\theta$  where  $\theta$  denotes the angle between the horizontal, or rather the global  $y$  axis, and the  $k$  axis of the local coordinate system. Again a superposition is employed and the full local-shear-strain expression is seen in Equation 3.7.

$$\gamma_{ij} = -r \frac{d\phi}{dx} + \gamma_{xy} \sin\theta - \gamma_{xz} \cos\theta \quad (3.7)$$

Each of the three strain expressions presented contains three terms; consequently, a total of nine terms are necessary to fully describe the arbitrary state of strain under consideration. In a manner that draws a parallel to CLPT, a 9x9 stiffness matrix  $\mathbf{M}$  can be defined such that it embodies the relationship between loadings and elastic responses. The proposed relationship is shown in Equation 3.8 and the derivations necessary to establish the terms of the  $\mathbf{M}$  matrix will follow.

$$\begin{pmatrix} F_{xx} \\ M_y \\ M_z \\ 0^* \\ 0^* \\ Pr_i \\ T \\ V_{xy} \\ V_{xz} \end{pmatrix} = [\mathbf{M}] \begin{pmatrix} \epsilon_{xx}^0 \\ \kappa_y \\ \kappa_z \\ d\epsilon_{jj}/dz \\ d\epsilon_{jj}/dy \\ \epsilon_D \\ d\phi/dx \\ \gamma_{xy} \\ \gamma_{xz} \end{pmatrix} \quad (3.8)$$



where:

$F_{xx}$  = axial force

$M_y, M_z$  = bending moments about the  $y$  and  $z$  axes, respectively

$Pr_i$  = product of internal pressure and inner radius

$T$  = torsion about the  $x$  axis

$V_{xy}, V_{xz}$  = shear loading in the  $x$ - $y$  and  $x$ - $z$  planes, respectively

and:

$\epsilon_{xx}^0$  = axial strain

$\kappa_y, \kappa_z$  = curvature about the  $y$  and  $z$  axes, respectively

$d\epsilon_{jj}/dz, d\epsilon_{jj}/dy$  = circumferential strain gradient in the  $z$  and  $y$  directions, respectively

$\epsilon_D$  = diametric strain

$d\phi/dx$  = rate of twist about the  $x$  axis

$\gamma_{xy}, \gamma_{xz}$  = shear strain in the  $x$ - $y$  and  $y$ - $z$  planes, respectively

\*Note that the need for zero terms will be clarified in the sections that follow.

## 3.2 Derivation of Stiffness Matrix Terms

Each row of the stiffness matrix  $M$  contains nine terms (some of which are zero) that emerge from an equation relating loading to stress and strain. Each of the equations that are derived in the subsections that follow are based upon the assumption of static equilibrium at a cross section, which is chosen to match the primary stress resulting from the loading.

### 3.2.1 Axial Force

Consider a tube under axial loading; let  $F_{xx}$  denote the total normal force acting upon a cross section that is perpendicular to the center axis of the tube.

An expression can be formed for the force  $dF_{xx}$  acting on the wedge-shaped section shown in Figure 3.2. Beginning with an infinitely thin element within a single lamina, the  $x$  direction force can be found by a simple multiplication of normal stress  $\sigma_{ii}$  and area  $rd\theta dr$  (arc length times thickness). An integration through the thickness of the lamina and a summation across laminae extends calculation to represent  $dF_{xx}$ , the normal force on the wedge-shaped section:

$$dF_{xx} = \sum_{n=1}^N \int_a^b \sigma_{ii}(rd\theta dr) \quad (3.9)$$

where:

$$a = r_n - t_n/2$$

$$b = r_n + t_n/2$$

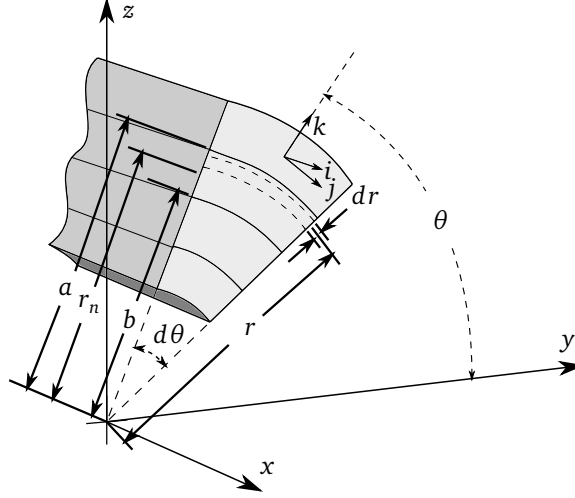


**Figure 3.2:** Depiction of area used in axial, moment, torsion, and shear calculations

The next step is to integrate Equation 3.9 from 0 to  $2\pi$  to find  $F_{xx}$ : the total normal force on the cross section due to axial loading. A substitution of Equation 3.2 for  $\sigma_{i_n}$ , as well as 3.5, 3.6, and 3.7 for strains shows:

$$F_{xx} = \sum_{n=1}^N \int_0^{2\pi} \int_a^b \left[ \bar{Q}_{11_n} (\epsilon_{xx}^0 + \kappa_y r \sin\theta - \kappa_z r \cos\theta) + \bar{Q}_{12_n} \left( r \frac{d\epsilon_{jj}}{dz} \sin\theta + r \frac{d\epsilon_{jj}}{dy} \cos\theta + \epsilon_D \right) \dots \right. \\ \left. + \bar{Q}_{16_n} \left( -r \frac{d\phi}{dx} + \gamma_{xy} \sin\theta - \gamma_{xz} \cos\theta \right) \right] r dr d\theta \quad (3.10)$$

Performing the integration through  $\theta$  has all  $\sin$  or  $\cos$  terms fall to zero:

$$F_{xx} = \sum_{n=1}^N \int_a^b \left[ 2\pi \bar{Q}_{11_n} \epsilon_{xx}^0 + 2\pi \bar{Q}_{12_n} \epsilon_D - 2\pi \bar{Q}_{16_n} r \frac{d\phi}{dx} \right] r dr \quad (3.11)$$

Performing the through-thickness integration produces:

$$F_{xx} = \sum_{n=1}^N 2\pi \left[ \bar{Q}_{11_n} \epsilon_{xx}^0 \left( \frac{b^2 - a^2}{2} \right) + \bar{Q}_{12_n} \epsilon_D \left( \frac{b^2 - a^2}{2} \right) - \bar{Q}_{16_n} \frac{d\phi}{dx} \left( \frac{b^3 - a^3}{3} \right) \right] \quad (3.12)$$

### 3.2.2 Moment

Bending moment produces normal forces in the same plane discussed with axial loading. For this reason the derivation is very similar and uses the same area shown in Figure 3.2. The moment calculation shown in Equation 3.13 differs from what was seen in axial loading in that a moment arm is needed; in the case of  $M_y$  this means the distance from the  $y$  axis, or  $r \sin \theta$ .

$$M_y = \sum_{n=1}^N \int_0^{2\pi} \int_a^b \sigma_{ii}(r \sin \theta) r dr d\theta \quad (3.13)$$

where:

$$a = r_n - t_n/2$$

$$b = r_n + t_n/2$$

Once again Equation 3.2 is substituted for  $\sigma_{ii}$ , followed by 3.5, 3.6, and 3.7 for strains:

$$\begin{aligned} M_y = \sum_{n=1}^N \int_0^{2\pi} \int_a^b & \left[ \bar{Q}_{11n} (\epsilon_{xx}^0 + \kappa_y r \sin \theta - \kappa_z r \cos \theta) + \bar{Q}_{12n} \left( r \frac{d\epsilon_{jj}}{dz} \sin \theta + r \frac{d\epsilon_{jj}}{dy} \cos \theta + \epsilon_D \right) \dots \right. \\ & \left. + \bar{Q}_{16n} \left( -r \frac{d\phi}{dx} + \gamma_{xy} \sin \theta - \gamma_{xz} \cos \theta \right) \right] r^2 \sin \theta dr d\theta \end{aligned}$$

The integration through  $\theta$  eliminates  $\sin \theta$ ,  $\cos \theta$ , or  $\sin \theta \cdot \cos \theta$  terms. Evaluating the through-thickness integration yields:

$$M_y = \sum_{n=1}^N \pi \left[ \bar{Q}_{11n} \kappa_y \left( \frac{b^4 - a^4}{4} \right) + \bar{Q}_{12n} \frac{d\epsilon_{jj}}{dz} \left( \frac{b^4 - a^4}{4} \right) + \bar{Q}_{16n} \gamma_{xy} \left( \frac{b^3 - a^3}{3} \right) \right] \quad (3.14)$$

The derivation for  $M_z$  is analogous and not shown, but yields the following expression:

$$M_z = \sum_{n=1}^N \pi \left[ \bar{Q}_{11n} \kappa_z \left( \frac{b^4 - a^4}{4} \right) - \bar{Q}_{12n} \frac{d\epsilon_{jj}}{dy} \left( \frac{b^4 - a^4}{4} \right) + \bar{Q}_{16n} \gamma_{xz} \left( \frac{b^3 - a^3}{3} \right) \right] \quad (3.15)$$

### 3.2.3 Internal Moment Equilibrium

Two equations are necessary to describe the relationship between the newly defined transverse strain gradients and the loadings on the left side of Equation 3.8. An equilibration of internal moments acting on a longitudinal cross-section (see Figure 3.3) will generate the expressions that yield the necessary  $M$  matrix terms. The internal moments must sum to zero, and hence the loading terms must be zero.

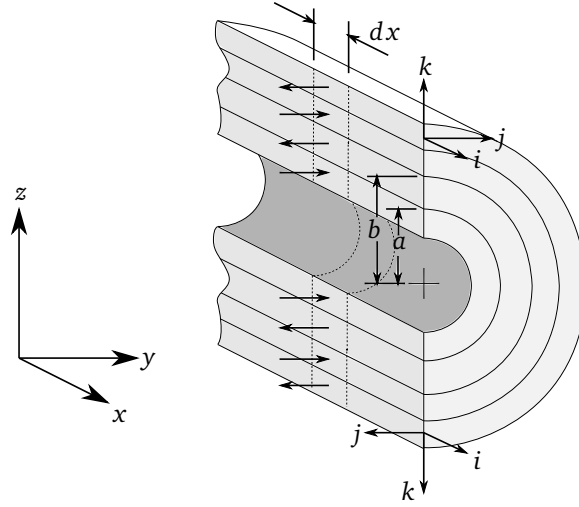


Figure 3.3: Depiction of area used to equilibrate internal moments

In a manner much the same as that seen in the preceding derivations, a summation across laminae of stress multiplied by area – integrated through the thickness – produces an expression for force, which is then multiplied by an elevation to give moment. In this case the area is  $drdx$ , the normal stress is  $\epsilon_{jj}$ , and the elevation from the  $x$  axis is  $r\sin\theta$ . This produces an expression for total internal moment in the element  $dx$ :

$$dM_{int_x k} = \sum_{n=1}^N \int_a^b \sigma_{jj}(drdx)r\sin\theta \quad (3.16)$$

where:

$$a = r_n - t_n/2$$

$$b = r_n + t_n/2$$

Note that no shear force is shown in the equilibration; because it has been assumed that the stress state is independent of  $x$ , any shear force acting in the  $i$ - $j$  plane that might tend to induce a moment about the  $x$  axis will be cancelled out by an equal and opposite force on the adjacent element face.

The  $dx$  term is constant throughout the thickness and can be extracted to the left hand side of the expression, giving an internal moment per unit length:

$$\frac{dM_{int_x}}{dx} = \sum_{n=1}^N \int_a^b \sigma_{jj}r\sin\theta dr \quad (3.17)$$

Because the local  $i$ - $j$ - $k$  coordinate system follows each lamina, a longitudinal cross-section will pass through two separate local coordinate systems. Consequently, Equation 3.17 must be evaluated at two values of  $\theta$ ,  $180^\circ$  apart. The values of  $\theta$  are irrelevant to the result so long as they are in the same plane;

internal moments must sum to zero in any chosen plane. For convenience,  $\theta$  is chosen as  $\pi/2$  and  $3\pi/2$  in this derivation. Substituting Equation 3.3 for  $\sigma_{jj}$  and evaluating at the chosen values of  $\theta$  produces Equation 3.18.

$$\begin{aligned} \frac{dM_{int_x}}{dx} = \sum_{n=1}^N \int_a^b \left[ r \sin\theta \left( \bar{Q}_{21_n} \epsilon_{ii} + \bar{Q}_{22_n} \epsilon_{jj} + \bar{Q}_{26_n} \gamma_{ij} \right) \Big|_{\theta=\pi/2} \dots \right. \\ \left. + r \sin\theta \left( \bar{Q}_{21_n} \epsilon_{ii} + \bar{Q}_{22_n} \epsilon_{jj} + \bar{Q}_{26_n} \gamma_{ij} \right) \Big|_{\theta=3\pi/2} \right] dr \end{aligned} \quad (3.18)$$

Strain equations 3.5, 3.6, and 3.7 are substituted and each case of  $\theta$  is evaluated. This substitution is followed by a number of algebraic steps in which most terms drop out or cancel with one another; the terms that do not are additive and double. The reduced expression is:

$$\frac{dM_{int_x}}{dx} = \sum_{n=1}^N \int_a^b 2 \left[ \bar{Q}_{21_n} \kappa_y r^2 + \bar{Q}_{22_n} \frac{d\epsilon_{jj}}{dz} r^2 + \bar{Q}_{26_n} \gamma_{xy} r \right] dr \quad (3.19)$$

Evaluating the through-thickness integral and enforcing the requirement that internal moment sums to zero brings the result:

$$0 = \sum_{n=1}^N 2 \left[ \bar{Q}_{21_n} \kappa_y \left( \frac{b^3 - a^3}{3} \right) + \bar{Q}_{22_n} \frac{d\epsilon_{jj}}{dz} \left( \frac{b^3 - a^3}{3} \right) + \bar{Q}_{26_n} \gamma_{xy} \left( \frac{b^2 - a^2}{2} \right) \right] \quad (3.20)$$

The derivation of  $dM_{int_x}$  associated with  $\frac{d\epsilon_{jj}}{dy}$  is analogous and not shown, but yields the following expression:

$$0 = \sum_{n=1}^N 2 \left[ -\bar{Q}_{21_n} \kappa_z \left( \frac{b^3 - a^3}{3} \right) + \bar{Q}_{22_n} \frac{d\epsilon_{jj}}{dy} \left( \frac{b^3 - a^3}{3} \right) - \bar{Q}_{26_n} \gamma_{xz} \left( \frac{b^2 - a^2}{2} \right) \right] \quad (3.21)$$

### 3.2.4 Pressure

Consider again a longitudinal cross-section of the tube (refer to Figure 3.4), this time subjected to a pressure-induced force on its inner diameter. Normal stress forms at the face shown to hold the tube together. The stress induced by internal pressure is axisymmetric and as a result it is not necessary to be concerned with cross-section orientation in this derivation. Define  $dF_{jj_n}$  as the total normal force acting on lamina  $n$  in the element with area  $t_n dx$ . Note that a through-thickness derivation is not necessary since lamina elevation does not factor into the following equation.

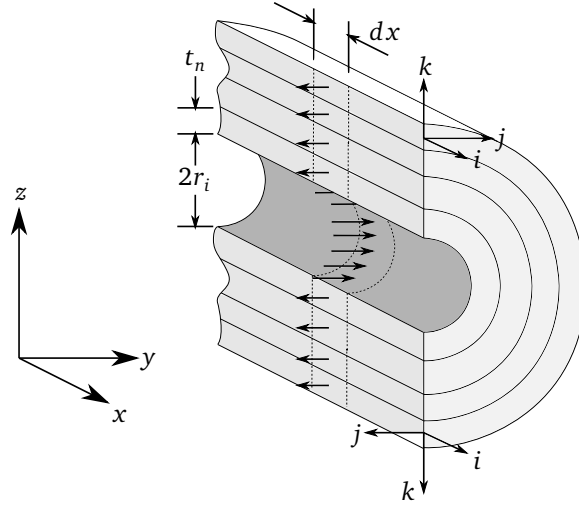


**Figure 3.4:** Depiction of area used in internal pressure calculations (note that only the component of pressure that acts in the  $j$  direction is shown)

$$dF_{jj} = \sum_{n=1}^N \sigma_{jj} t_n dx \quad (3.22)$$

Substituting Equation 3.3 for  $\sigma_{jj}$  and dividing both sides by  $dx$  yields an expression of force per unit length (Equation 3.24). This expression represents only one half (top or bottom laminae in Figure 3.4) of the total force equilibrating the pressure induced force. To enforce static equilibrium, the summation of forces acting on the face shown is set to zero, or rather the force per unit length caused by pressure is equated to twice the force per unit length described in Equation 3.22:

$$2 \frac{dF_{jj}}{dx} = 2r_i P \quad (3.23)$$

where  $2r_i P$  represents the force per unit length caused by pressure, i.e., diameter times pressure. From Equation 3.23 it should be evident how  $\frac{dF_{jj}}{dx} = Pr_i$ .

$$\frac{dF_{jj}}{dx} = \sum_{n=1}^N \left[ \bar{Q}_{21n} \epsilon_{xx}^0 + \bar{Q}_{22n} \epsilon_D - \bar{Q}_{26n} r \frac{d\phi}{dx} \right] t_n = Pr_i \quad (3.24)$$

### 3.2.5 Torsion

In developing an expression for torsion, one may refer back to Figure 3.2, and consider the shear loading  $\tau_{ij}$  imposed on an infinitesimal element within a lamina. The torque contribution of this element is expressed as the product of stress, area, and moment arm (radius). Integrating through the thickness

gives the torque contribution of lamina  $n$ :

$$dT_n = \int_a^b -\tau_{ij}(rd\theta dr)r \quad (3.25)$$

A summation across laminae and an integration through  $\theta$  gives total torque:

$$T = \sum_{n=1}^N \int_0^{2\pi} \int_a^b -\tau_{ij}(rd\theta dr)r \quad (3.26)$$

Substitution of Equation 3.4 for  $\tau_{ij}$  followed by 3.5, 3.6, and 3.7 for strains gives:

$$\begin{aligned} T = & - \sum_{n=1}^N \int_0^{2\pi} \int_a^b \left[ \bar{Q}_{61_n} (\epsilon_{xx}^0 + \kappa_y r \sin\theta - \kappa_z r \cos\theta) + \bar{Q}_{62_n} \left( r \frac{d\epsilon_{jj}}{dz} \sin\theta + r \frac{d\epsilon_{jj}}{dy} \cos\theta + \epsilon_D \right) \dots \right. \\ & \left. + \bar{Q}_{66_n} \left( -r \frac{d\phi}{dx} + \gamma_{xy} \sin\theta - \gamma_{xz} \cos\theta \right) \right] r^2 dr d\theta \quad (3.27) \end{aligned}$$

Finally, an evaluation of the integrals presents the expression for torque:

$$T = \sum_{n=1}^N 2\pi \left[ -\bar{Q}_{61_n} \epsilon_{xx}^0 \left( \frac{b^3 - a^3}{3} \right) - \bar{Q}_{62_n} \epsilon_D \left( \frac{b^3 - a^3}{3} \right) + \bar{Q}_{66_n} \frac{d\phi}{dx} \left( \frac{b^4 - a^4}{4} \right) \right] \quad (3.28)$$

### 3.2.6 Shear

Forming an expression for shear force requires a slightly more involved approach than has been seen in the preceding derivations; a transverse shear loading in the global coordinate system results in a lamina shear stress which varies direction in the local coordinate system, depending on location  $\theta$  in the plane of interest. It is necessary to employ stress and strain transformation theories to quantify the effect of global shear loading on a particular lamina.

In the local coordinate system, forming an expression for shear force is simple; consider again the infinitesimal element in Figure 3.2 under shear loading. The shear force acting on the element may be expressed as the product of stress and area:

$$\begin{aligned} dV_{ij_n} &= \tau_{ij_n} r dr d\theta \\ dV_{ik_n} &= \tau_{ik_n} r dr d\theta \end{aligned} \quad (3.29)$$

where  $dV_{ij_n}$  and  $dV_{ik_n}$  are the shear forces acting on an infinitesimal element in lamina  $n$ , and  $\tau_{ij_n}$   $\tau_{ik_n}$  the shear stresses. Needless to say, these shears are not in the global coordinate system and, therefore, must be converted before carrying forward with the development of an expression for global shear loading.

It is possible to arrive at an expression for shear loading in the global coordinate system by treating

the loadings as vectors and applying some simple trigonometry to convert between coordinate systems:

$$\begin{aligned} dV_{xy_n} &= dV_{ij_n} \sin\theta + dV_{ik_n} \cos\theta \\ dV_{xz_n} &= dV_{ik_n} \sin\theta - dV_{ij_n} \cos\theta \end{aligned} \quad (3.30)$$

Substituting Equations 3.29 into 3.30 produces the desired expressions of global shear force as a function of local shear stress:

$$\begin{aligned} dV_{xy_n} &= \tau_{ij_n} \sin\theta r dr d\theta + \tau_{ik_n} \cos\theta r dr d\theta \\ dV_{xz_n} &= \tau_{ik_n} \sin\theta r dr d\theta - \tau_{ij_n} \cos\theta r dr d\theta \end{aligned} \quad (3.31)$$

Just as with the preceding derivations, the next step is to substitute expressions for stresses, in this case  $\tau_{ij}$  and  $\tau_{ik}$ . While Equation 3.4 can be used for  $\tau_{ij}$ , the stress  $\tau_{ik}$  has not yet been defined. If it is assumed that there is no coupling associated with the  $i$ - $k$  plane one may simply use the relation  $\tau_{ik_n} = G_{ik} \gamma_{ik}$ . Substituting Equation 3.4 for  $\tau_{ij}$  and the newly defined expression for  $\tau_{ik}$  into Equations 3.31 gives:

$$\begin{aligned} dV_{xy_n} &= \left[ (\bar{Q}_{61_n} \epsilon_{ii_n} + \bar{Q}_{62_n} \epsilon_{jj_n} + \bar{Q}_{66_n} \gamma_{ij_n}) \sin\theta + (G_{ik_n} \gamma_{ik_n}) \cos\theta \right] r dr d\theta \\ dV_{xz_n} &= \left[ (G_{ik_n} \gamma_{ik_n}) \sin\theta - (\bar{Q}_{61_n} \epsilon_{ii_n} + \bar{Q}_{62_n} \epsilon_{jj_n} + \bar{Q}_{66_n} \gamma_{ij_n}) \cos\theta \right] r dr d\theta \end{aligned} \quad (3.32)$$

The next step is to substitute in equations for the strains; it should be noticed first that expressions are needed for  $G_{ik}$  and  $\gamma_{ik}$ . An expression for  $G_{ik}$  can be derived in a procedure involving vector addition of strains and a ‘wedge-method’ equilibration of stresses. Alternatively, the expression is found in [35] as:

$$G_{ik} = G_{13} \cos^2(f_a) + G_{23} \sin^2(f_a) \quad (3.33)$$

where  $f_a$  is the fibre angle,  $G_{23}$  is found from Equation 2.1, and transverse isotropy requires that  $G_{13} = Q_{66}$  [9]. The same strain transformation procedure that produced the relation for  $\gamma_{ij}$  (Equation 3.7) caused by shear can be applied to show that  $\gamma_{ik_{shear}} = \gamma_{xy} \cos\theta + \gamma_{xz} \sin\theta$ . Recalling the assumption that no coupling exists that can induce the shear  $\gamma_{ik}$ , one may write:

$$\gamma_{ik} = \gamma_{xy} \cos\theta + \gamma_{xz} \sin\theta \quad (3.34)$$

The variables  $\epsilon_{ii}$ ,  $\epsilon_{jj}$ ,  $\gamma_{ij}$ ,  $G_{ik}$ , and  $\gamma_{ik}$  in the expression for  $dV_{xy_n}$  of Equations 3.32 are replaced by inserting equations 3.5, 3.6, 3.7, 3.33, and 3.34, respectively. A double integration and summation takes



the infinitesimal element force  $dV_{xy_n}$  to the total shear force in the  $x$ - $y$  direction  $V_{xy}$ :

$$V_{xy} = \sum_{n=1}^N \int_0^{2\pi} \int_a^b \left[ \left( \bar{Q}_{61_n} \epsilon_{xx}^0 + \bar{Q}_{61_n} \kappa_y r \sin\theta - \bar{Q}_{61_n} \kappa_z r \cos\theta + \bar{Q}_{62_n} \epsilon_D + \bar{Q}_{62_n} \frac{d\epsilon_{jj}}{dz} r \sin\theta + \bar{Q}_{62_n} \frac{d\epsilon_{jj}}{dy} r \cos\theta \dots \right. \right. \\ \left. \left. - \bar{Q}_{66_n} r \frac{d\phi}{dx} + \bar{Q}_{66_n} (\gamma_{xy} \sin\theta - \gamma_{xz} \cos\theta) \right) \sin\theta + G_{ik} (\gamma_{xy} \cos\theta + \gamma_{xz} \sin\theta) \right] r dr d\theta \quad (3.35)$$

Carrying out the integrations gives:

$$V_{xy} = \sum_{n=1}^N \pi \left[ \left( \frac{b^3 - a^3}{3} \right) \left( \bar{Q}_{61} \kappa_y + \bar{Q}_{62} \frac{d\epsilon_{jj}}{dz} \right) + \left( \frac{b^2 - a^2}{2} \right) (\gamma_{xy}) (\bar{Q}_{66} + G_{ik}) \right] \quad (3.36)$$

A similar procedure will take the  $dV_{xz_n}$  term of Equations 3.32 to an expression for the total shear force in the  $x$ - $z$  direction  $V_{xz}$ :

$$V_{xz} = \sum_{n=1}^N \pi \left[ \left( \frac{b^3 - a^3}{3} \right) \left( \bar{Q}_{61} \kappa_z - \bar{Q}_{62} \frac{d\epsilon_{jj}}{dy} \right) + \left( \frac{b^2 - a^2}{2} \right) (\gamma_{xz}) (\bar{Q}_{66} + G_{ik}) \right] \quad (3.37)$$

### 3.3 Result: Relationship Between Loading and Elastic Response

Each of the preceding expressions corresponds to an entry in the loading matrix and contains three terms; each term being a multiple of an entry in the elastic response matrix. Arranging all of these derived expressions into matrix form produces the relationship between loadings and elastic responses:

$$\begin{pmatrix} F_{xx} \\ M_y \\ M_z \\ 0 \\ 0 \\ Pr_i \\ T \\ V_{xy} \\ V_{xz} \end{pmatrix} = \begin{bmatrix} M_{11} & 0 & 0 & 0 & 0 & M_{16} & M_{17} & 0 & 0 \\ 0 & M_{22} & 0 & M_{24} & 0 & 0 & 0 & M_{28} & 0 \\ 0 & 0 & M_{33} & 0 & M_{35} & 0 & 0 & 0 & M_{39} \\ 0 & M_{42} & 0 & M_{44} & 0 & 0 & 0 & M_{48} & 0 \\ 0 & 0 & M_{53} & 0 & M_{55} & 0 & 0 & 0 & M_{59} \\ M_{61} & 0 & 0 & 0 & 0 & M_{66} & M_{67} & 0 & 0 \\ M_{71} & 0 & 0 & 0 & 0 & M_{76} & M_{77} & 0 & 0 \\ 0 & M_{82} & 0 & M_{84} & 0 & 0 & 0 & M_{88} & 0 \\ 0 & 0 & M_{93} & 0 & M_{95} & 0 & 0 & 0 & M_{99} \end{bmatrix} \begin{pmatrix} \epsilon_{xx}^0 \\ \kappa_y \\ \kappa_z \\ d\epsilon_{jj}/dz \\ d\epsilon_{jj}/dy \\ \epsilon_D \\ d\phi/dx \\ \gamma_{xy} \\ \gamma_{xz} \end{pmatrix} \quad (3.38)$$

where

$$\begin{aligned}
M_{11} &= \sum_{n=1}^N 2\pi \bar{Q}_{11_n} \psi_2 ; & M_{16} &= \sum_{n=1}^N 2\pi \bar{Q}_{12_n} \psi_2 ; & M_{17} &= \sum_{n=1}^N -2\pi \bar{Q}_{16_n} \psi_3 ; \\
M_{22} = M_{33} &= \sum_{n=1}^N \pi \bar{Q}_{11_n} \psi_4 ; & M_{24} = -M_{35} &= \sum_{n=1}^N \pi \bar{Q}_{12_n} \psi_4 ; & M_{28} = M_{39} &= \sum_{n=1}^N \pi \bar{Q}_{16_n} \psi_3 ; \\
M_{42} = -M_{53} &= \sum_{n=1}^N -2\bar{Q}_{21_n} \psi_3 ; & M_{44} = M_{55} &= \sum_{n=1}^N 2\bar{Q}_{22_n} \psi_3 ; & M_{48} = -M_{59} &= \sum_{n=1}^N -2\bar{Q}_{26_n} \psi_2 ; \\
M_{61} &= \sum_{n=1}^N \bar{Q}_{21_n} \psi_1 ; & M_{66} &= \sum_{n=1}^N \bar{Q}_{22_n} \psi_1 ; & M_{67} &= \sum_{n=1}^N -\bar{Q}_{26_n} \psi_2 ; \\
M_{71} &= \sum_{n=1}^N -2\pi \bar{Q}_{61_n} \psi_3 ; & M_{76} &= \sum_{n=1}^N -2\pi \bar{Q}_{62_n} \psi_3 ; & M_{77} &= \sum_{n=1}^N 2\pi \bar{Q}_{66_n} \psi_4 ; \\
M_{82} = M_{93} &= \sum_{n=1}^N \pi \bar{Q}_{61_n} \psi_3 ; & M_{84} = -M_{95} &= \sum_{n=1}^N \pi \bar{Q}_{62_n} \psi_3 ; & M_{88} = M_{99} &= \sum_{n=1}^N \pi (\bar{Q}_{66_n} + G_{i_{k_n}}) \psi_2 ;
\end{aligned}$$

and,

$$\psi_1 = (b - a) ; \quad \psi_2 = \left( \frac{b^2 - a^2}{2} \right) ; \quad \psi_3 = \left( \frac{b^3 - a^3}{3} \right) ; \quad \psi_4 = \left( \frac{b^4 - a^4}{4} \right)$$

The relationship described by Equation 3.38 is most useful when rearranged to form an expression for elastic responses as a function of loading:

$$\left\{ \begin{array}{c} \epsilon_{xx}^0 \\ \kappa_y \\ \kappa_z \\ d\epsilon_{jj}/dz \\ d\epsilon_{jj}/dy \\ \epsilon_D \\ d\phi/dx \\ \gamma_{xy} \\ \gamma_{xz} \end{array} \right\} = [\mathbf{M}^{-1}] \left\{ \begin{array}{c} F_{xx} \\ M_y \\ M_z \\ 0 \\ 0 \\ Pr_i \\ T \\ V_{xy} \\ V_{xz} \end{array} \right\} \quad (3.39)$$

This relationship is not easily solved by hand as it involves the inversion of a nine by nine matrix. A code has been developed in the MATLAB<sup>®</sup> computing environment that allows for a fast and efficient solution (see Appendix C). Computing time is on the order of 0.25 seconds<sup>1</sup>. The user is required to generate a spreadsheet that describes the FRP layup, as well as one that describes the cross-section geometry and loading conditions. The program accesses these spreadsheets and generates a  $\bar{\mathbf{Q}}$  matrix corresponding to each layer, then populates the  $\mathbf{M}$  matrix. Once the  $\mathbf{M}$  matrix has been generated, the elastic response may be obtained through solution of Equation 3.39. It is possible that this system of equations could be reorganized to form a banded stiffness matrix; however, the increase in calculation efficiency would not warrant the effort, as computational runtimes are already very low.

<sup>1</sup>Analyses were performed on a PC running Microsoft<sup>®</sup> Windows<sup>®</sup> 7 Professional (64 bit) with an Intel<sup>®</sup> Core<sup>™</sup> i7-2600k CPU @ 3.40 GHz. The PC was equipped with 16 GB of RAM.

## 3.4 Discussion

A number of assumptions were made in the preceding derivations; they are discussed with regard to their implications and potential effects on model accuracy, as follows:

### 3.4.1 Bending

The bending model employed here is one of Euler-Bernoulli beam theory; axial-direction normal strains resulting from bending are assumed to vary linearly with distance from the neutral axis. Euler-Bernoulli beam theory does not consider the transverse shear strain caused by a bending moment that varies through the beam's length. Consequently, the model loses integrity as the beam's length-to-diameter ratio decreases, particularly in the case of a beam having a thin outer layer with significantly higher moduli than the inner layer or layers. These problems are not unexpected; classical Euler-Bernoulli treatment of beam bending is known to over-predict bending stiffness in low aspect-ratio beams and especially in sandwich-panel beams having a low aspect-ratio. The use of an expression for bending moment that is based on Timoshenko beam theory would account for this shortcoming of the current model, but was not included due to the unwarranted complexity. The typical use case of the expressions will be long slender members where the error will be small.

### 3.4.2 Transverse Strain Gradients

A set of 'strain gradients' was defined with the purpose of capturing the lamina strain  $\epsilon_{jj}$ , which varies linearly with elevation from the neutral axis. To clarify: a curvature  $\kappa_y$  results in a strain  $\epsilon_{jj}$  that varies linearly with elevation from the  $y$  axis; the rate of variance is characterized by  $\frac{d\epsilon_{jj}}{dz}$ . Likewise, curvature  $\kappa_z$  results in a strain  $\epsilon_{jj}$  varying linearly with elevation from the  $z$  axis, characterized by  $\frac{d\epsilon_{jj}}{dy}$ . It was mentioned that these strain gradients do not have a direct significance, but are necessary to quantify the non-uniform transverse strain in the tube. It is therefore unlikely that these values will be pertinent to design, but the terms that emerge from the preceding derivations capture an important characteristic of transverse strain within the tube.

### 3.4.3 Pressure

The expression for pressure developed and used in the current model is based upon plane-stress assumptions for *thin-walled* tubes. A derivation could be produced and included that accounts for the non-uniform distribution of normal stress  $\sigma_{jj}$  present when a *thick-walled* tube is subjected to a pressure loading. However, this has not been done; the primary intent of the current model is accurate prediction of the elastic response to common structural loadings (i.e., axial force, bending moment, torsion, and transverse shear). While certain cases of these loadings may cause  $\sigma_{jj}$  stress, the distribution thereof

is not critical to the overall stiffness characteristics of the tube. The inclusion of a pressure term in the model serves to allow quantification of uniform diametric strain. This strain is present in the pure axial and torsional loading of tubes and cylinders as a result of Poisson's ratio effects; the effect of this strain (in loadings other than pressure) depends on the  $M_{16}$ , and  $M_{76}$  terms of the  $\mathbf{M}$  matrix, for axial loading and torsional loading, respectively. Without the pressure expression included in the model, the effect of these terms would not be included.

All of the terms that appear in the loading matrix on the left hand side of Equation 3.8 are simply loads, except the pressure term  $Pr_i$ , which includes a geometric parameter (inner radius). An effort to maintain consistency would see the equation re-arranged to have the pressure load  $P$  alone on one side of the equals sign. However, this model is developed with the potential to analyse the response of not only tubes, but also solid cylinders where  $r_i = 0$ . Expressing Equation 3.24 with  $P$  alone on one side of the equation would result in an  $r_i$  denominator term; moving a potentially null variable into position as a denominator opens the door for problems with computer coding, which is the ultimate destination of these derivations. For this reason the term remains as  $Pr_i$ .

#### 3.4.4 Transverse Shear

In the derivation of an expression for shear, it was assumed that no coupling associated with the  $i$ - $k$  plane exists. This assumption allows the through-thickness transverse shear stress  $\tau_{ik}$  to be described by the relation  $\tau_{ik} = G_{ik}\gamma_{ik}$ . This assumption of no coupling in the  $i$ - $k$  plane is backed by two realizations:

1. Recall the study of the stress-strain response of a single lamina, seen in Section 2.2.5 where the fibre direction is labelled as the one direction, and the in-plane, and through-thickness directions are labelled two and three, respectively. Rotation of the one-two-three coordinate system such that the fibre axis does not coincide with a primary axis, but remains within the plane of the lamina, is then labelled  $x$ - $y$ - $z$ . A transformation of the compliance matrix of Equation 2.13 to represent an  $x$ - $y$ - $z$  coordinate system will show that the through-thickness shear strain  $\gamma_{xz}$  is a function of only the out-of-plane shear stress  $\tau_{yz}$ , and the through-thickness shear stress  $\tau_{xz}$ . Inverting this relationship will show the through-thickness shear stress  $\tau_{xz}$  to be a function of only the out-of-plane shear strain  $\gamma_{yz}$ , and the through-thickness shear strain  $\gamma_{xz}$ . Relating this to the current case with an  $i$ - $j$ - $k$  coordinate system reveals that the through-thickness shear stress  $\tau_{ik}$  is a function of only the out-of-plane shear strain  $\gamma_{jk}$ , and the through-thickness shear strain  $\gamma_{ik}$ . Furthermore, the coupling term associated with the out-of-plane shear strain  $\gamma_{jk}$  is zero for any lamina where the two out-of-plane shear moduli are equal ( $G_{jk} = G_{ik}$ ); while this is typically not true, their magnitudes are generally very close, resulting in a negligible coupling term.
2. Regardless of the size of the compliance term associated with the out-of-plane shear strain  $\gamma_{jk}$ , the cylinder subjected to any loading under the current investigation will not experience a significant

$\gamma_{jk}$  shear deformation, and so the effect of any coupling is further diminished.

The current treatment of a transversely applied shear loading harbours another assumption; no consideration has been given to the attenuation of transverse shear toward the free edges of the cross section. It is known that a free surface can not bear a *through-thickness* shear stress; in the case of a tube with circular cross-section, the free surfaces exist at the inner and outer diameter of the tube. Strictly speaking, the only free surfaces that truly do not exhibit shear stress with response to the applied shear loading are those that are perpendicular to the applied shear loading, i.e., infinitesimally small tangent extremities of the cross-section. Recall the well known shear stress distribution for a thin-walled tube and a solid rod (both of isotropic material) found in any good mechanics of materials text (reproduced for convenience in Figure 3.5). For a shear force in the  $y$  direction, zero shear stress surfaces exist on the  $y$  axis, at  $\pm r_i$  and  $\pm r_o$ . While the average value of transverse shear stress in the model will match the reality, the assumed through-thickness distribution of transverse shear is inaccurate – a result of ignoring the free surfaces' inability to carry shear stress. In reality, the through-thickness shear stress distribution will diminish near to the inner and outer diameters in a non-linear manner.

The stress distribution seen in Figure 3.5 is not necessarily representative of a composite tube; it is likely that anisotropy and coupling effects may augment, slightly, the non-linearity of the shear stress distribution. However, the distribution shown provides some insight into the potential for erroneous predictions of maximum shear stress; the shear stress is significantly higher at the location of  $\tau_{max}$  than the average used in the current model. This would become gravely important if the current model was adapted to include failure prediction; shear failure is a common mode in FRP laminates due to the relatively low shear strength and modulus. For current purpose of the model though, shear stiffness is the relevant parameter, and while the model's failure to account for shear stress distribution gives erroneous peak shear stress values, the average should remain accurate, given that the laminae are transversely isotropic. Consequently, transverse shear stiffness is modelled with sufficient accuracy.

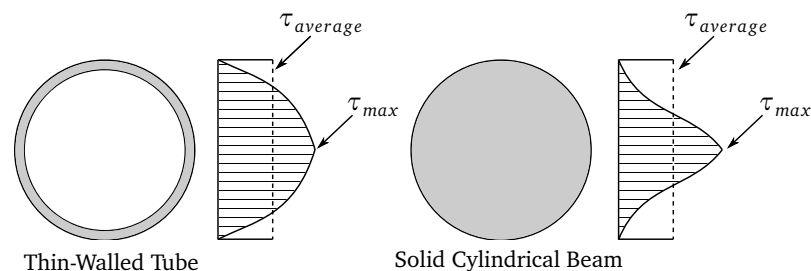


**Figure 3.5:** Distribution of shear stress in circular cross-sections with response to transverse shear loading (of an isotropic material)

### 3.4.5 Additional Stress and Strain Distribution Considerations

The current model assumes that end-effects are negligible, i.e., the application of loading is far enough away from the area of interest that end effects become irrelevant. The effects of end constraints, shear lag, etc., are well beyond the scope of the model presented.

It was shown in [25] that a uniform stress field generally does not result from axial loading, even far from the area of load application; the mechanics, however, are not well explained. Consider the cross section of a thick-walled tube of  $+45^\circ$  FRP subjected to uniform axial tension. Uniform axial strain is assumed; as a result, the tendency of any point through the thickness of the tube is to strain transversely, *by an equal amount* (extensional shear lamina coupling). Because the lamina is tubular and seamless, the global result is extensional-torsional coupling. The tube's induced torsional deflection results in a transverse strain that varies with radius, through the thickness of the tube – each point is forced to strain by an *unequal* amount. In comparing the global effect of each point's tendency to transversely strain, the inner points would cause more torsional deflection for a given transverse strain than the outer; this is clear upon examination of the geometric relation  $\gamma_{transverse} = r\phi$ , or clearer yet when the relation is expressed as  $\phi = \gamma_{transverse}/r$ . What this means is that in reality, where transverse strain distribution is a function of  $r$ , the material on the outside is strained more than its natural tendency, and the material on the inside is strained less. The differential between imposed shear strain and the natural lamina shear strain response generates variation in the normal stress distribution through the thickness of the tube. The current model accounts for this phenomenon precisely as it was described here. It would be valuable to perform an investigation using the current model, on the the distribution of normal stress through the thickness of a thick-walled tube, and compare the result to existing predictions of [25]. This study has not been performed here due to time constraints, but would be easily done using the computer code developed for the model presented.

It is also worth nothing that an effect somewhat analogous to that described in the preceding paragraph exists when the tube is subjected to uniform transverse shear loading; transverse shear stress develops throughout the thickness, but more so in laminae that have their tendency to exhibit shear-extensional coupling suppressed by surrounding laminae. Consider, for example, a tube comprising three layers, configured as (from the inside out) a unidirectional  $0^\circ$  lamina, a  $+45^\circ$  lamina, and another unidirectional  $0^\circ$  lamina, loaded in uniform transverse shear. The  $+45^\circ$  lamina will adopt more shear stress as a result of having a higher transverse shear modulus, but the effect is augmented by the fact that the unidirectional laminae are very stiff in extension and are bonded to the middle lamina, restraining its extension (through inter-laminar shear). This increase in shear stress, however, is local to the section of laminae that is parallel to the direction of transverse shear loading; as the laminae approach a perpendicular orientation, the effect is no longer present (this is the cause of global shear-bending coupling). Consequently, not only can the transverse shear stress distribution vary between laminae, but also through location  $\theta$  in a lamina, and as discussed, with proximity to a free surface. While it was

mentioned that no provisions have been made for attenuation of transverse shear stress near the free surface, no constraints are imposed by the model on the transverse shear stress distribution – it is allowed to develop the distribution discussed. The author has not encountered any study in the literature of this distribution, but one could be performed using the presented model.

### **3.4.6 Through-Thickness Normal Stress**

Lastly, it is necessary to discuss through-thickness normal stress. The model presented here makes no attempt at accounting for through-thickness normal stress. Aside from pressure loading of thick-walled tubes, none of the applied loadings included in the model directly produce a through-thickness normal stress. It is possible that a differential, between lamina, of diametric expansion would subject certain laminae to through-thickness normal stress, but the effect is likely minuscule. Discussion has been presented already with regard to shortcomings of the model's treatment of pressure; through thickness normal stress falls into the same category and could be added to the model if desired.

## Chapter 4

# Validation of The Elasticity Model

Validation of the elasticity model is sought through computational and experimental means. The following sections detail the efforts, results, and shortcomings of both methodologies. The first section focuses on computational validation and provides a thorough analysis of a select few cases, comparing between finite element predictions and laminated cylinder model predictions of elastic tube response. Lastly, some final remarks are provided with regard to missing aspects of validation. The second section will provide details and information regarding the specimens subjected to physical testing, the apparatus used therein, and the experiments themselves: three point flexure tests, as well as torsion tests. A discussion is provided, outlining the implications of the experiments.

### 4.1 Finite Element Analysis

Two finite element (FE) studies were performed, with each study containing numerous FE models. The first study compares the response of a thin-walled tube in torsion as modelled using 1) shell elements in FE, and 2) the laminated cylinder model. The second study examines the effect tube thickness has on the FE and laminated cylinder model prediction of axial force response as well as extensional-torsional coupling. The FE models were meshed and preprocessed using Altair<sup>®</sup> Hypermesh<sup>®</sup>, and solved using the linear static solver of RADIOSS<sup>®</sup>.

#### 4.1.1 Elastic Response to Torsion of a Thin-Walled Tube

A tube of 20 mm length, 2 mm diameter, and 0.1 mm wall-thickness was modelled using both the FE method, and the laminated cylinder model; the tube's torsional deformation (angular deflection  $\phi$ ) in response to an applied torsional loading of 1 N-mm is predicted. The solutions of the FE method and the laminated cylinder model are compared and discussed. A mesh sensitivity study is included to ensure convergence of the FE solution.



### Finite Element Model Architecture

An FE model was generated with CQUAD4 quadrilateral shell elements approximating the tube; elements were meshed with a 0.5 mm nominal-size. A linear-elastic orthotropic material model was used with the properties shown in Table 4.1 and the fibre-angle was specified as  $45^\circ$ .

**Table 4.1:** In-plane properties of unidirectional carbon-fibre/epoxy laminate used in FE studies ( $V_f = 0.6$ )

Material	$E_{11}$ (GPa)	$E_{22}$ (GPa)	$\nu_{12}$	$G_{12}$ (GPa)	Ref.
AS4(Carbon)/3501-6(Epoxy)	131.0	11.2	0.28	6.55	[36]

The nodes at one end of the model are all constrained in translational movement in the axial ( $x$ ) direction using single-point constraints (SPCs). The tube is restrained from rotation by special treatment of the top-most, bottom-most, left-most, and right-most nodes; the top and bottom nodes, which coincide with the vertical ( $z$ ) axis, have their translation in the horizontal ( $y$ ) direction constrained as well. The left and right nodes, which coincide with the  $y$  axis, are also restricted from translation in  $z$ . This treatment allows the end of the tube to expand, while prohibiting translation or rotation. These constraints may be seen in Figure 4.1a.

On the nodes at the opposing end of the model, a torsion is imposed through an interpolation (RBE3) element. The central node of this element has a moment applied and evenly distributes tangential forces to each node at one end of the model – simulating torsional loading. This configuration may be seen in Figure 4.1b.

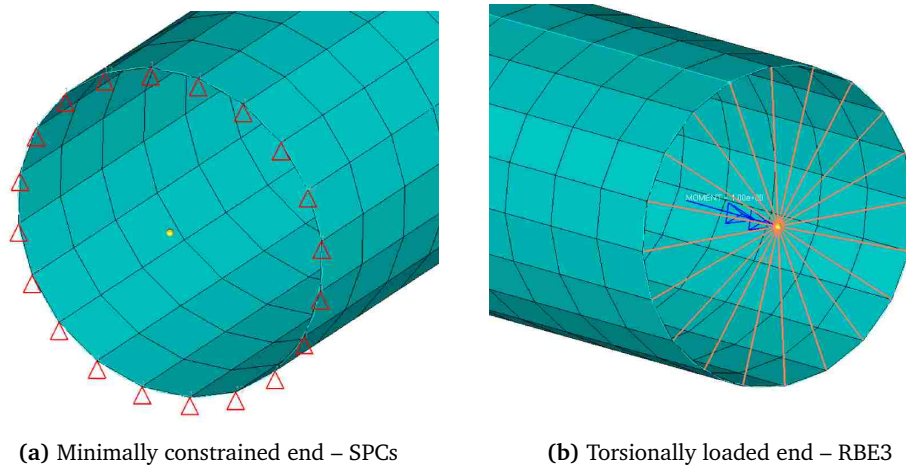


**Figure 4.1:** FE torsion model: constraints and loading (0.5 mm mesh shown)

## Results

Three FE models were generated using the following mesh sizes: 1.0 mm, 0.5 mm, and 0.25 mm. The torsional deflection prediction that results from each mesh size is shown in Table 4.2. Beyond a 0.5 mm mesh, no significant change is seen in the solution.

**Table 4.2:** Mesh sensitivity study of torsionally loaded FE model

Mesh Size (mm)	$\phi_{FE}$ (degrees)
1.0	0.2221
0.5	0.1958
0.25	0.1958

The laminated cylinder model predicts an angular displacement of  $0.1835^\circ$  in the tube. Comparing the FE method solution to that of the laminated cylinder model produces a 6.7% difference.

## Discussion

The solution of the FE model and the laminated cylinder model do not converge to the extent that one might expect when dealing with a thin-walled tube; the tube diameter to wall-thickness ratio is 20, which should be sufficiently high to warrant the use of shells in the FE model. Moreover, the tube diameter to wall-thickness ratio should be high enough to warrant use of CLPT to obtain a shear modulus for the material and proceed with classical torsional deformation calculations using  $\phi = TL/JG$ . Doing this produces an angular displacement prediction of  $0.1841^\circ$  for the tube under consideration. This is within 0.3% of the laminated cylinder model's prediction. Given the tube diameter to wall-thickness ratio, and the comparability of the classical and laminated cylinder model prediction, it is likely that the FE model is not producing a fully accurate solution; further investigation with a non-linear FE solver or a solid element model could provide a great deal of insight as to why, but is not performed here due to limitations in time and resources.

### 4.1.2 The Effect of Tube Wall-Thickness on Axial Response & Coupling

Five tubes of varying wall-thickness with a length of 20 mm and a diameter of 2 mm were modelled using FE methods and the laminated cylinder model. The tubes were subjected to an axial tensile force of 100 N and the axial strain response (change in length  $dl$ ) and torsional coupling response (angular displacement  $\phi$ ) were predicted using both methods; the results were then compared over the range of tube wall-thickness. In all cases, the tube was modelled to contain a single lamina of unidirectional carbon-fibre/epoxy at a  $45^\circ$  helix angle. The material properties of the lamina are shown in Table 4.1.

### Finite Element Model Architecture

An FE model was generated with quadrilateral shell elements approximating the tube; elements were meshed with a 0.5 mm nominal-size. A linear-elastic orthotropic material model was used with the properties shown in Table 4.1 and the fibre-angle was specified at  $45^\circ$ .

The nodes at one end of the model are constrained using SPCs in the same manner that was discussed in Section 4.1.1. The opposing end of the model has its nodes subjected to a tensile force in the axial direction. Both the constraints (SPCs) and the loading may be seen in Figure 4.2.

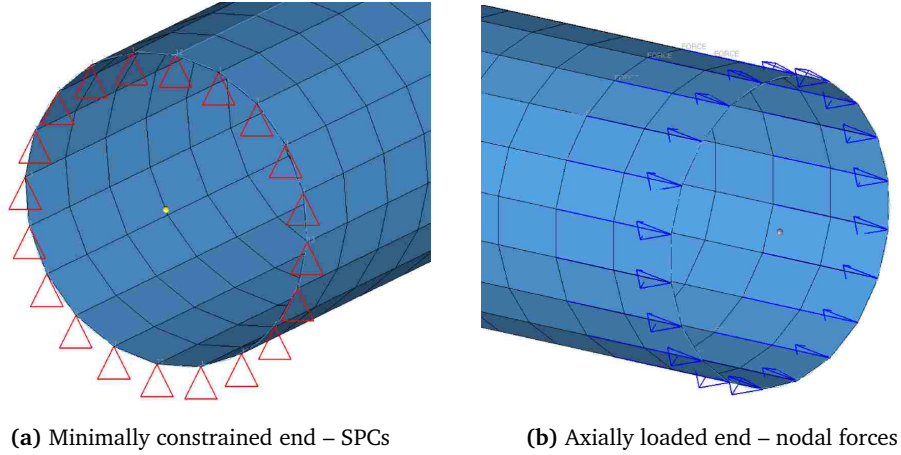


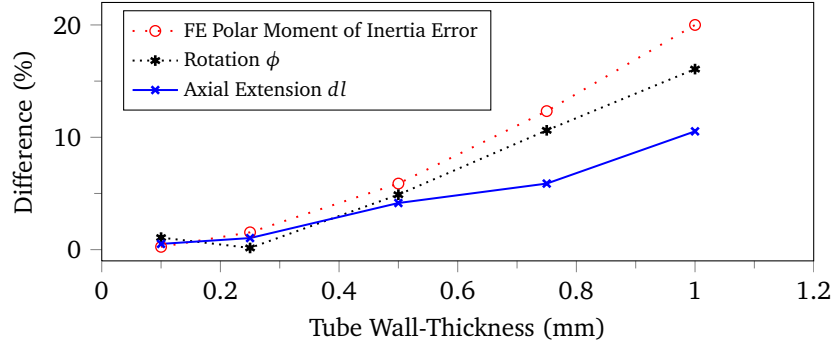
Figure 4.2: FE axial loading model: constraints and loading

### Results

The axial response predictions (shown as extension  $dl$ ) as well as predictions of the resulting torsional deformation (shown as  $\phi$ ) are shown in Table 4.3 for each tube wall-thickness investigated. The difference between the two predictions is seen in the aforementioned table, or more clearly (as an absolute value) plotted in Figure 4.3. Also present on the plot is the percent difference between two values for polar moment of inertia: one obtained using the classical formula  $J_{classical} = \frac{\pi(r_o^4 - r_i^4)}{2}$  for tubes, as well as the moment of inertia that results from a shell calculation  $J_{shell} = 2\pi t r^3$ , where  $t$  is the tube wall-thickness. The latter of these formulae is likely unfamiliar to the reader, but may be easily derived from the definition of a cross-section's polar moment of inertia  $J = \int_A \rho^2 dA$ , where  $\rho$  is the distance from the axis of interest to the centroid of area  $dA$ . In the case of a tube modelled as a shell, the distance  $\rho$  is constant, and the total area may be given by  $2\pi r t$ . The relevance of this line on the plot is clarified in the section that follows.

**Table 4.3:** Axially loaded model results: axial force response  $dl$  & associated extensional-torsional coupling  $\phi$  for a number of tubes with varying wall-thickness

Thickness (mm)	$dl_{model}$ (mm)	$dl_{FE}$ (mm)	Difference (%)	$\phi_{model}$ (degrees)	$\phi_{FE}$ (degrees)	Difference (%)
0.10	0.195	0.196	0.51	7.411	7.490	1.07
0.25	0.078	0.077	-1.03	2.893	2.889	-0.15
0.50	0.039	0.037	-4.15	1.335	1.270	-4.89
0.75	0.026	0.024	-5.88	0.793	0.709	-10.62
1.00	0.019	0.017	-10.53	0.521	0.437	-16.07

**Figure 4.3:** Percent difference (absolute value) in predictions of FE and laminated cylinder model on axial response and axial-torsional coupling. The percent difference between the polar moment of inertia calculated using classical methods and that of shell assumptions is also shown.

## Discussion

A distinct divergence of the FE and laminated cylinder model prediction for axial strain response to tensile loading is evident in Table 4.3. The magnitude of said divergence is depicted by the plot of the percent difference between  $dl$  predictions in Figure 4.3 (solid-line). For a thin-walled tube, the prediction of the two models is quite similar; however, as tube thickness increases, there is a development of the non-uniform normal stress discussed in the second paragraph of Section 3.4.5. Ultimately, the inner portion of the lamina tends to add to the transverse shear strain (in a direction tangential to the tube) of the outer portion because of the inner portion's tendency to create greater torsional tube deformation for a given transverse shear strain. This adds to the net transverse lamina shear strain as well as the tube's rotational deformation, which increases axial normal strain. Although the FE shell model accurately describes the magnitude of cross-sectional area of the tube, all stresses are evaluated at the plane of the shell and consequently, there is no capture of the through-thickness non-uniformity of normal stress existent in the tension of cylindrically anisotropic thick-walled tubes. It is for this reason that the FE model over-predicts tube stiffness when compared to the laminated cylinder model.

Examine now, in Table 4.3, the difference between the two models' predictions of the tube's an-

gular deformation that results from axial loading; again the magnitude of this difference is plotted in Figure 4.3, this time as a tightly-dashed line. The FE model's apparent under-prediction of extensional-torsional coupling in thick-walled tubes is likely due to the existence of the same non-uniform stress field discussed in the preceding paragraph. To further promote this point, examine the loosely-dotted plot in Figure 4.3 showing the error present in the polar moment of inertia of the FE shell model; the plot is very close to that of the difference in torsional deformation predictions. At this point, it is worth noting that the FE model does predict *some* extensional-torsional coupling of the tube. This may be attributed to the fact that the FE model performs CLPT on the laminate to arrive upon the behaviour of the shell, and does still capture the lamina's extensional-shear coupling that causes some of the tube's extensional-torsional coupling. The FE shell model does not, however, capture the additional coupling that results from the discussed normal stress non-uniformity.

### 4.1.3 Final Remarks

Only a select few loading cases are considered here to illustrate some key behaviours and observations that are important to the modelling of anisotropic cylinders and tubes. The FE models here are limited to ones of shell elements; as such, their viability is greatly limited in the study of thick-walled tubes. Shell element models subjected to bending, transverse shear, and pressure are not presented; theoretically, the shell model elastic response solutions to these loadings should coincide with those of classical elasticity formulae when using a material model obtained via CLPT. This is evident when comparing the solutions obtained using the laminated cylinder model to those obtained with CLPT and classical elasticity formulae for thin-walled tubes: the solutions converge as the tube's relative wall-thickness decreases.

While much was gained from the studies presented, the obvious next step would be production of either a multi-shell FE model or a solid element FE model to provide further insight into the validity of the laminated cylinder model's elastic response and elastic coupling predictions for the loading of thick-walled tubes, as well as cylinders. To that end, an attempt was made at generation of a multi-shell FE model in which concentric tubular shells of different diameter serve to capture the effects previously discussed; however, complications in tying the shells together without adding false stiffness to the model proved prohibitive. A solid element model was not produced due to time and resource constraints.

## 4.2 Experimental Program

### 4.2.1 Specimens

A total of six cylindrical beam E-glass/epoxy FRP specimens were manufactured and subsequently tested in two separate loading cases: bending and torsion. The specimens comprise two sets of three; the specimens of the first set have a unidirectional core with outer layers of fibres helically wrapped at an

alternating angle of approximately  $\pm 45^\circ$ , while those of the second set have a fibre-angle that varies linearly from  $0^\circ$  to  $\theta_{fibre}$  along the radius. Hereafter, the three samples of the first set will be designated 1A, 1B, and 1C; and those of the second set: 2A, 2B, and 2C. All specimens were manufactured with a nominal diameter of 25 mm and a nominal length of 914.4 mm. Each specimen had approximately 90 mm of length removed from each end, to ensure that the material tested is not affected by the temperature gradient toward the edges of the mould in which the specimens were cured. The glass fibres used in the core of the first set of specimens, and the entirety of the second set are Jushi<sup>®</sup> E6 312T direct rovings. The first set of specimens used helically-wound outer layers of Fibrex<sup>™</sup> TR-503-N-4900T blown fibre roving. The thermoset system used is Cass Polymers' Adtech<sup>™</sup> EP-700 epoxy with EP-802 hardener. Elastic properties for these materials can be found in Table B.1.

Each specimen was carefully measured and weighed; resulting properties are shown in Table 4.4. The specimens were weighed using a scale accurate to a tenth of a gram. Two measurements of length were obtained using a large set of calipers and then averaged, having rotated the specimen  $90^\circ$  between measurements to account for imperfect (non-perpendicular) end-cuts. Six measurements of diameter were obtained and averaged, having rotated the specimen  $90^\circ$  between the first and last three measurements to account for any ovalization that may have occurred during manufacture. Three measurements of fibre-angle were taken using an angle gauge accurate to the degree and averaged. Specimens having a core of different fibre-angle had said core measured twice on each end of the cylinder, again rotating the specimen  $90^\circ$  between the first and second measurement to account for any ovalization of the core.

**Table 4.4:** Cylindrical FRP test specimen dimensions

Sample	Mass (g)	Length (mm)	Diameter (mm)	Core Diameter (mm)	Fibre-Angle <sup>1</sup> (Degrees)
1A	640.8	733.92	25.20	13.85	52
1B	644.7	734.15	25.10	14.02	-46
1C	649.2	734.28	25.20	16.08	-47
2A	682.1	734.23	25.03		-15.67
2B	677.4	733.61	24.96		7.67
2C	680.5	734.69	25.20		10.67

<sup>1</sup>Fibre-angle measured at outer diameter of specimen. Note that 1A, 1B, and 1C all contain 11 outer layers at alternating ( $\pm$ ) fibre-angle.

## 4.2.2 Apparatus

A great deal of equipment and material was involved in the experimental testing of the specimens described in the preceding subsection; namely, a bending testing machine, a torsional testing machine, and the materials and fixtures designed to mount the specimens for torsion testing. Each of these is described in the current subsection.

### Bending Testing Machine

Three-point-bending tests were carried out using an MTS<sup>®</sup> Criterion<sup>™</sup> Model 43 electromechanical test system equipped with a 50 kN load cell. The documentation provided by MTS for the machine specifies a load cell accuracy of  $\pm 1.0\%$  of the applied force in the range of 250 N to 500 N, and  $\pm 0.5\%$  between 500 N and 50 kN. The crosshead position is provided by a digital encoder with a 0.00006 mm resolution and has a specified accuracy of  $\pm 0.5\%$ . Crosshead actuation is provided by an AC servo motor with a pre-loaded ballscrew system. Data acquisition as well as machine control was achieved using a PC running MTS<sup>®</sup> TestSuite<sup>™</sup> software, which is designed to work harmoniously with this testing machine. Data sampling was performed at 10 Hz.

The testing machine was fitted with an MTS<sup>®</sup> Model 642.25 three-point-bend fixture. The fixture, which is shown in Figure 4.4, consists of an 8.0" x 4.0" steel I-beam with its top surface ground flat and two hardened steel precision-machined rollers that sit atop billet posts clamped to the beam. The posts may be slid along the beam and clamped at the desired distance apart; a scale with graduations every 0.5 mm indicates the span distance minus roller diameter. The span was set to 550 mm, providing a distance between the 40 mm rollers (bending span) of 590 mm  $\pm 0.25$  mm. A similar roller and post was used to provide the applied load and is also shown in Figure 4.4.

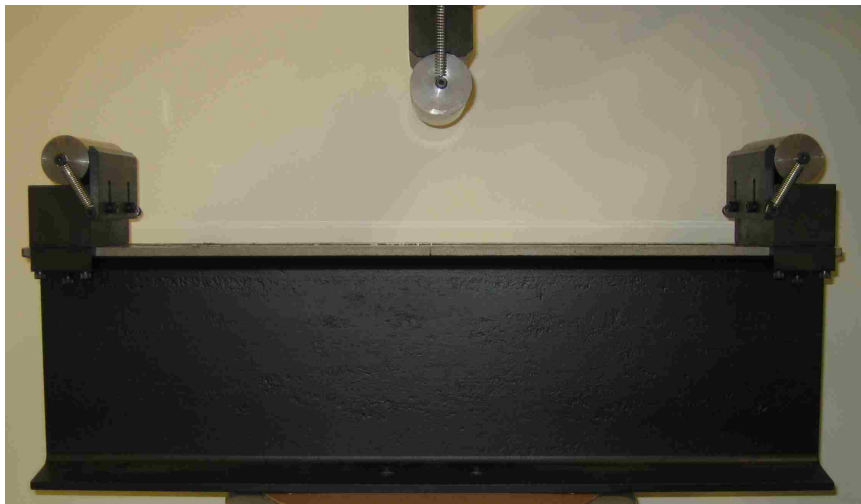


Figure 4.4: MTS<sup>®</sup> Model 642.25 Bend Fixture

### Torsion Testing Machine

A torsion testing machine appropriate for the expected specimen stiffness and necessary specimen length was not readily available; consequently, it was necessary to design and build one. Relevant details of the machine structure as well as sensor and data acquisition information will follow. Also outlined are the material and fixtures needed to mount the specimens to the torsion testing machine.



Figure 4.5: Torsion Testing Machine

**Machine Structure:** The machine seen in Figure 4.5 was designed by the author and a colleague[20] having similar motives; machining and assembly was commissioned to a local manufacturing company, REKO Manufacturing Group Inc. Much consideration went into producing a machine that is versatile, adjustable, and robust. A capability was desired to characterize the stiffness of specimens at least one meter in length, but maintain an adjustable fixture set, such that shorter specimens can be easily accommodated. It was expected that the machine would need to produce values of torque over 1000 Nm, while still harbouring a capacity to accurately measure torques well under 100 Nm. Ability to produce at least 45° of torsional deformation was needed, with accurate measurement thereof.

The machine is composed fundamentally of three fixtures: a ‘live-end’ fixture that serves to produce and measure rotation as well as torque at one end of the specimen, a ‘dead-end’ fixture to restrict rotation at the opposing end of the specimen, and a flat rigid base upon which the fixtures are mounted.

**Machine Base:** The base of the machine is a welded box section having four legs of hollow structural steel channel. The top of the box section is a 1600 mm by 450 mm steel plate of 15.875 mm thickness that has been blanchard ground to provide a flat surface on which to mount the fixtures. The box section alone was designed to have a stiffness at least 100 times greater than that of the stiffest spec-



imen to be tested. The legs are bolted to a ground-level concrete floor to further stiffen the assembly; high stiffness is critical to the design, as any torsional flexure of the machine affects the measurement of torsional deflection in the specimen.

**Dead-End Fixture:** The dead-end fixture consists of a 19.05 mm thick plate positioned perpendicularly to the base. This plate is welded to a bottom plate that mounts to the base, as well as to two triangular gussets that support the main dead end fixture plate. A number of holes are bored in a circular pattern through the dead-end fixture plate to allow the mounting of specimens or specimen flanges. The entire dead-end fixture bolts to the base by four bolts and is aligned by two precision dowels. The base features a number of mounting holes and dowel holes arranged with a longitudinal spacing of 130 mm to allow mounting of the dead end at various positions, corresponding to various specimen lengths.

**Live-End Fixture:** The live-end fixture, which is mounted to the base and opposes the dead-end, is also a weldment of 19.05 mm plate bolted in place with dowels for alignment. While the live-end fixture as a whole may be seen in Figure 4.5, the functional components that are described in this paragraph are best understood from a simplified line drawing: see Figure 4.6. Two heavy duty ball bearings pressed into the live-end fixture plates support a 50 mm main shaft that serves to transfer torsional loading into the second mounting point of the specimen. On the inbound end of the main shaft is the live-end mounting plate having the same bolt pattern found on the dead-end, with the same purpose of specimen mounting. A large sprocket is affixed to the center of the main shaft by two keys and held in place between the bearings with set-screws. A 530 series roller chain, which mates with the sprocket, is pulled downward toward the base by an Acme-threaded rod to create angular motion of the live-end mounting plate, imposing a torque on the specimen. Rotation of a wheel and nut pulls the rotationally-fixed Acme-threaded rod downward through the base. The top end of the threaded rod is connected to the hanging end of the chain by a load cell with a U-joint at each end. Consequently, the downward pull on the chain may be monitored and knowledge of the sprocket radius allows determination of applied torque. A rotary potentiometer is fixed to the stationary part of the live-end fixture, having its actuator shaft mated with the main shaft. The unloaded side of the chain hangs freely from the sprocket with a counter-weight attached to balance the weight of the load cell and threaded rod assembly.

**Sensors and Data Acquisition:** The torsion testing machine utilizes two sensors and a data acquisition system, described as follows.

**Load Cell:** While the machine was designed to allow the use of different load cells depending on the desired range of torque application, only one load cell was used during the torsion tests discussed in the current manuscript: a 1.33 kN capacity Model 60001 S-beam load cell manufactured by Sensortronics™ of Vishay® Precision Group. The calibration data supplied with the load cell specifies a sensor output

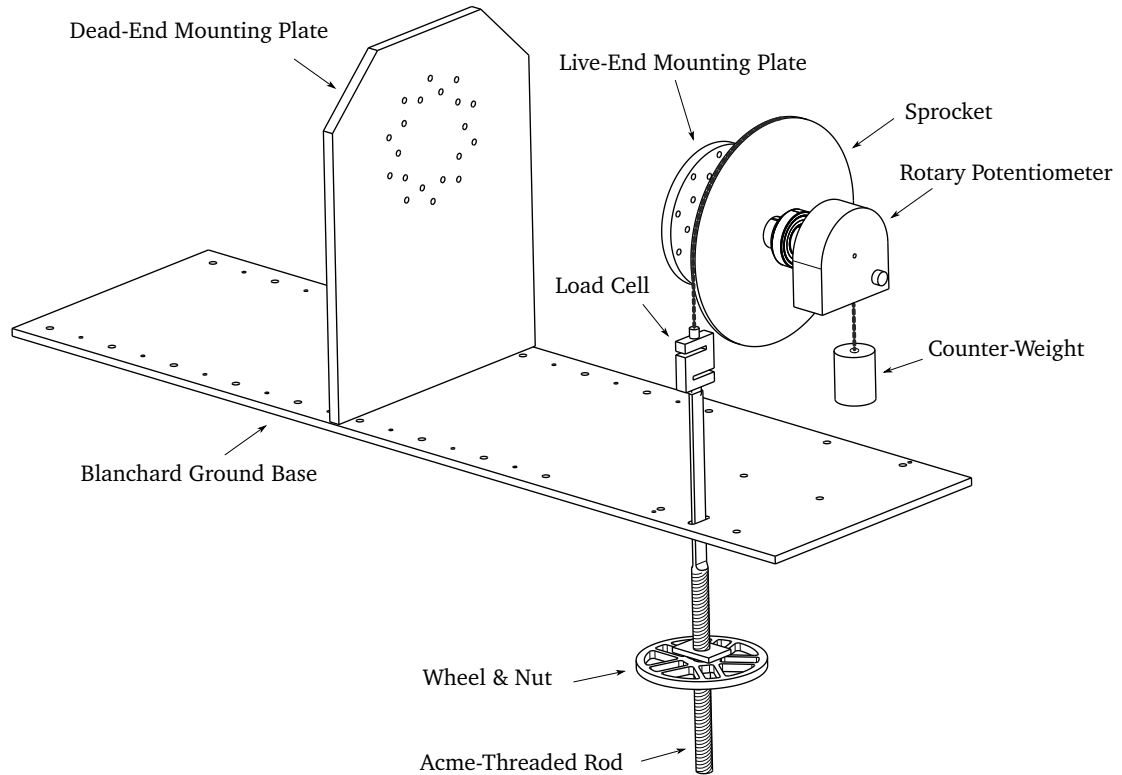


Figure 4.6: Primary-function components of torsion testing machine

of 3.582 mV/V. The NTEP<sup>®</sup> Class III rating gives a combined error of  $\pm 0.02\%$  of full scale ( $\pm 0.267$  N, or  $\pm 47.22$  N·mm as pertaining to the machine). Non-repeatability is listed as  $\pm 0.01\%$  of full scale ( $\pm 0.134$  N, or  $\pm 23.71$  N·mm). As recommended by the manufacturer, the load cell was supplied a 10 V excitation.

**Rotary Potentiometer:** A Celesco<sup>™</sup> Model RT9101-001-131-4110 rotational position transducer with a  $360^\circ$  range was affixed to the machine, having its actuator shaft mated with the machine's main shaft. The specifications of the sensor are as follows: sensor output is 2.661 mV/V/degree, specified calibration accuracy is  $\pm 0.179\%$  of the reading, repeatability is  $\pm 0.02\%$  of full stroke ( $\pm 0.072^\circ$ ), and resolution of the plastic-hybrid precision potentiometer sensor is essentially infinite. A 10 V input signal was supplied to the rotary potentiometer.

**Data Acquisition System:** Data was processed and recorded using a System 8000 StrainSmart<sup>®</sup> Data Acquisition System manufactured by Micro-Measurements<sup>®</sup> of Vishay<sup>®</sup> Precision Group. The system communicates over an ethernet network to a PC running the included StrainSmart<sup>®</sup> software, which allows adjustment of parameters pertaining to calibration and sensor excitation voltage, among others.

Sensor excitation as well as sensor signal is transmitted through an eight pin RJ45 connector. Each signal is read by a channel-specific, 24-bit analogue-to-digital converter and filtered to remove noise. Data is processed by a 32-bit, floating-point, digital signal processor operating at 300 MHz. Strain-gauge-based, millivolt-level, sensor (e.g. load cell) readings are measured with a  $0.25 \mu\text{V}$  resolution and amplified with a DC gain accuracy of  $\pm 0.05\%$ . High-level sensor (e.g. potentiometer) readings are measured with a  $100 \mu\text{V}$  effective resolution. The system's excitation voltage accuracy is  $\pm 10 \text{ mV}$  with a resolution of  $3 \text{ mV}$ .

**Mounting Fixtures and Material:** A means was required to rigidly affix the torsion test specimens to the live-end and dead-end mounting plates of the torsion machine. Sets of rectangular aluminium plates were manufactured and secured to the ends of the specimens with an epoxy joint. The  $26 \text{ mm}$  thick plates were water-jet cut with a mounting hole at each corner, and subsequently drilled to have a stepped hole in their center. The stepped hole served to precisely locate the specimen, while allowing a  $0.75 \text{ mm}$  thick layer of epoxy to bond the  $25 \text{ mm}$  diameter specimens to the inner surface of the bored hole. The stepped section of the hole amounts to only  $3 \text{ mm}$  of thickness, leaving a  $23 \text{ mm}$  thick by  $27 \text{ mm}$  diameter bonding area. The bond thickness was kept relatively low to ensure that the shear deformation of the epoxy itself does not significantly contribute to the measurement of torsional deflection. Epoxy typically displays a strain-to-failure of approximately  $2.0\%$  [5], and so the joint will likely fail before any significant torsional deformation is present.

The aluminium plates as well as the specimens were prepared with 80-grit sandpaper and cleaned with isopropyl alcohol before being bonded together with Henkel LePage<sup>®</sup> Gel Epoxy (Henkel product number 1165246). Henkel reports the epoxy's tensile strength as  $13.355 \pm 0.614 \text{ MPa}$  when adhered to sandblasted aluminium and cured for at least 24 hours. In accordance, each specimen/plate set was allowed 24 hours of cure time before testing began. The specimen/plate assembly was bolted into the machine immediately after the epoxy was applied and remained in place during cure to ensure perfect alignment. Once fixed in the testing machine, distance between the aluminium mounting plates was measured as  $682 \pm 0.5 \text{ mm}$ . A line was drawn across the bonded joint from the aluminium plate onto the specimen to allow easy detection of any slippage in the joint – there was none.

### 4.2.3 Three-Point-Bending Tests

The six specimens described in Section 4.2.1 were tested in three point flexure using the setup described in detail in Section 4.2.2 and seen in Figure 4.7. Each specimen was subjected to at least five mm of mid-point deflection. The force-displacement curve produced by each test was fitted with a linear trend-line to determine the slope, or spring-rate, in the linear regime of the test.

The slope obtained from the data corresponding to each test was used to determine the flexural rigidity  $EI$  for each specimen. This was accomplished by a rearrangement of the Euler-Bernoulli equation

for deflection of a simply supported beam point-loaded at its midspan (Equation 4.1).

$$EI = \frac{-PL^3}{48x} \quad (4.1)$$

where  $x$  is the midspan beam deflection,  $P$  is the applied load,  $L$  defines the span length, and  $EI$  is the beam's flexural rigidity.

The value of  $EI$  extracted from each experiment is compared to that which was calculated by the laminated cylinder model; a prediction of  $EI$  may be obtained by taking the inverse of the  $m_{22}$  or  $m_{33}$  terms of the compliance matrix seen in Equation 3.39. However, this prediction does not include the effects of transverse shear load, while the experimentally obtained flexural rigidity does; to remedy this, an effective flexural rigidity was calculated using the  $m_{99}$  shear compliance term, and added to the aforementioned  $EI$  prediction using a series spring-rate summation. The input to the laminated cylinder model is shown and discussed for each specimen in Appendix B.

The experimentally determined flexural rigidity, the predicted flexural rigidity (including transverse shear<sup>1</sup>), and the error observed in comparing the predicted value to the experimental is shown for each specimen in Table 4.5.



Figure 4.7: Experimental setup: three point flexure test (sample 1C)

---

<sup>1</sup>Note that in this case ‘transverse shear’ refers to through-thickness transverse shear, not to be confused with the Timoshenko shear effects that are not included in the current laminated cylinder model.

**Table 4.5:** Three point flexure test: experimental results and laminated cylinder model predictions for each specimen

Specimen	$EI$ (Experimental) (N·mm <sup>2</sup> )	$EI$ (Predicted) (N·mm <sup>2</sup> )	Error (%)
1A	278.0 x 10 <sup>6</sup>	217.9 x 10 <sup>6</sup>	-21.6
1B	312.8 x 10 <sup>6</sup>	245.5 x 10 <sup>6</sup>	-21.5
1C	362.3 x 10 <sup>6</sup>	287.0 x 10 <sup>6</sup>	-20.8
2A	672.5 x 10 <sup>6</sup>	691.2 x 10 <sup>6</sup>	2.8
2B	740.0 x 10 <sup>6</sup>	806.3 x 10 <sup>6</sup>	9.0
2C	712.3 x 10 <sup>6</sup>	765.9 x 10 <sup>6</sup>	7.5

#### 4.2.4 Torsion Tests

The six specimens described in Section 4.2.1 were tested in torsion using the setup described in detail in Section 4.2.2 and seen in Figures 4.8 and 4.9. The torsion beam span of the specimens was measured to be 682 ±0.5 mm. Each specimen was subjected to at least 10° of rotation. Trend-lines were fit to the linear regime (between zero and six degrees in this case) of plots showing applied torque versus rotational displacement. The slope of each trend-line represents the measured torsional stiffness of the corresponding specimen in N·mm/degree. In a treatment analogous to that of Equation 4.1, a value of torsional rigidity  $JG$  may be extracted from the experimental data using Equation 4.2: a rearrangement of the classical formula for torsional deflection of a solid beam of circular cross-section.

$$JG = \frac{TL}{\phi} \quad (4.2)$$

where  $\phi$  is the angular deflection,  $T$  is the applied torque, and  $L$  is the torsion span length.

The laminated cylinder model's prediction of torsional rigidity may be obtained by calculating the inverse of the  $m_{77}$  term in Equation 3.39. This produces a value of  $JG$  in N·mm<sup>2</sup>/radian which may be converted to N·mm<sup>2</sup>/degree. The experimentally obtained torsional rigidity, the predicted torsional rigidity, and the error observed in comparing the predicted value to the experimental is shown in Table 4.6. As was mentioned, the input to the laminated cylinder model is shown and discussed in Appendix B.



**Figure 4.8:** Experimental setup: torsion test (live-end with specimen 2A mounted)



**Figure 4.9:** Experimental setup: torsion test (dead-end with specimen 2A mounted)

**Table 4.6:** Torsion test: experimental results and laminated cylinder model predictions for each specimen

Specimen	$JG$ (Experimental) (N·mm <sup>2</sup> /degree)	$JG$ (Predicted) (N·mm <sup>2</sup> /degree)	Error (%)
1A	$4.057 \times 10^6$	$6.383 \times 10^6$	57.4
1B	$4.213 \times 10^6$	$6.756 \times 10^6$	60.4
1C	$4.368 \times 10^6$	$6.460 \times 10^6$	47.9
2A	$3.576 \times 10^6$	$3.015 \times 10^6$	-15.7
2B	$2.968 \times 10^6$	$2.544 \times 10^6$	-14.3
2C	$3.148 \times 10^6$	$2.639 \times 10^6$	-16.1

#### 4.2.5 Discussion

There is a distinct difference in the accuracy of the model's stiffness predictions between the 1X-series and 2X-series sets of specimens. For the 1X-series set of specimens, the error in stiffness prediction is over 20% for bending, and as high as 60% in the case of torsion. The 2X-series specimens, however, were found to have a bending stiffness prediction error within less than 10% and a torsional stiffness prediction error of 16% or less. This marked difference in accuracy could mean two things: the model is particularly erroneous for configurations such as those of the 1X-series specimens, or that the material configuration and properties have been poorly quantified in the case of the 1X-series specimens. The following paragraphs will discuss why the latter is a likely culprit.

The fibre-angle of all specimens was measured at the outer diameter. Without the use of a closed-loop control system in the manufacture of these specimens, the outer diameter may or may not be a good indication of the fibre-angle throughout the specimen. The standard deviation of the fibre-angle measurements is 3.5°, 2.6°, and 6.1° for specimens 1A, 1B, and 1C, respectively; for the 2X-series specimens, it was 0.6°, 1.5°, and 1.2° for 2A, 2B, and 2C, respectively. It is clear that even the variation through the specimen length is quite large for the 1X-series specimens.

The measurement of core diameter is another source for error in the quantification of the 1X-series specimens. The standard deviations of core diameter measurements was 0.3 mm, 0.6 mm, and 0.6 mm for specimens 1A, 1B, and 1C, respectively. The 2X-series specimens have no distinct core and consequently, no core measurements.

The shear modulus for the glass fibre as well as for the epoxy matrix has been calculated as a function of a manufacturer's listed elastic modulus and an assumed value of Poisson's ratio. No coupon testing was performed to establish these material properties as the manufacturing process utilized here does not lend itself to the manufacture of ASTM standard test coupons. The lack of elastic modulus estimates gathered from physical testing is of particular importance because the elastic moduli of the epoxy matrix can vary depending on variables such as temperature, cure time, cure temperature, and mix quality, among others. The 1X-series specimens are particularly sensitive to matrix shear modulus

when subjected to bending stress, as the principal stresses in the material are not aligned with the fibre direction; an erroneous estimate of shear modulus can have a large effect on predicted bending stiffness accuracy. Strictly speaking, the torsional stiffness of a specimen with a fibre-angle of  $\pm 45^\circ$  is not affected by matrix shear modulus at all, as the principal stresses are oriented along and perpendicular to the fibre-direction; torsional stiffness of this type of specimen is governed by Young's modulus in tension and compression. What this says is that the torsional stiffness predictions of the 1X-series specimens is influenced heavily by elastic modulus estimates for both the fibre and matrix.

As a result of the vast difference in moduli between fibre and matrix, the fibre-volume fraction has a substantial effect on the stiffness of a lamina. The 1X-series specimens have a unidirectional  $0^\circ$  core of non-blown fibre roving, i.e., fibres that are tightly bundled together in their roving. The fibres that make up the outer layer are blown-fibre roving, meaning they have been blasted with compressed air to spread out the roving and increase resin absorption. Compounding this differential in fibre packing densities, the fibre-angle of outer layers of the 1X-series specimens are alternating from layer to layer, forming voids between the overlapping fibres – voids which are filled by resin, reducing the net fibre-volume fraction of the laminate. The point here is that in the 1X-series specimens, a difference likely exists between the fibre-volume fraction of the core and that of the outer layers. The assumption inherent to the method that was used to determine the fibre-volume fraction is that the fraction is uniform and homogeneous throughout the specimen; as a result the core has likely been given an under-predicted fraction, while the outer layers are likely over-predicted. This could explain some of the torsional stiffness over-prediction of the 1X-series specimens, especially when considering that the outermost layers generally contribute the majority of specimen torsional stiffness. However, if this is the case, the bending stiffness under-prediction is greater than shown.

A brief sensitivity study reveals that the uncertainty in measurements and properties could quickly compound on each other and produce relatively large margins or error. In the cases of both bending and torsion of the 1X-series specimens, 5% changes were made to certain input variables, and the change in the model's deformation prediction was recorded. The variables changed were fibre angle, core diameter, fibre-volume fraction at the outer layers  $V_f$ , fibre modulus in the outer layers  $E_f$ , and matrix modulus in the outer layers  $E_m$ . The results are shown in Table 4.7, where  $\Delta\phi$  represents the change in torsional deformation that results from a 5% change in the variable/property when the cylinder is subjected to torsion, and  $\Delta\kappa$  represents the change in curvature that results from a 5% change in the variable/property when the cylinder is subjected to constant bending moment.



**Table 4.7:** Sensitivity of the model's elastic response prediction to input variables and properties

<b>Variable/Property</b>	<b><math>\Delta\phi</math> (%)</b>	<b><math>\Delta\kappa</math> (%)</b>
Fibre Angle	3.8	2.6
Core Diameter	1.3	5.3
$V_f$ Outer	4.9	3.4
$E_f$ Outer	4.1	0.5
$E_m$ Outer	0.9	2.8

## Chapter 5

# Anti-Roll Bar Analysis & Design

The composite anti-roll bar (ARB) has been designed to match the stiffness and *some* geometrical attributes of an existing steel anti-roll bar. No information was made available regarding the desired force-displacement characteristics of the composite anti-roll bar, or the geometric envelope within which it may exist. Consequently, it was necessary to benchmark the existing steel anti-roll bar with the aim of replicating its stiffness.

The present chapter is broken into two sections, the first of which describes the benchmarking procedure used to characterize the steel bar. The second section details the design of the composite bar; software is developed and used to establish a configuration that meets the defined design criteria.

The geometry of the steel bar is depicted in Figure 5.1. The indicated loading points receive opposing forces in and out of the page while the bushings are rigidly mounted to the vehicle body. The compliance of the bar will be defined as the relative vertical displacement of the endpoints per unit force applied in opposition; the stiffness of the bar is the inverse of this.

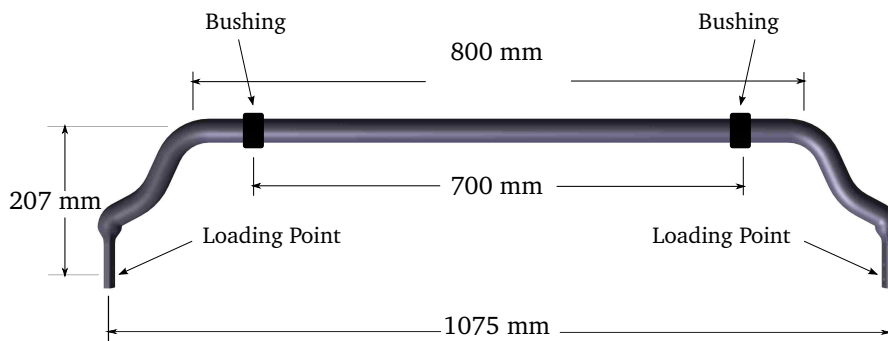


Figure 5.1: Geometry of existing steel anti-roll bar

## 5.1 Benchmarking of the Steel Anti-Roll Bar

The steel anti-roll bar is benchmarked using three methods: conventional analytical methods, a finite element analysis, and experimental testing. Each of these methods is described in detail in the sections that follow.

### 5.1.1 Classical Analytical Methods

If the geometry of the steel ARB is simplified to what is shown in Figure 5.2, it can be analysed with relative ease using the classical formulae for Saint-Venant torsion and Euler-Bernoulli bending of beams applied to each section of the bar. The bar is broken into three elastic sections: a mid-section 800 mm wide, and two cantilevered sections 270 mm in length oriented at 50° to the mid-span. Two short sections exist at the endpoints but are assumed rigid due to their short length and larger moment of inertia – these sections are the only portion of the steel bar in which the cross-section varies from circular to rectangular. The loading points are at a perpendicular distance of 47.5 mm from the mid-axis of the cantilevered sections, and are separated from each other by 1075 mm of horizontal distance. The compliance of the bar is assumed to consist of four contributions: torsion of the mid-span, bending of the midspan, bending of the cantilevered arms, and torsion of the cantilevered arms caused by loading which is offset to their shear-center. Each section of the bar is analysed with regard to its contribution to the bar's overall stiffness.

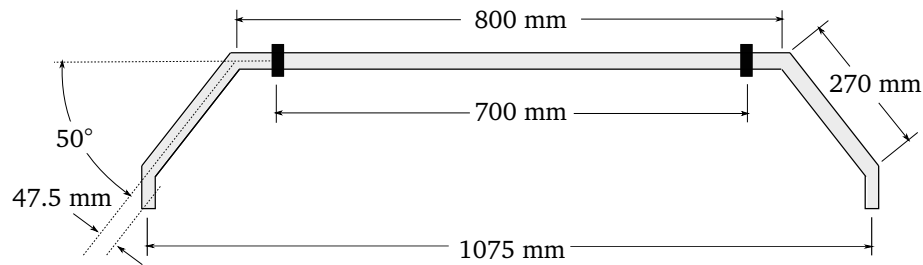


Figure 5.2: Simplified anti-roll bar geometry: plan view

The torsional spring-rate of the mid-span is easily calculated as  $\frac{JG}{l}$  and will have units of N·mm/rad. This angular spring-rate can be converted into an effective linear spring-rate in our context with the following unit conversion:

$$\frac{\text{N}\cdot\text{mm}}{\text{rad}} * \frac{\text{N}}{207 \text{ N}\cdot\text{mm}} * \frac{\pi \text{ rad}}{(207 \text{ mm})(\pi \text{ rad})} = \frac{\text{N}}{42849 \text{ mm}} \quad (5.1)$$

This converted rate represents the linear spring-rate which would exist at a fixed moment arm of 207 mm (recall that 207 mm is the perpendicular distance from the loading point to the mid-span). Ultimately,

**Table 5.1:** Stiffness contributions in steel anti-roll bar

Form of Compliance	Linear Spring-Rate (N/mm)
Mid-Span Torsion	261.13
Mid-Span Bending	1892.25
Cantilevered Section Torsion	86886.51
Cantilevered Section Bending	1771.57
Overall Linear Spring-Rate:	181.87

this means that the contribution of the mid-span to the overall bar stiffness is equal to:

$$\frac{JG}{42849(l)} \text{ N/mm} \quad (5.2)$$

where  $J$  is the polar moment of inertia of the cross-section,  $G$  is the shear modulus of the steel, and  $l$  is the length.

Torsion of the cantilevered section due to offset loading can be accounted for in a manner analogous to the treatment of the mid-span torsion; the only difference being that the moment arm in the current case is 47.5 mm

Bending of the cantilevered sections and of the midspan can be found by evaluating the linear spring-rate for a beam in bending as  $\frac{3EI}{l^3}$ , where  $E$  is Young's modulus, and  $I$  is the area moment of inertia of the cross-section. Timoshenko shear effects are included in the calculations, but are a negligible contribution to compliance.

The individual contribution to overall bar stiffness of each type of compliance is shown in Table 5.1. Each of the shown spring-rates is superimposed by a series spring calculation, to arrive at the overall anti-roll bar stiffness.

### 5.1.2 Finite Element Analysis

A CAD model of the steel ARB was established using the geometric specifications provided by its manufacturer. The inherently anti-symmetric loading of the symmetric bar allows the use of special constraints and a half-model. Meshing and preprocessing was performed using Altair<sup>®</sup> Hypermesh<sup>®</sup>, and the model was solved using the linear static solver of RADIOSS<sup>®</sup>.

#### Model Architecture:

The majority of the bar is of constant circular cross-section, meaning that it can be meshed using a solid FE map. To that end, a two-dimensional mesh of quadrilateral elements was swept along the length of the bar to create a number of eight-noded CHEXA solid elements. The nominal length of the solid elements (specified during their creation) was chosen to be equal to the average length of elements

in the two-dimensional mesh and was different for each model in the convergence study to be shown. Consequently, elements resemble cubes as closely as possible while still capturing the desired geometry. However, the elements at the inner radius in curved portions of the bar tend to attain high aspect-ratios, becoming short in length relative to their width and height. This issue was negated by carefully selecting an edge-density<sup>1</sup> that lessens the severity of element aspect-ratios at the cost of increasing average element length. The maximum aspect ratio in the finest mesh was 4.8, and only 1% of the elements exceeded an aspect ratio of 2.0.

The end of the bar is forged into a rectangular cross-section with holes drilled at the loading points. While this section and its transition into the circular section are both mappable, use of solid mapping produces a heavily distorted mesh between the rectangular and circular cross-sections. Instead, tetrahedral elements were used to fill the volume of these sections. While it is generally known that first-order tetrahedral elements produce erroneously stiff results in bending-dominated problems, it should be noted that the portion of the bar containing tetrahedral elements is small and at a low bending moment. Furthermore, this section has little contribution in terms of additional bar compliance due to the fact that its area moment of inertia is much larger than that of the circular cross-section which contains equal volume. An example of the full mesh can be seen in Figure 5.3

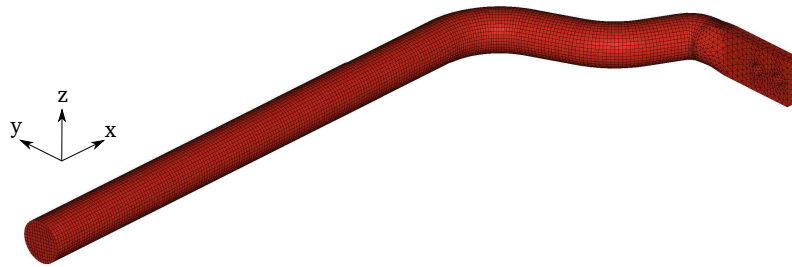


Figure 5.3: Solid element mesh (2.5 mm nominal element length)

There are two boundary conditions that constrain the bar: the anti-symmetric loading condition, and the bushing. The anti-symmetric loading condition has been addressed by attaching the independent nodes of a rigid body (RBE2) element to the symmetry-plane face of the half-bar. The rigid element's dependent node is located at the center of this face and is constrained with an SPC in  $x$  and  $z$  translation, as well as in rotation about the  $x$  axis. No effort has been made to model the compliance associated with that of the bushings; the rationale should be clear in the subsection that follows. The bushing is instead assumed rigid; however, axial translation of the bar within the bushing is permitted, as well as rotation in all directions. The modelling of the bushing constraint is similar to that of the anti-symmetric loading: a rigid body (RBE2) element has its dependent node located such that it represents the center

<sup>1</sup>Edge-density defines the number of elements along the length of a particular edge

of the bushing, while the independent nodes are connected to the surface of the bar – where the bushing would make contact. The dependent node is then constrained with an SPC to restrict translation in the  $y$  and  $z$  directions. Both the bushing and anti-symmetry condition constraints can be seen in Figure 5.4.

It should be noted that rigid body elements, and in particular RBE2 (true rigid) elements, can add unrealistic stiffness to a model. However, this particular case should not produce great concern as the areas affected by the rigid elements are small in relation to the bar. The use of an interpolation element such as an RBE3 may have alleviated some of the induced stiffness, but RBE3 elements do not allow the use of an SPC at the dependent node. Without an SPC restricting the motion of the bar's symmetry-plane face, the model is under-constrained.

A 5 kN force was applied in the  $z$  direction at the loading point of the bar. The force was distributed to the nodes at the inner surface of the hole using an RBE3 element as shown in Figure 5.4.

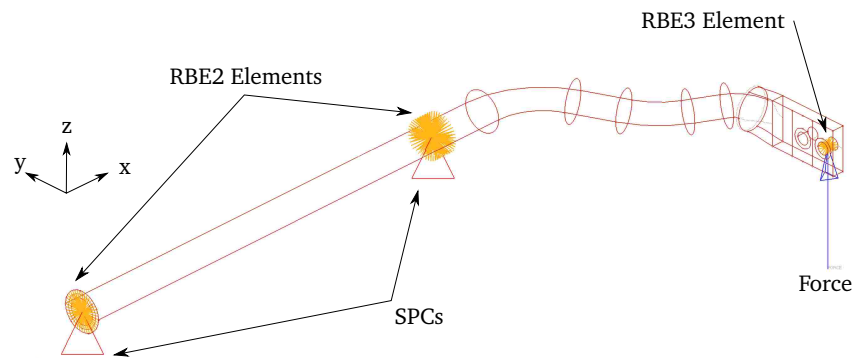


Figure 5.4: Wireframe model showing constraints and applied loading

### Mesh Sensitivity Study:

The analysis was performed using a number of progressively finer meshes to ensure the solver had converged upon a solution.

The solid map used to mesh the constant cross-section length of the bar was generated using a nominal element size ranging from 5 mm to 1.25 mm. The tetrahedral mesh at the loaded end of the bar was re-meshed in each case to allow proper transition into the newly mapped hexahedral mesh. Aside from this, the nominal element size (4 mm) of the tetrahedral mesh was not changed throughout the study. Some properties of the meshes used can be found in Table 5.2. The 5 mm and 1.25 mm meshes are shown in Figure 5.5. The trend of the linear spring-rates extracted from the study is shown in Figure 5.6. Note that only 0.9% difference separates the 2.5 mm and 1.25 mm meshes, an indication that sufficient convergence has been achieved. The solution of linear stiffness resulting from the classical analysis is shown on the plot to allow convenient comparison between classical and numerical solutions; the finest mesh results in a stiffness within 0.04% of the classical analysis result. Careful inspection

of the plot will reveal that perhaps an even finer mesh would produce slightly stiffer results than the classical analysis, but it is unlikely that this differential would be at all substantial.

**Table 5.2:** Steel ARB finite element mesh-sensitivity study data

Nominal Element Length (mm)	Number of Elements	Computing Time <sup>1</sup> (s)	Resulting Linear Spring-Rate (N/mm)
5.00	6536	0	171.53
4.00	16783	4	176.80
2.50	38387	12	180.24
1.25	323049	409	181.80

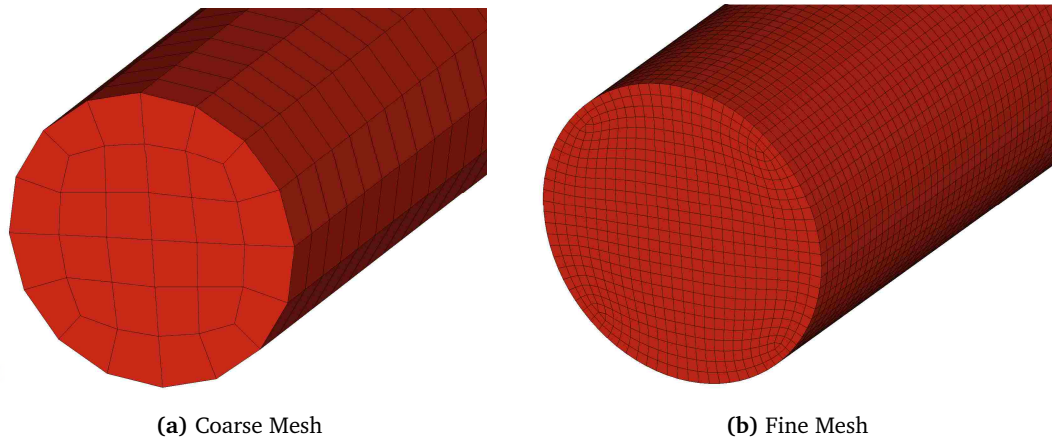


**Figure 5.5:** Coarsest and finest mesh used in steel ARB convergence study

<sup>1</sup>Analyses were performed on a PC running Microsoft® Windows® 7 Professional (64 bit) with an Intel® Core™ i7-2600k CPU @ 3.40 GHz. The PC was equipped with 16 GB of RAM.

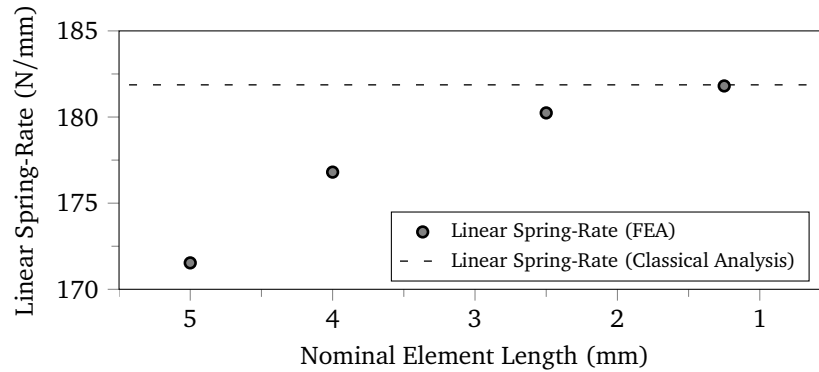


**Figure 5.6:** Steel ARB finite element solution convergence: linear spring-rate vs. element size

### 5.1.3 Experimental Testing

Physical testing was performed on the existing steel bar as part of the benchmarking regimen. The test setup geometry was as shown in Figure 5.1 with bushings spaced at 700 mm center-to-center. The bushings were mounted to square-channel structural steel pillars that were bolted to a steel platen table. The loading point at one end of the bar was pinned to a steel yoke and pillar (see Figure 5.7). At the opposing loading point, a hydraulic cylinder was used to produce the applied load, which was transmitted into the bar by a steel yoke and pin. A button-style load cell was positioned between the yoke and the hydraulic cylinder to measure the applied force; this can be seen in Figure 5.8. A height gauge indicated the vertical displacement of the yoke. Load cell force measurements were taken at three incremental values of vertical displacement during the quasi-static tests with the intent of gaining perspective on the linearity of the bar's elastic response.

The first set of tests was performed using the polymer bushings that were provided with the bar; these bushings can be seen in Figure 5.7. Results are averaged from three tests and shown in Table 5.3. Significant deformation of the bushings produced values of stiffness that are not a good representation of the bar's elastic response – much of the measured compliance was a direct result of bushing deformation. For this reason, further testing was performed using a set of steel bushings, each bushing comprising two mating halves to encase the bar (see Figure 5.8). The steel bushings were mounted in the same manner as with the previous tests, after being greased to reduce friction between the bar and the bushings. The results, again averaged over three tests, can be seen in Table 5.4.





**Figure 5.7:** Physical testing setup: fixed end with polymer bushing



**Figure 5.8:** Physical testing setup: actuated end with steel bushing

**Table 5.3:** Steel ARB test (polymer bushings)

Deflection (mm)	Load (N)	Linear Spring-Rate (N/mm)
10	1230.7	123.07
20	2584.4	129.22
30	4510.2	138.34

**Table 5.4:** Steel ARB test (steel bushings)

Deflection (mm)	Load (N)	Linear Spring-Rate (N/mm)
10	1786.7	178.67
20	3647.5	182.38
30	5627.0	187.57

## 5.2 Composite Anti-Roll Bar

Conventional FRP materials rarely offer an elastic modulus as high as that of steel even at their stiffest fibre angle; this deficit between moduli only increases as the loading direction deviates from that which is optimal. Because of this, the composite bar must be of a larger diameter than the steel to provide comparable stiffness. In lieu of a geometric design envelope, it is assumed that the diameter of the bar may be increased moderately but that the basic shape may not change.

### 5.2.1 Analysis Software

It is possible to design a computer program that will establish the state of loading in each section of a discretized ARB given a known applied force. It was mentioned in Section 3.3 that a computer program was developed that quickly and efficiently computes a solution to the elastic response of a laminated FRP tube or cylinder subjected to arbitrary loading. A program has been developed, again in the MATLAB<sup>®</sup> environment, that communicates with the aforementioned elasticity model software to determine the deformed shape of a composite ARB subjected to a known force at its loading point. The code is included in Appendix D.

The program, henceforth referred to as CARBA (Composite Anti-Roll Bar Analysis), accepts a user-generated list of coordinates in spreadsheet form to describe the shape of the ARB. A number of assumptions are employed to simplify the program:

1. The desired line geometry of the ARB is known and exists within a two-dimensional plane. Furthermore, the cross-section of the bar is circular and is centered about the known line geometry.

2. The ARB is not a curved beam, but a beam comprising a number of straight sections subjected to small and linear deformation.
3. The ARB is subjected to a known force at the first and last points listed in the coordinate spreadsheet. These points are loaded in opposing directions that are perpendicular to the two-dimensional plane in which the bar exists.
4. Exactly two bushings constrain the ARB at the point on the bar coincident with the bushing. The bar is constrained by the bushings only in translation, and the bushing locations are specified in the coordinate spreadsheet by the user.
5. Loading points and bushings are symmetrically located with respect to a vertical line passing through the center of the bar.

As an example, a simple geometry is shown in Figure 5.9, where the points are indicated by the 'x' marks, and bushings are circled. The line about which the loading points and bushings must remain symmetric is represented by the dashed line.

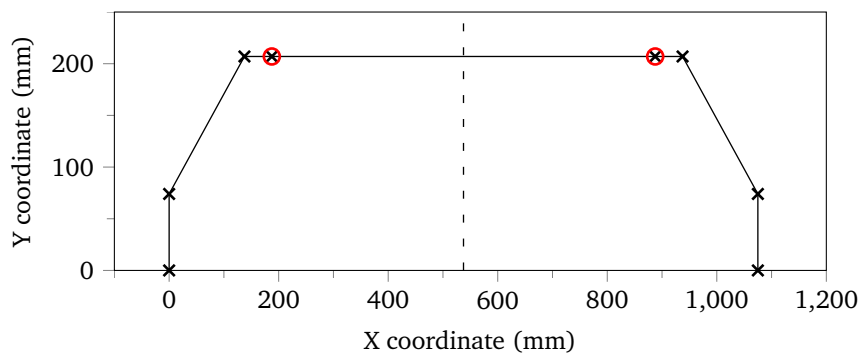


**Figure 5.9:** Line geometry input to CARBA software (congruent with classical analysis)

### Software Structure:

The CARBA software imports the user-defined line geometry and calculates the length and orientation of each section. Under assumptions two and three, the moments and transverse shear force at each point can be calculated with respect to the global X-Y coordinate system. The global loading state at each point is resolved into a local coordinate system to describe the loading in the sections adjacent to the point (e.g., if two sections are perpendicular to each other, the bending moment in the first section will equate to the torque in the second and vice-versa). The torsion within a section is modelled as constant, while the bending moment may be a function of position; locations closer to the bushing are generally subjected to greater bending moments. Each section is further discretized into a number of straight

beams (subsections) to allow a linear interpolation of bending moment along the length of that section. The transverse shear force in the bar is ultimately constant in three regions of the bar – separated by the bushings.

The state of loading now defined for each section and subsection of the bar is input individually to the laminated cylinder model; an elastic response corresponding to each section and subsection is returned. Starting at the bushings and working outward toward the end points, the strain and curvature resultants returned by the laminated cylinder model are used to compute the vertical displacement of the bar at all points. Prior to this, however, the deformation in the mid-region (between the bushings) is determined to allow definition of boundary conditions (slope and torsional deflection) required to quantify deflection of the outer regions of the bar.

The vertical displacement corresponding to each user-input point is displayed in a plot. Figure 5.10 shows the plot generated with a 1 N force applied at the loaded ends of the bar shown in Figure 5.9. The value of deflection at the loading points can be extracted and resolved into a compliance (mm/N). Because the applied force is simply 1 N, an inversion of the total relative displacement between the loaded ends produces a linear stiffness compatible with those found during the benchmarking of the steel bar in Section 5.1.

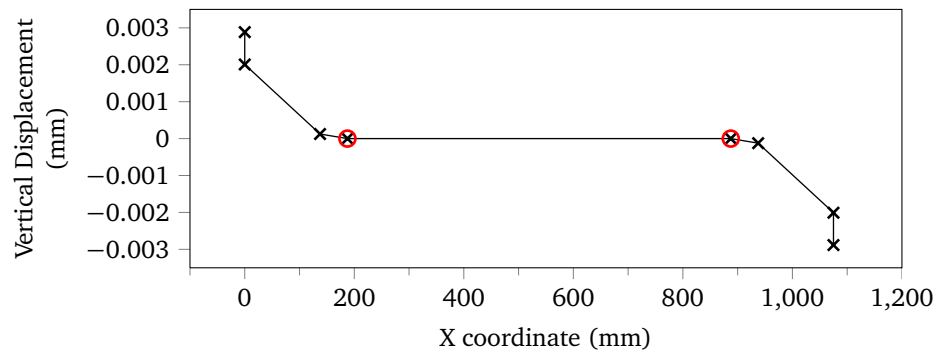


**Figure 5.10:** Vertical displacement profile output from CARBA software for the steel bar

### Validation:

An example representing the geometry which is used in the classical analysis of Section 5.1.1 was shown in Figure 5.9; both this geometry, and the material properties used in the classical analysis were input to the CARBA software. The resulting vertical deflection profile has already been presented in Figure 5.10. The result is a deflection at the loading points of 0.002884 mm, or a relative displacement of 0.005768 mm from a 1 N applied load. Resolving the linear stiffness from this produces a value of 175.07 N/mm; within 3.7% of the classical analysis result. Certainly, some of the additional compliance seen in the CARBA software output can be explained by slight differences between the classical anal-

ysis and the software-based analysis. Both analyses compute the mid-span deflection and its effect on stiffness, but the classical analysis does not include the portion of the mid-span that extends into and slightly beyond the bushings.

### 5.2.2 Design

As was mentioned, the center-line geometry of the ARB will remain fixed throughout the design. While a simple geometry was shown in the preceding subsection for the purpose of validation, it is sensible to use a coordinate set that more precisely matches the desired geometry during design of the composite bar; that coordinate set and resulting line geometry is shown in Figure 5.11.

With an unknown geometric envelope in which the composite bar may exist, it was determined that keeping the diameter relatively small is of importance. Use of a fibre/matrix combination that is readily available and cost effective increases the viability of high-volume production. For these reasons, a general purpose structure of Hexcel<sup>®</sup> AS4 carbon fibre and 3501-6 epoxy was specified for the outer layers of helically wrapped FRP. The core of the bar, which provides little contribution to stiffness and strength relative to the outer layers, will comprise a more cost-effective fibre: E-glass. Typical in-plane stiffness properties are listed in Table 5.5 for AS4 and E-glass laminated in 3501-6 epoxy with a volume fraction of  $V_f = 0.6$ .

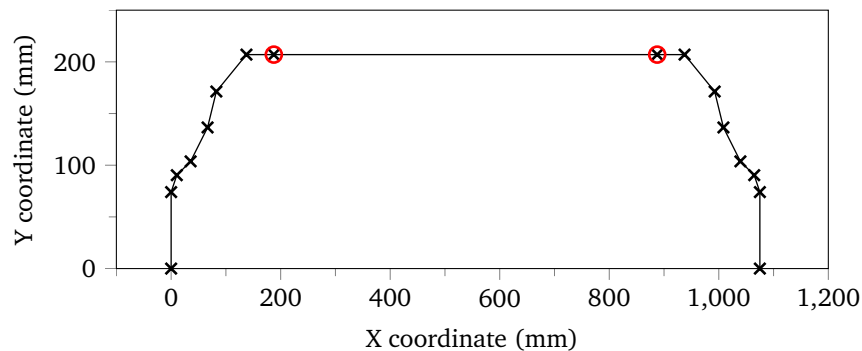


Figure 5.11: Desired line geometry of composite ARB

Table 5.5: In-plane properties of carbon and E-glass unidirectional laminates

Material	$E_{11}$ (GPa)	$E_{22}$ (GPa)	$\nu_{12}$	$G_{12}$ (GPa)	Density (g/cc)	Ref.
AS4(Carbon)/3501-6(Epoxy)	131.0	11.2	0.28	6.55	1.55	[36]
E-glass/Epoxy	38.6	8.27	0.26	4.14	1.80	[37]

For reasons pertinent to the intended manufacturing process, the thickness of the helically wound outer layers has been defined as 0.45 mm and the core diameter as 20 mm. The helically wound

layers are configured such that each successive layer has a fibre-angle equal in magnitude but opposite in sign to the last. An investigation was performed using the CARBA software that demonstrates the variance of expected stiffness with fibre-angle and number of outer layers; the results of this are shown in Figure 5.12. Recall that the benchmarking performed in Section 5.1 established a desired linear spring-rate of approximately 180 N/mm. An outer layer count of 27 produces a peak value of stiffness of 176.13 N/mm at a fibre angle of  $\pm 30^\circ$ .

With a fixed layer size of 0.45 mm, the simplest way to fine-tune the stiffness is by slight adjustment of the core diameter; a 20.30 mm E-glass fibre reinforced epoxy core wound with 27 layers of 0.45 mm thick  $\pm 30^\circ$  carbon fibre reinforced epoxy produces a stiffness of 180.78 N/mm. The outer diameter of the composite ARB resulting from the specified configuration is 44.3 mm. The vertical displacement profile from which the stiffness was extracted can be seen in Figure 5.13.

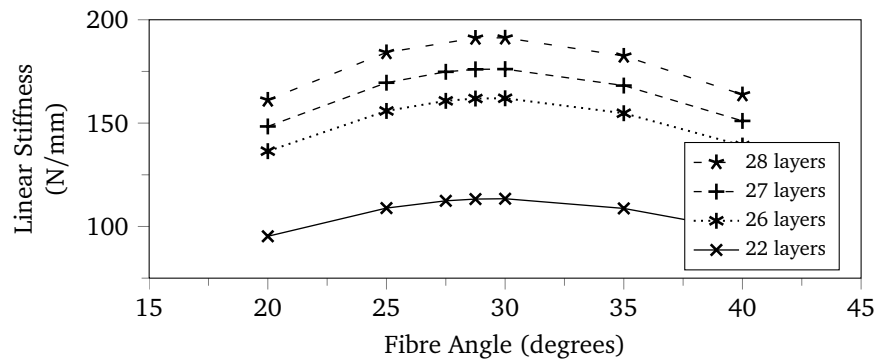


**Figure 5.12:** Linear anti-roll bar stiffness vs. fibre angle for composite bars having 20 mm E-glass unidirectional cores wound with varying numbers of 0.45 mm helically wound carbon/epoxy layers

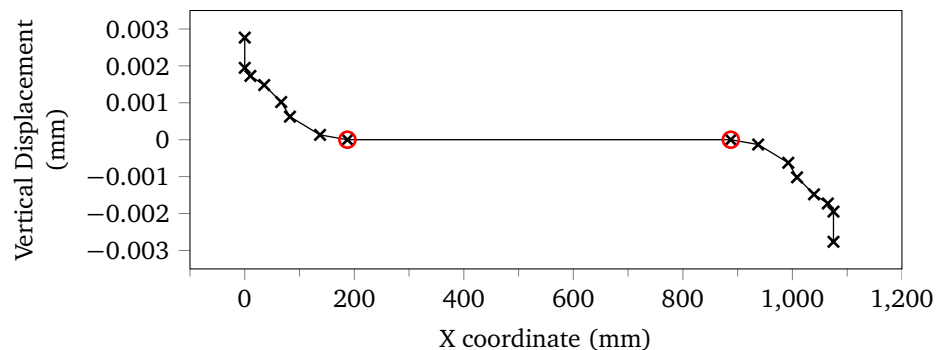


**Figure 5.13:** Vertical displacement profile output from CARBA software for the composite bar

The steel bar's mass has been calculated as 8.58 kg; the mass of the proposed composite bar design

can be calculated in the same manner as 3.18 kg. This results in a mass reduction of 63%. However, this number will likely be reduced slightly when provisions are made for load application connection points on the FRP anti-roll bar.

While the runtime of the CARBA software is a function of the number of input geometry points, as well as other input variables, it is worth noting that the current design requires a runtime of 9.2 seconds<sup>1</sup>. An FE model was not produced for the composite bar, but recall that runtimes on the order of 400 seconds were observed in the numerical analysis of the isotropic steel bar.

### 5.2.3 Discussion and Recommendations

A number of assumptions were necessary in the design of the composite ARB; some of these assumptions have deviated the design from what is optimal. Discussion and recommendations are presented in the following text with regard to areas in which design compromises are present.

With no information available regarding the limits the vehicle's configuration imposes on bar geometry, changes to the bar's overall shape were kept to a minimum to reduce the likelihood of tolerance/interference issues upon installation. It may be safe to conclude that the shape of the existing steel bar is a product of thoughtful consideration of what is optimal, but a filament wound composite bar has considerably different behaviour; a shape that is optimal for a steel ARB is almost certainly not optimal for its composite counterpart.

Perhaps the most limiting assumption present in the current design is that of constant fibre-angle, shape, and bar diameter throughout the length of the ARB. It has been shown that loading varies throughout the length of the bar; the mid-span section (between the bushings) experiences significantly more torsion and less bending load than the sections that extend outward from the bushings. Moreover, the bending moment in the end-sections is maximum near the bushings, but diminishes toward the loading points. The moment varies throughout the mid-span section as well. A design that truly exploits these observations would have fibre-angle, bar diameter, and cross-sectional geometry varying along the length of the bar to reduce its total mass. To that end, the CARBA software has been written in a manner that is conducive to the addition of an optimization scheme producing varying bar diameter and fibre layup, though time constraints prevented the author from including these capabilities.

The CARBA software is limited to the analysis of strictly two-dimensional geometries. This limitation alone has no effect on the present bar design; recall that the lack of a defined geometric envelope restricted the design to a single plane. However, one could easily speculate on the need to design or analyse an ARB that simply cannot be constrained to two dimensions. Three dimensional capability could be added to the CARBA software using the same principles that allowed loading and deformation to be determined in the two-dimensional case. Another possibility is the development of a beam element

<sup>1</sup>Analyses were performed on a PC running Microsoft® Windows® 7 Professional (64 bit) with an Intel® Core™ i7-2600k CPU @ 3.40 GHz. The PC was equipped with 16 GB of RAM.

for a finite element solver; the elasticity model presented herein could be used in parallel with an FE solver to arrive upon the elastic response of an anti-roll bar having complex three-dimensional geometry.



## Chapter 6

# Conclusions & Recommendations

The first section of this chapter provides a summary of what was accomplished. The second section draws conclusions with regard to the work herein, and the third section discusses recommendations for future work.

### 6.1 Summary

An analytical elasticity model has been developed for laminated cylindrically anisotropic cylinders subjected to extension, bending, pressure, torsion, and transverse shearing; care has been taken to ensure that the model captures all elastic coupling present in these loading cases. The model may be applied to thick or thin walled tubes, as well as solid cylinders. While the model's derivation is somewhat long, the end result is pragmatic and concise in matrix form. Once coded into a computer software, the model provides a fast and efficient means of obtaining the elastic response of the tube or cylinder as a function of user-input loadings; elastic response is returned in the form of nine values that describe strain and curvature resultants, as well as strain gradients.

Some computational validation has been provided by comparing the predictions of the laminated cylinder model to those of FE methods for the elastic response of a thin-walled tube subjected to torsional and axial loading. Some experimental validation has been provided by the physical testing, in torsion and in three-point flexure, of two sets of glass-fibre/epoxy cylindrical test specimens.

An existing steel anti-roll bar has been rigorously benchmarked using classical analytical methods, FE methods, and experimental testing. An analysis software has been generated that uses the laminated cylinder model presented herein to predict the linear-elastic response of an anti-roll bar. The center-line geometry of the bar must be planar, but may be specified by a user-generated coordinate set. The analysis software is limited to the linear regime of the bar's elastic response. This software has been used to establish a composite anti-roll bar design, which has been presented here, with the aim of replacing

the existing steel bar.

## 6.2 Conclusions

The presented laminated cylinder model provides a concise method of obtaining a prediction for the elastic response of thick-walled tubes, thin-walled tubes, and cylinders subjected to axial force, bending moment, pressure, torsion, and transverse shearing. The following conclusions may be made regarding this model:

- The predicted response to pressure is not valid for thick-walled tubes. The model does not account for through-thickness normal stress, Timoshenko shear in bending, shear stress attenuation at free edges, or material non-linearity. The model neglects the possibility of any buckling and ignores end-effects associated with loading and shear lag.
- While significant further work is needed for a full validation, the model shows promise to provide a useful means of establishing accurate predictions of elastic response, and internal stress.
- The model is well suited for integration into optimization schemes directed at materials in the discussed regime.

The presented composite anti-roll bar analysis software – CARBA – provides a convenient and efficient means of analysing the linear-elastic stiffness of proposed designs for filament wound, fibre-reinforced, composite anti-roll bars. The CARBA software relies directly on the accuracy of the laminated cylinder model; consequently, it too has yet to be fully validated and adopts all the assumptions of the laminated cylinder model as well as the limitations thereof. The software does not account for the geometric non-linearity of large deformation of the anti-roll bar, and hosts other assumptions and limitations that have been discussed.

A composite bar having a 10.15 mm radius E-glass/epoxy unidirectional  $0^\circ$  core helically wound with 27 layers of  $\pm 30^\circ$  AS4 carbon fibre/epoxy will provide a linear stiffness of 180.78 N·mm. This configuration results in a 44.3 mm diameter anti-roll bar and is expected to have a mass that is 63% less than the steel bar it serves to replace.

## 6.3 Recommendations for Future Work

Some recommendations for future work are provided as follows with regard to both the laminated cylinder model, and the composite anti-roll bar design.

### **Laminated Cylinder Model**

First and foremost, the presented model requires a thorough validation through both FE methods and an experimental program. A non-linear solver could be employed to solve solid-element FE models for a number of tube diameter to wall-thickness ratios, as well as solid cylinders. All loadings handled by the model should be addressed. A large range of laminate configurations needs to be included in the study to ensure proper handling of internal stress; with a fine solid mesh, one could compare stress distributions predicted by the model and the FE method. A number of cases should be validated through experimental testing as well, to provide further confidence in the FE solutions.

Upon the successful completion of model validation, attention could be given to capturing higher-fidelity phenomena such as Timoshenko shear effects, through-thickness normal stress, material non-linearity, and the pressure loading of thick-walled tubes.

The model could easily be adapted to include a failure model such as Tsai-Wu[38], or something more sophisticated to predict matrix cracking, durability, and fatigue. With internal strains and stresses already modelled and accessible, focus could be put directly into application of a current and existing failure model. While some concern should be present regarding material fracture toughness, a protective coating may be enough to provide protection from impact with road debris. General Motor's Corvette uses a GFRP transverse leaf spring that has proved successful for over 30 years (and counting); this spring is in the same general location and orientation that is necessary for an anti-roll bar – in fact the spring doubles as an anti-roll bar.

### **Composite Anti-Roll Bar**

The composite anti-roll bar design presented herein is very much a first order prototype proposal; however, the analysis software has been structured in a manner that is conducive to the addition of design capabilities and changes that are to be recommended in the paragraphs that follow.

The first recommendation is modification of the analysis software to account for a varying diameter, fibre-angle, and layer count throughout the length of the anti-roll bar. There are a number of ways this could be accomplished, but the simplest would likely be to allow user input of a fibre-angle profile as well as a diameter profile, in much the same way that the anti-roll bar shape is handled. The fibre-angle and diameter profiles could be discretized with the same resolution as the bar itself; an individual interpolated value for fibre angle and diameter would be sent to the laminated cylinder model software for each discretized section.

The second recommendation is that provisions be made to the software such that a fibre-angle and diameter profile are generated, instead of input. Reasonable assumptions that would greatly simplify the implementation of this capability include constant layer thickness and constant fibre-angle through the thickness. It is also reasonable to assume that each layer should be oriented negatively to the last. An iterative process could seek to minimize maximum stress within the bar (while still achieving a desired

overall stiffness), or to add diameter to sections of the bar whose compliance most greatly reduces overall bar stiffness, after first optimizing fibre-angle with the same goal.

Lastly, the program could be modified to accommodate three-dimensional bar shape as well as non-vertical loading, with provisions for the non-linearity of large deformation.

The recommended changes for the laminated cylinder model itself would also add a great deal of capability to the software.

## 6.4 Contributions

This section will outline the aspects of the work presented herein that are particularly novel or contributory.

The largest contribution of this work is an elasticity model for laminated cylindrically anisotropic cylinders. To the best knowledge of the author, no elasticity model precedes this publication that accounts for axial, bending, pressure, torsion, and shear loadings, while accounting for all elastic coupling. Moreover, few existing elasticity models provide the simplicity and applicability offered here.

A tailored analysis software has been presented that can provide a foundation for composite anti-roll bar design, utilizing the aforementioned elasticity model. A composite anti-roll bar design has been presented with good argument to support deviation from intuitive and erroneous design optimization decisions.

A robust and versatile torsion testing machine was designed by the author and a colleague. Materials, manufacture, and funding was provided by external agencies, but the machine is property of the University of Windsor and remains in service for future use.

## References

- [1] L. Segel, "Theoretical prediction and experimental substantiation of the response of the automobile to steering control," *Proceedings of the Institution of Mechanical Engineers: Automobile Division*, vol. 10, no. 1, pp. 310–330, 1956.
- [2] N. Barter, "Measurement of vehicle handling by tethered testing," *Proceedings of the Institution of Mechanical Engineers: Automobile Division*, vol. 184, no. 1, pp. 219–231, 1969.
- [3] H. Pacejka, *Tyre and Vehicle Dynamics*. Oxford, UK: Elsevier, 2005.
- [4] J. Chang, "Method of manufacturing hybrid composite leaf springs," June 20 1995. US Patent 5,425,829.
- [5] S. R. Swanson, *Introduction to Design and Analysis With Advanced Composite Materials*. Upper Saddle River, New Jersey, USA: Prentice Hall, 1997.
- [6] P. Mallick, *Fiber-Reinforced Composites: Materials, Manufacturing, and Design*. Boca Raton, Florida, USA: CRC Press, 3rd ed., 2008.
- [7] Makelainen, Pentti, and P. Hassinen, *Light-weight Steel and Aluminium Structures*. Elsevier Science, 1st ed., 1999.
- [8] R. Jones, *Mechanics of Composite Materials*. New York: Hemisphere Publishing, 1975.
- [9] R. Christensen, "The numbers of elastic properties and failure parameters for fiber composites," *Journal of Engineering Materials and Technology*, vol. 120, pp. 110–113, April 1998.
- [10] Z. Hashin and B. Rosen, "The elastic moduli of fiber-reinforced materials," *Journal of Applied Mechanics*, vol. 46, no. 2, pp. 543–550, 1964.
- [11] R. Hill, "Theory of mechanical properties of fibre-strengthened materials: 1. elastic behaviour," *Journal of Mechanics and Physics of Solids*, vol. 12, pp. 199–212, 1964.
- [12] R. Christensen and H. Lo, "Solutions for effective shear properties in three phase sphere and cylinder models," *Journal of Mechanics and Physics of Solids*, vol. 27, pp. 315–330, 1979.

- [13] J. Halpin and J. Kardos, "The halpin-tsai equations: A review," *Polymer Engineering and Science*, vol. 16, pp. 344–352, May 1976.
- [14] Y. Yeow and H. Brinson, "A comparison of simple shear characterization methods for composite laminates," *Composites*, vol. 9, pp. 49–55, January 1978.
- [15] N. Iosipescu, "New accurate procedure for single shear testing of metals," *Journal of Materials*, vol. 2, no. 3, pp. 537–566, 1967.
- [16] D. Walrath and D. Adams, "The Iosipescu shear test as applied to composite materials," *Experimental Mechanics*, vol. 23, no. 1, pp. 105–110, 1983.
- [17] ASTM, "Standard test method for shear properties of composite materials by the v-notched beam method."
- [18] S. Swanson, M. Messick, and G. Toombes, "Comparison of torsion tube and Iosipescu in-plane shear test results for a carbon fibre-reinforced epoxy composite," *Composites*, vol. 16, no. 3, pp. 220–224, 1985.
- [19] B. Rosen, "A simple procedure for experimental determination of the longitudinal shear modulus of unidirectional composites," *Journal of Composite Materials*, vol. 6, pp. 552–554, 1972.
- [20] H. Honickman, J. Johrendt, D. Northwood, and P. Frise, "Design of a pultruded steel-gfrp hybrid structural member," in *proceedings of the ASME 2010 International Mechanical Engineering Congress and Exposition*, no. IMECE2010-37378, (Vancouver, British Columbia, Canada), American Society of Mechanical Engineers (ASME), November 12–18 2010.
- [21] S. Lekhnitskii, "Stress distribution in an elastic bar with curvilinear anisotropy under a tensile force and bending moments," *Prikl. Matem. i Mekh.*, vol. 13, no. 3, pp. 307–316, 1949.
- [22] R. E. Sherrer, "Filament-wound cylinders with axial-symmetric loads," *Journal of Composite Materials*, vol. 1, no. 4, pp. 344–355, 1967.
- [23] V. C. Cutler, "Bending analysis of directionally reinforced plastic pipe," in *16th Annual Technical And Management Conference Proceedings*, The Society of Plastic Industry Inc, 1961.
- [24] S. Timoshenko and J. Goodier, *Theory of Elasticity*. McGraw-Hill Book Company, 1951.
- [25] N. Pagano, J. Halpin, and J. Whitney, "Tension buckling of anisotropic cylinders," *Journal of Composite Materials*, vol. 2, no. 2, pp. 154–167, 1968.
- [26] N. Pagano and J. Whitney, "Geometric design of composite cylindrical characterization specimens," *Journal of Composite Materials*, vol. 4, no. 3, pp. 360–378, 1970.

- [27] N. Pagano, "Stress gradients in laminated composite cylinders," *Journal of Composite Materials*, vol. 5, no. 2, pp. 260–265, 1971.
- [28] E. Reissner and W. Tsai, "On pure bending and stretching of orthotropic laminated cylindrical shells," *Journal of Applied Mechanics*, vol. 41, p. 168, 1974.
- [29] C. Jolicoeur and A. Cardou, "Analytical solution for bending of coaxial orthotropic cylinders," *Journal of Engineering Mechanics*, vol. 120, no. 12, pp. 2556–2574, 1994.
- [30] T. Ting, "Pressuring, shearing, torsion and extension of a circular tube or bar of cylindrically anisotropic material," *Proceedings of the Royal Society of London. Series A: Mathematical, Physical and Engineering Sciences*, vol. 452, no. 1954, pp. 2397–2421, 1996.
- [31] T. Chen, C. Chung, and W. Lin, "A revisit of a cylindrically anisotropic tube subjected to pressuring, shearing, torsion, extension and a uniform temperature change," *International Journal of Solids and Structures*, vol. 37, no. 37, pp. 5143–5159, 2000.
- [32] C. Chouchaoui and O. Ochoa, "Similitude study for a laminated cylindrical tube under tensile, torsion, bending, internal and external pressure. part i: Governing equations," *Composite Structures*, vol. 44, no. 4, pp. 221–229, 1999.
- [33] J. Tarn and Y. Wang, "Laminated composite tubes under extension, torsion, bending, shearing and pressuring: a state space approach," *International Journal of Solids and Structures*, vol. 38, no. 50, pp. 9053–9075, 2001.
- [34] J. Tarn, "A state space formalism for anisotropic elasticity: Part ii: Cylindrical anisotropy," *International Journal of Solids and Structures*, vol. 39, no. 20, pp. 5157–5172, 2002.
- [35] S. Swanson, "Torsion of laminated rectangular rods," *Composite Structures*, no. 42, pp. 23–31, 1998.
- [36] S. Swanson and A. Christoforou, "Response of quasi-isotropic carbon/epoxy laminates to biaxial stress," *Journal of Composite Materials*, vol. 20, no. 5, pp. 457–471, 1986.
- [37] S. W. Tsai and T. N. Massard, *Composites Design*. Think Composites, 1985.
- [38] W. E. Tsai, S.W., "A general theory of strength for anisotropic materials," *Journal of Composite Materials*, vol. 5, no. 1, pp. 58–80, 1971.

## Appendix A

# Specimen Measurements

As was discussed in Section 4.2.1, each specimen was subjected to a number of measurements to establish average dimensions and properties; each measurement is shown as follows:

**Table A.1:** Sample 1A measurements

Mass (g)	Length (mm)	Diameter (mm)	Core Diameter (mm)	Fibre angle (degrees)
640.8	733.98	24.90	14.21	50
	733.86	25.08	14.00	56
		25.10	13.69	50
		25.15	13.50	
		25.54		
		25.40		

**Table A.2:** Sample 1B measurements

Mass (g)	Length (mm)	Diameter (mm)	Core Diameter (mm)	Fibre angle (degrees)
644.7	734.18	25.03	14.16	-43
	734.11	25.40	13.30	-47
		25.75	14.70	-48
		24.10	13.90	
		25.00		
		25.29		



Table A.3: Sample 1C measurements

Mass (g)	Length (mm)	Diameter (mm)	Core Diameter (mm)	Fibre angle (degrees)
649.2	734.26	25.00	16.31	-50
	734.30	24.90	15.70	-51
		25.05	16.80	-40
		25.48	15.50	
		25.42		
		25.35		

Table A.4: Sample 2A measurements

Mass (g)	Length (mm)	Diameter (mm)	Fibre angle (degrees)
682.1	734.33	24.88	-16
	734.13	25.08	-16
		24.99	-15
		24.98	
		25.18	
		25.05	

Table A.5: Sample 2B measurements

Mass (g)	Length (mm)	Diameter (mm)	Fibre angle (degrees)
677.4	733.63	24.84	9
	733.58	25.02	6
		25.01	8
		24.81	
		25.05	
		25.02	

Table A.6: Sample 2C measurements

Mass (g)	Length (mm)	Diameter (mm)	Fibre angle (degrees)
680.5	734.37	25.14	10
	735.01	25.53	10
		25.19	12
		25.11	
		25.23	
		24.98	

## Appendix B

# Laminated Cylinder Model Input

The material properties of the Jushi<sup>®</sup> E6 312T E-glass fibres used in the core of samples 1A, 1B, 1C, and in samples 2A, 2B, 2C are listed in Table B.1 as  $E_F$  core,  $G_f$  core, and  $\nu_f$ . The properties of the Fibrex<sup>™</sup> TR-503-N-4900T E-glass fibres used in the outer layer of samples 1A, 1B, and 1C are shown in Table B.1 as  $E_F$  outer,  $G_f$  outer, and  $\nu_f$ . The density of the fibres is assumed to be  $0.002540 \text{ g/mm}^3$ .

The material properties of the cured Adtech<sup>™</sup> EP-700 epoxy with EP-802 hardener are shown in Table B.1 as  $E_m$ ,  $G_m$ , and  $\nu_m$ . The density of the cured matrix was assumed to be  $0.001107 \text{ g/mm}^3$ .

For both the fibres and the matrix, the longitudinal moduli  $E_f$  and  $E_m$  were extracted from the manufacturers' documentation, while Poisson's ratios  $\nu_f$  and  $\nu_m$  were assumed from [6];  $G_f$  and  $G_m$  were calculated using the values just listed.

**Table B.1:** Material properties of E-glass fibres and epoxy matrix used in test specimens

$E_f$ core (MPa)	$E_f$ outer (MPa)	$E_m$ (MPa)	$G_f$ core (MPa)	$G_f$ outer (MPa)	$G_m$ (MPa)	$\nu_f$	$\nu_m$
80454	73000	3200	32705	29675	1185.2	0.23	0.35

The specimen measurements that are seen in Appendix A were averaged and used to calculate a fibre volume fraction. The volume of the specimens was calculated as length times cross-sectional area; this volume was used to calculate specimen density. From there, an iterative solver was used to establish the volume fraction necessary to produce the calculated specimen density, knowing the fibre and matrix densities. The results of this fibre volume fraction calculation are shown in Table B.2.

The elastic properties of the laminae that constitute sections of the samples were established using the fibre and matrix material properties seen in Table B.1 and the fibre volume fraction results of Table B.2. Longitudinal moduli ( $E_{11}$ ), and Poisson's ratios ( $\nu_{12}$ ,  $\nu_{21}$ ) were calculated using the rule of mixtures model, while transverse properties ( $E_{22}$ ,  $G_{12}$ ) were calculated using Halpin-Tsai formulation. The resulting elastic properties for each specimen are shown in Table B.3.

Each of the 1X-series specimens contains 11 layers of helically wrapped outer layers of alternating fibre-angle and a uni-directional core. The thickness of the outer layers was established by subtracting the measured core diameter from the outer diameter. The 11 layers were assumed to be of equal thickness and opposing angles.

The 2X-series specimens do not contain distinct layers, but a continuum of linearly varying fibre-angle. Accordingly, they were modelled with 30 layers of equal thickness having a fibre-angle that varies linearly from 0 to  $\theta$ , where theta is the average of the measured outer fibre-angles listed in Appendix A. The use of 30 layers is somewhat arbitrary, but also somewhat irrelevant: beyond a certain number of layers, little change in elastic response is observed with additional layers.

**Table B.2:** Specimen fibre volume fraction calculation

Sample	Volume (mm <sup>3</sup> )	Net Density	calc Density	$V_f$
1A	365904.1	0.0017513	0.0017513	0.44962
1B	363116.6	0.0017755	0.0017755	0.46650
1C	366228.9	0.0017727	0.0017727	0.46455
2A	361183.6	0.0018885	0.0018885	0.54536
2B	358908.2	0.0018874	0.0018874	0.54459
2C	366336.5	0.0018576	0.0018576	0.52380

**Table B.3:** Local elastic properties of individual laminae in test specimens

Sample	$E_{11}$	$\nu_{12}$	$\nu_{21}$	G12	E22
1A (core)	37935	0.29605	0.043946	2888.8	9597.9
1A (outer)	34583	0.29605	0.048051	2867.3	9474.4
1B (core)	39239	0.29402	0.043434	3001.8	10008.6
1B (outer)	35762	0.29402	0.047494	2978.3	9874.0
1C (core)	39088	0.29425	0.043488	2988.4	9960.0
1C (outer)	35626	0.29425	0.047553	2965.1	9826.7
2A	45331	0.28456	0.042171	3625.0	12243.7
2B	45272	0.28465	0.042174	3618.0	12219.0
2C	43665	0.28714	0.042337	3436.9	11574.2

## Appendix C

# Laminated Cylinder Model Code

The laminated cylinder model discussed in Chapter 3 has been coded into MATLAB<sup>®</sup>. That code is shown in this appendix.

19/09/13 1:38 PM E:\Documents\MSc Thesis\Thu...\Laminated\_cylinder\_model\_func.m 1 of 4

```

function [strain_curvs] = Laminated_cylinder_model_func(resultants)

%Import Data from CSV file
layup = importdata('layup.csv', ',', 1);

r_i =0.0; % Inner Radius

%Material Properties by layer
t_k = layup.data(:,2); % layer thickenss
theta_fiber = layup.data(:,3); % fiber angle
E11 = layup.data(:,4); % Long. Modulus
E22 = layup.data(:,5); % Trans. Modulus
v12 = layup.data(:,6);
v21 = layup.data(:,7);
G12 = layup.data(:,8); % Shear Modulus
% F1t = layup.data(:,9); %-----
% F2t = layup.data(:,10); %
% F1c = layup.data(:,11); % Tsai-Wu failure criteria
% F2c = layup.data(:,12); %
% F6 = layup.data(:,13); %-----
r_k = zeros([length(t_k),1]); %Preallocate matrix for speed
r_k(1) = r_i + t_k(1)/2; %Mid-layer radii
for i = 2 : length(t_k) %Mid-layer radii
    r_k(i) = r_k(i-1) + t_k(i-1)/2 + t_k(i)/2;
end

%% Generate Q and Q_bar Matrices

D = (1 - v12.*v21); %denominator for Q matrix
Q11 = E11./D; %-----
Q12 = v21.*E11./D; %
Q21 = v12.*E22./D; % Q Matrix
Q22 = E22./D; %
Q66 = G12; %-----

m = cos(deg2rad(theta_fiber)); %cos term for Q bar eqn
n = sin(deg2rad(theta_fiber)); %sin term for Q bar eqn
% Q Bar Matrix
Qbar11 = Q11.*(m.^4) + 2*(Q12 + 2*Q66).*n.^2.*m.^2 + Q22.*n.^4;
Qbar12 = (Q11 + Q22 - 4.*Q66).*n.^2.*m.^2 + Q12.*(n.^4 + m.^4);
Qbar21 = Qbar12;
Qbar22 = Q11.*n.^4 + 2*(Q12 + 2.*Q66).*n.^2.*m.^2 + Q22.*m.^4;
Qbar16 = (Q11 - Q12 - 2*Q66).*n.*m.^3 + (Q12 - Q22 + 2*Q66).*n.^3.*m;
Qbar61 = Qbar16;
Qbar26 = (Q11 - Q12 - 2*Q66).*n.^3.*m + (Q12 - Q22 + 2*Q66).*n.*m.^3;
Qbar62 = Qbar26;
Qbar66 = (Q11 + Q22 - 2*Q12 - 2*Q66).*n.^2.*m.^2 + Q66.*(n.^4 + m.^4);

```

19/09/13 1:38 PM E:\Documents\MSc Thesis\Thu...\Laminated\_cylinder\_model\_func.m 2 of 4

```

%Generate G terms needed for Shear Calculations
G13 = Q66;
v23 = v12.*(1-v21)./(1-v12);
G23 = E22./(2.*(1+v23));
Gik = G13.*(cos(theta_fiber)).^2+G23.*(sin(theta_fiber)).^2;

%% Generate M matrix terms
%-----
%Axial Force Equations
sum = 0;
for i = 1 : length(t_k)
%   sum = sum + t_k(i)*r_k(i)*Qbar11(i);
    sum = sum + ((r_k(i)+t_k(i)/2)^2-(r_k(i)-t_k(i)/2)^2)/2*Qbar11(i);
end
M(1,1) = 2*pi()*sum; % M_11 term in M matrix

sum = 0;
for i = 1 : length(t_k)
%   sum = sum + t_k(i)*r_k(i)*Qbar12(i);
    sum = sum + ((r_k(i)+t_k(i)/2)^2-(r_k(i)-t_k(i)/2)^2)/2*Qbar12(i);
end
M(1,6) = 2*pi()*sum; % M_16 term in M matrix

sum = 0;
for i = 1 : length(t_k)
%   sum = sum + t_k(i)*r_k(i)^2*Qbar16(i);
    sum = sum + ((r_k(i)+t_k(i)/2)^3-(r_k(i)-t_k(i)/2)^3)/3*Qbar16(i);
end
M(1,7) = -2*pi()*sum; % M_17 term in M matrix
%-----
%Moment Equations
sum = 0;
for i = 1 : length(t_k)
    sum = sum + ((r_k(i)+t_k(i)/2)^4-(r_k(i)-t_k(i)/2)^4)/4*Qbar11(i);
end
M(2,2) = pi()*sum; % M_22 term in M matrix
M(3,3) = --M(2,2); % M_33 term in M matrix

sum = 0;
for i = 1 : length(t_k)
    sum = sum + ((r_k(i)+t_k(i)/2)^4-(r_k(i)-t_k(i)/2)^4)/4*Qbar12(i);
end
M(2,4) = pi()*sum; % M_24 term in M matrix
M(3,5) = -M(2,4); % M_35 term in M matrix

sum = 0;
for i = 1 : length(t_k)
    sum = sum + ((r_k(i)+t_k(i)/2)^3-(r_k(i)-t_k(i)/2)^3)/3*Qbar16(i);
end
M(2,8) = pi()*sum; % M_28 term in M matrix
M(3,9) = --M(2,8); % M_39 term in M matrix

```

---

19/09/13 1:38 PM E:\Documents\MSc Thesis\Thu...\Laminated\_cylinder\_model\_func.m 3 of 4

---

```

%-----
%Equilibrium Equations
sum = 0;
for i = 1 : length(t_k)
    sum = sum + ((r_k(i)+t_k(i)/2)^3-(r_k(i)-t_k(i)/2)^3)/3*Qbar21(i);
end
M(4,2) = 2*sum; % M_42 term in M matrix
M(5,3) = -M(4,2); % M_53 term in M matrix

sum = 0;
for i = 1 : length(t_k)
    sum = sum + ((r_k(i)+t_k(i)/2)^3-(r_k(i)-t_k(i)/2)^3)/3*Qbar22(i);
end
M(4,4) = 2*sum; % M_44 term in M matrix
M(5,5) = M(4,4); % M_55 term in M matrix

sum = 0;
for i = 1 : length(t_k)
    sum = sum + ((r_k(i)+t_k(i)/2)^2-(r_k(i)-t_k(i)/2)^2)/2*Qbar26(i);
end
M(4,8) = 2*sum; % M_48 term in M matrix
M(5,9) = -M(4,8); % M_59 term in M matrix
%-----
%Pressure*radius Equations
sum = 0;
for i = 1 : length(t_k)
    sum = sum + t_k(i)*Qbar21(i);
end
M(6,1) = sum; % M_61 term in M matrix

sum = 0;
for i = 1 : length(t_k)
    sum = sum + t_k(i)*Qbar22(i);
end
M(6,6) = sum; % M_66 term in M matrix

sum = 0;
for i = 1 : length(t_k)
    sum = sum + ((r_k(i)+t_k(i)/2)^2-(r_k(i)-t_k(i)/2)^2)/2*Qbar26(i);
end
M(6,7) = -sum; % M_67 term in M matrix
%-----
%Torsion Equations
sum = 0;
for i = 1 : length(t_k)
    sum = sum + ((r_k(i)+t_k(i)/2)^3-(r_k(i)-t_k(i)/2)^3)/3*Qbar61(i);
end
M(7,1) = -2*pi()*sum; % M_71 term in M matrix

sum = 0;
for i = 1 : length(t_k)

```

---

19/09/13 1:38 PM E:\Documents\MSc Thesis\Thu...\Laminated\_cylinder\_model\_func.m 4 of 4

---

```

    sum = sum + ((r_k(i)+t_k(i)/2)^3-(r_k(i)-t_k(i)/2)^3)/3*Qbar62(i);
end
M(7,6) = -2*pi()*sum; % M_76 term in M matrix

sum = 0;
for i = 1 : length(t_k)
    sum = sum + ((r_k(i)+t_k(i)/2)^4-(r_k(i)-t_k(i)/2)^4)/4*Qbar66(i);
end
M(7,7) = 2*pi()*sum; % M_77 term in M matrix
%-----
%Shear Force Equations
sum = 0;
for i = 1 : length(t_k)
    sum = sum + ((r_k(i)+t_k(i)/2)^3-(r_k(i)-t_k(i)/2)^3)/3*Qbar61(i);
end
M(8,2) = pi()*sum; % M_82 term in M matrix
M(9,3) = pi()*sum; % M_93 term in M matrix

sum = 0;
for i = 1 : length(t_k)
    sum = sum + ((r_k(i)+t_k(i)/2)^3-(r_k(i)-t_k(i)/2)^3)/3*Qbar62(i);
end
M(8,4) = pi()*sum; % M_84 term in M matrix
M(9,5) = -pi()*sum; % M_95 term in M matrix

sum = 0;
for i = 1 : length(t_k)
    sum = sum + ((r_k(i)+t_k(i)/2)^2-(r_k(i)-t_k(i)/2)^2)/2 * (Qbar66(i) + Gik(i));
end
M(8,8) = pi()*sum; % M_88 term in M matrix
M(9,9) = pi()*sum; % M_99 term in M matrix

%% Calculate Strains

m = inv(M);

strain_curvs = m*resultants';

end

```



## Appendix D

# Composite Anti-Roll Bar Analysis Code

The composite anti-roll bar analysis (CARBA) software discussed in Section 5.2.1 has been coded into `MATLAB`<sup>®</sup>. That code is shown in this appendix.

19/09/13 1:41 PM E:\Documents\MSc Thesis\Thunder Composi...\SwayBarProgram\_11.m 1 of 8

```

%% Copyright (C) 2013, Michael Doody
%% This is free software; you can redistribute it and/or modify it
%% under the terms of the GNU General Public License as published by
%% the Free Software Foundation.
%%
%% This software is distributed in the hope that it will be useful, but
%% WITHOUT ANY WARRANTY; without even the implied warranty of
%% MERCHANTABILITY or FITNESS FOR A PARTICULAR PURPOSE. See the GNU
%% General Public License for more details at www.gnu.org/copyleft/gpl.html.
%%
%%-----

% ASSUMPTIONS:
%   - The desired centerline geometry of the ARB is known and exists
%     within a two-dimensional plane
%   - The bar is round in cross section throughout its entirety
%   - Loads are at first and last (X,Y) point.
%   - Exactly two bushings are defined by the presence of a "1" in the
%     cell to the right of the corresponding (X,Y) pair.
%   - Loads and bushings are symmetric about a vertical line passing
%     through the center of the sway bar.
%   - Sway bar is not a curved beam, but a collection of straight
%     sections.
%   - Bushings constrain all translation but no rotation.

clear all
close all
clc

%% Import/plot Model Input

%Import Data from CSV file
shape = importdata('shape.csv', ',', 1);
X = shape.data(:,1); % X values of sway bar shape
Y = shape.data(:,2); % Y values of sway bar shape
bushings = shape.data(:,3);
F = shape.data(1,4); % Force magnitude
numPoints = length(X);

% Plot csv data
plot(X,Y,'-+')
axis equal
title('Sway Bar Shape')
grid on
hold on

%% Determine & plot Bushing Location
i=0;
while i <= numPoints-1
    i = i+1;
    if isfinite(bushings(i)) == 1

```

19/09/13 1:41 PM E:\Documents\MSc Thesis\Thunder Composi...\SwayBarProgram\_11.m 2 of 8

```

        bushing1 = i;
        plot(X(i),Y(i),'ro')
        i = numPoints+100; % force exit loop
    end
end
i = bushing1+1;
while i <= numPoints
    if isfinite(bushings(i)) == 1
        bushing2 = i;
        plot(X(i),Y(i),'ro')
    end
    i = i+1;
end
bushingSpacing = X(bushing2) - X(bushing1); %determine bushing spacing
totalSpan = X(numPoints)-X(1);
%% Determine global angle of each section
for i = 1:numPoints-1
    if (X(i+1)-X(i)) >= 0 % angle is right of the vertical
        if (Y(i+1)-Y(i)) >= 0 %first quadrant
            sectOrient(i) = atan( (Y(i+1)-Y(i))/(X(i+1)-X(i)) ); %angle from horizontal of ✓
        section i
        else %fourth quadrant
            sectOrient(i) = 2*pi() + atan( (Y(i+1)-Y(i))/(X(i+1)-X(i)) ); %angle from horizontal ✓
        of section i
        end
    else % angle is left of the vertical
        if (Y(i+1)-Y(i)) >= 0 %second quadrant
            sectOrient(i) = pi() + atan( (Y(i+1)-Y(i))/(X(i+1)-X(i)) ); %angle from horizontal ✓
        of section i
        else %third quadrant
            sectOrient(i) = pi() + atan( (Y(i+1)-Y(i))/(X(i+1)-X(i)) ); %angle from horizontal ✓
        of section i
        end
    end
end
end

%% Calculate Moments, torques, shears

% Initialize variables
MyArm = zeros([numPoints-1,2]); % starting (1st column) and final (2nd column) moment ✓
arm for each section
My = zeros([numPoints-1,2]);
TArm = zeros([numPoints-1,1]); % torque in each section (constant across section)
T = zeros([numPoints-1,1]);
V = zeros([numPoints-1,1]); % shear force in each section (constant across section)
l = zeros([numPoints-1,1]); % length of section i
Mx_global = zeros([numPoints,1]);
My_global = zeros([numPoints,1]);

%Loops for all left, middle and right sections
%Left Section of bar

```

19/09/13 1:41 PM E:\Documents\MSc Thesis\Thunder Composi...\SwayBarProgram\_11.m 3 of 8

```

for i = 1:bushing1 %nodes
    Mx_global(i) = -F * ( Y(i) - Y(1) );
    My_global(i) = F * ( X(i) - X(1) );
end
for i = 1:(bushing1-1) %sections
    My(i,1) = Mx_global(i)*sin(sectOrient(i)) - My_global(i)*sin( pi()/2 -
sectOrient(i)) ;
    My(i,2) = Mx_global(i+1)*sin(sectOrient(i)) - My_global(i+1)*sin( pi()/2 -
sectOrient(i)) ;

    T(i,1) = Mx_global(i)*cos(sectOrient(i)) + My_global(i)*cos( pi()/2 - sectOrient
(i)) ;
    T(i,2) = Mx_global(i+1)*cos(sectOrient(i)) + My_global(i+1)*cos( pi()/2 -
sectOrient(i)) ;

    V(i,1) = -F;

    l(i) = ((X(i+1)-X(i))^2+(Y(i+1)-Y(i))^2)^0.5; %section length (for later use)
end

%Right section of bar
for i = bushing2:numPoints %nodes
    Mx_global(i) = -F * ( Y(i) - Y(numPoints) );
    My_global(i) = F * ( X(i) - X(numPoints) );
end
for i = bushing2:(numPoints-1) %sections
    My(i,1) = -Mx_global(i)*sin(sectOrient(i)) + My_global(i)*sin( pi()/2 -
sectOrient(i)) ;
    My(i,2) = -Mx_global(i+1)*sin(sectOrient(i)) + My_global(i+1)*sin( pi()/2 -
sectOrient(i)) ;

    T(i,1) = Mx_global(i)*cos(sectOrient(i)) + My_global(i)*cos( pi()/2 - sectOrient
(i)) ;
    T(i,2) = Mx_global(i+1)*cos(sectOrient(i)) + My_global(i+1)*cos( pi()/2 -
sectOrient(i)) ;

    V(i,1) = -F;

    l(i) = ((X(i+1)-X(i))^2+(Y(i+1)-Y(i))^2)^0.5; %section length (for later use)
end

%Middle section - between bushings
shearMidSect = F*(totalSpan/bushingSpacing - 1);
for i = bushing1:bushing2 %nodes
    Mx_global(i) = Mx_global(bushing1) - (Y(i)-Y(bushing1))*shearMidSect;
    My_global(i) = My_global(bushing1) - (X(i)-X(bushing1))*shearMidSect;
end
for i = bushing1:(bushing2-1) %sections
    My(i,1) = -Mx_global(i)*sin(sectOrient(i)) + My_global(i)*sin( pi()/2 -
sectOrient(i)) ;
    My(i,2) = -Mx_global(i+1)*sin(sectOrient(i)) + My_global(i+1)*sin( pi()/2 -

```

19/09/13 1:41 PM E:\Documents\MSc Thesis\Thunder Composi...\SwayBarProgram\_11.m 4 of 8

```

sectOrient(i) ;

    T(i,1) = Mx_global(i)*cos(sectOrient(i)) + My_global(i)*cos( pi()/2 - sectOrient
(i) ) ;
    T(i,2) = Mx_global(i+1)*cos(sectOrient(i)) + My_global(i+1)*cos( pi()/2 -
sectOrient(i) ) ;

    V(i,1) = F*(totalSpan/bushingSpacing-1);

    l(i) = ((X(i+1)-X(i))^2+(Y(i+1)-Y(i))^2)^0.5; %section length (for later use)
end

%%
%Break each section into parts, query laminated tube function for deflections

numEls = 100;
strain_curvs = zeros([9 numEls]); % number of discrete elements in each section

for i = 1:(numPoints-1) % calculate for each section
    for j = 1:numEls %break each section into discrete beams with constant moment,
torque, shear, radius etc.

        F_xx = 0;
        M_y(j,i) = (My(i,1)+(My(i,2)-My(i,1))*(j-0.5)/numEls); %moment interpolated at
midpoint of discrete beam 'j' in section 'i'
        M_z = 0;
        % 0
        % 0
        Pr_i = 0;
        T_model(j,i) = T(i,1);
        V_xy(j,i) = 0;
        V_xz = V(i,1);

        resultants = [F_xx,M_y(j,i),M_z,0,0,Pr_i,T_model(j,i),V_xy(j,i),V_xz];
        [strain_curvs(:,(i-1)*(numEls)+j)] = Laminated_cylinder_model_func(resultants); %
matrix containing a strains/curvatures column for each discrete beam of each section
    end

end

%% Begin calculating deflection/curvature
%initialize variables
Z_2 = zeros(1,numPoints-1);
slope = zeros(numEls,numPoints-1);
phi = zeros(numEls,numPoints-1);
deltaZ = zeros(1,numPoints);
kappa_y = zeros(1,numPoints); %Curvature of discrete subsection
dPhidx = zeros(1,numPoints); %Angle of twist of discrete subsection
gammamaxz = zeros(1,numPoints); %Shear deformation angle of discrete subsection

```

19/09/13 1:41 PM E:\Documents\MSc Thesis\Thunder Composi...\SwayBarProgram\_11.m 5 of 8

```

%Middle Section of bar
slopeBushing1 = 0 ;
slopeBushing2 = 0 ;
phiBushing1 = 0 ;
deltaSlopeMid = 0;
p=0;
while abs(abs(slopeBushing1)-abs(slope(numEls,bushing2-1))) >= 0.0001*abs(slope(numEls,
bushing2-1)) || abs(slopeBushing2)==0
for i = bushing1:(bushing2-1) %sections
    elLength = l(i)/numEls;
    for j = 1:numEls
        kappa_y(j) = strain_curvs(2,(i-1)*(numEls)+j); %Curvature of discrete subsection
        dPhidx(j) = strain_curvs(7,(i-1)*(numEls)+j); %Angle of twist of discrete
subsection
        gammaxz(j) = strain_curvs(9,(i-1)*(numEls)+j); %Shear deformation angle of
discrete subsection
        if j == 1 % transfer slopes and twists into coordinate system of next section
            if i == bushing1
                slope(j,i) = slopeBushing1 + kappa_y(j)*elLength ;
                phi(j,i) = phiBushing1 + elLength*dPhidx(j);
            else
                slope(j,i) = kappa_y(j)*elLength...
                    + slope(numEls, i-1)*cos( sectOrient(i-1) - sectOrient(i) )...
                    + phi(numEls, i-1)*sin( sectOrient(i-1) - sectOrient(i) ) ;
                phi(j,i) = elLength*dPhidx(j)...
                    - slope(numEls, i-1)*sin( sectOrient(i-1) - sectOrient(i) )...
                    + phi(numEls, i-1)*cos( sectOrient(i-1) - sectOrient(i) ) ;

                deltaZ(j) = elLength*gammaxz(j)... %shear
                    + (1-cos(elLength*kappa_y(j)))/kappa_y(j)... %curvature
                    + elLength*sin(slope(numEls,i-1)); %tangency
            end
        else
            slope(j,i) = kappa_y(j)*elLength + slope(j-1,i) ; %cumulative slope
            phi(j,i) = elLength*dPhidx(j) + phi(j-1,i); %cumulative angle of twist

            deltaZ(j) = elLength*gammaxz(j)... %shear
                + (1-cos(elLength*kappa_y(j)))/kappa_y(j)... %curvature
                + elLength*sin(slope(j-1,i)); %tangency
        end

    end

    Z_2(i+1) = sum(deltaZ) + Z_2(i);
end

deltaSlopeMid =atan(Z_2(bushing2)/(bushingSpacing));

slopeBushing1 = slopeBushing1 - deltaSlopeMid;
slopeBushing2 = slope(numEls,bushing2-1) - deltaSlopeMid;

```

19/09/13 1:41 PM E:\Documents\MSc Thesis\Thunder Composi...\SwayBarProgram\_11.m 6 of 8

```

deltaPhiMid = phi(numEls,bushing2-1) - phiBushing1;

phiBushing1 = -deltaPhiMid/2;
phiBushing2 = deltaPhiMid/2;

p = p+1;
end

%Left Section of bar (up to but not including bushing #1)
for i = (bushing1 - 1):-1:1
    elLength = l(i)/numEls;
    for j = numEls:-1:1
        %curvatures and strains become negative when moving backwards
        %along the beam
        kappa_y(j) = -strain_curvs(2,(i-1)*(numEls)+j); %Curvature of discrete
subsection
        dPhidx(j) = -strain_curvs(7,(i-1)*(numEls)+j); %Angle of twist of discrete
subsection
        gammaxz(j) = -strain_curvs(9,(i-1)*(numEls)+j); %Shear deformation angle of
discrete subsection

        if j == numEls % transfer slopes and twists into coordinate system of next
section
            if i == (bushing1 - 1) % Section connected to bushing
                slope(j,i) = kappa_y(j)*elLength... slope at end (pointing away
from bushing) of constant curvature beam j
                    + -slopeBushing1*cos(sectOrient(i) - sectOrient(i+1))...
                    + phiBushing1*sin(sectOrient(i) - sectOrient(i+1));
                phi(j,i) = elLength*dPhidx(j)...
                    - -slopeBushing1*sin( sectOrient(i) - sectOrient(i+1) )...
                    + phiBushing1*cos( sectOrient(i) - sectOrient(i+1) );

                deltaZ(j) = elLength*gammaxz(j)... %shear
                    + (1-cos(elLength*kappa_y(j)))/kappa_y(j)... %curvature
                    + -elLength*sin(slopeBushing1); %tangency

            else %section connected to node
                slope(j,i) = kappa_y(j)*elLength... slope at end (pointing away
from bushing) of constant curvature beam j
                    + slope(1, i+1)*cos(sectOrient(i) - sectOrient(i+1))...
                    + phi(1, i+1)*sin(sectOrient(i) - sectOrient(i+1));
                phi(j,i) = elLength*dPhidx(j)...
                    - slope(1, i+1)*sin( sectOrient(i) - sectOrient(i+1) )...
                    + phi(1, i+1)*cos( sectOrient(i) - sectOrient(i+1) );

                deltaZ(j) = elLength*gammaxz(j)... %shear
                    + (1-cos(elLength*kappa_y(j)))/kappa_y(j)... %curvature
                    + elLength*sin(slope(1,i+1)); %tangency
            end
        end
    end
end

```

19/09/13 1:41 PM E:\Documents\MSc Thesis\Thunder Composi...\SwayBarProgram\_11.m 7 of 8

```

        end
    else %section connected to element
        slope(j,i) = kappa_y(j)*elLength + slope(j+1,i) ; %cumulative slope
        phi(j,i) = elLength*dPhidx(j) + phi(j+1,i); %cumulative angle of twist

        deltaZ(j) = elLength*gammaxz(j)... %shear
            + (1-cos(elLength*kappa_y(j)))/kappa_y(j)... %curvature
            + elLength*sin(slope(j+1,i)); %tangency
    end
end
Z_2(i) = sum(deltaZ) + Z_2(i+1);
end

%Right Section of bar (from but not including bushing #2)
for i = bushing2:(numPoints-1) %sections
    elLength = l(i)/numEls;
    for j = 1:numEls
        kappa_y(j) = strain_curvs(2,(i-1)*(numEls)+j); %Curvature of discrete✓
subsection
        dPhidx(j) = strain_curvs(7,(i-1)*(numEls)+j); %Angle of twist of discrete✓
subsection
        gammaxz(j) = strain_curvs(9,(i-1)*(numEls)+j); %Shear deformation angle of✓
discrete subsection
        if j == 1 % transfer slopes and twists into coordinate system of next✓
section
            slope(j,i) = kappa_y(j)*elLength...
                + slope(numEls, i-1)*cos( sectOrient(i-1) - sectOrient(i) )...
                + phi(numEls, i-1)*sin( sectOrient(i-1) - sectOrient(i) ) ;
            phi(j,i) = elLength*dPhidx(j)...
                - slope(numEls, i-1)*sin( sectOrient(i-1) - sectOrient(i) )...
                + phi(numEls, i-1)*cos( sectOrient(i-1) - sectOrient(i) ) ;

            deltaZ(j) = elLength*gammaxz(j)... %shear
                + (1-cos(elLength*kappa_y(j)))/kappa_y(j)... %curvature
                + elLength*sin(slope(numEls,i-1)); %tangency
        else
            slope(j,i) = kappa_y(j)*elLength + slope(j-1,i) ; %cumulative slope
            phi(j,i) = elLength*dPhidx(j) + phi(j-1,i); %cumulative angle of twist

            deltaZ(j) = elLength*gammaxz(j)... %shear
                + (1-cos(elLength*kappa_y(j)))/kappa_y(j)... %curvature
                + elLength*sin(slope(j-1,i)); %tangency
        end
    end

    Z_2(i+1) = sum(deltaZ) + Z_2(i);
end
end

```



---

19/09/13 1:41 PM E:\Documents\MSc Thesis\Thunder Composi...\SwayBarProgram\_11.m 8 of 8

---

```
figure
plot(X, z_2, '+-')
title('Sway Bar Deflected Shape')
grid on
```

```
1/(z_2(1)*2)
```

## **Vita Auctoris**

Michael Doody was born in Saint John, New Brunswick, Canada, in 1989. He graduated from Hampton High School in Hampton, New Brunswick in 2007, and from University of New Brunswick in 2011 with a Bachelor's degree in Mechanical Engineering. This document will mark the final requirements of his degree at the University of Windsor, a Master of Science in Mechanical Engineering.